



저작자표시-비영리-변경금지 2.0 대한민국

이용자는 아래의 조건을 따르는 경우에 한하여 자유롭게

- 이 저작물을 복제, 배포, 전송, 전시, 공연 및 방송할 수 있습니다.

다음과 같은 조건을 따라야 합니다:



저작자표시. 귀하는 원저작자를 표시하여야 합니다.



비영리. 귀하는 이 저작물을 영리 목적으로 이용할 수 없습니다.



변경금지. 귀하는 이 저작물을 개작, 변형 또는 가공할 수 없습니다.

- 귀하는, 이 저작물의 재이용이나 배포의 경우, 이 저작물에 적용된 이용허락조건을 명확하게 나타내어야 합니다.
- 저작권자로부터 별도의 허가를 받으면 이러한 조건들은 적용되지 않습니다.

저작권법에 따른 이용자의 권리는 위의 내용에 의하여 영향을 받지 않습니다.

이것은 [이용허락규약\(Legal Code\)](#)을 이해하기 쉽게 요약한 것입니다.

[Disclaimer](#)

공학박사학위논문

자가치료 고분자 복합재의 멀티스케일
기계적 해석

Multiscale mechanical analysis of self-healing
polymer composites

2017 년 2 월

서울대학교 대학원

기계항공공학부

신 현 성

자가치료 고분자 복합재의 멀티스케일 기계적 해석

Multiscale mechanical analysis of self-healing
polymer composites

지도교수 조 맹 효

이 논문을 공학박사 학위논문으로 제출함

2016 년 10 월

서울대학교 대학원

기계항공공학부

신 현 성

신현성의 공학박사 학위논문을 인준함

2016 년 12 월

위 원 장 : _____

부위원장 : _____

위 원 : _____

위 원 : _____

위 원 : _____

ABSTRACT

In this dissertation, a multiscale mechanical analysis of self-healing polymer composites has been conducted. Recently, the biomimetic self-healing polymeric systems have been focused due to their high healing efficiency. In spite of this attractive merit, these systems have critical limitations on the weakened effective stiffness and the fracture toughness as the weight fraction of microcapsules including the healing agent increases. To make up for this weakness, the “self-healing polymer composites” has been developed by addition of rigid nanoparticles or thermoplastic polymers into the self-healing polymers. However, the experiments-based optimal design of self-healing polymer composites cannot be achieved because there are too many design variables due to multi-compositions, and complex mechanical behaviors to be elucidated. Therefore, the multiscale mechanical analysis method for self-healing polymer composites is proposed for the efficient, reliable, and rational design.

The mechanics of self-healing polymer composites is very complex due to the combination of the toughening mechanisms and the macroscopic crack healing behaviors. To achieve the objective of this study, the following two theoretical models are developed. Firstly, "the multiscale model of self-healing polymers" is developed to predict the elastic properties, virgin fracture toughness, and healed fracture toughness of self-healing polymers as the weight fraction of microcapsules increases. To describe the adhesive behaviors between healing agents and matrix and mechanical behaviors of interface during the mechanical healing of

macroscopic cracks, the curing kinetics model and the full atomistic molecular dynamics simulations are merged. Secondly, "the multiscale continuum model near the macroscopic cracks", which can predict the toughness enhancement due to the addition of rigid nanoparticles and thermoplastic polymers, has been developed. The fracture toughness is highly related to the dissipated energy. To obtain the toughness enhancement, the dissipated microscopic energy is quantified using the proposed multiscale models. Using the multiscale model of self-healing polymers, the stress fields near the macroscopic cracks can be obtained during the healing of macroscopic cracks. Based on these stress fields, the fracture toughness enhancement can be predicted during the healing of macroscopic cracks. Finally, the multiscale mechanical analysis method of self-healing polymer composites has been developed.

Keywords

Self-healing polymers; Polymer nanocomposites; Multiscale analysis; Fatigue and fracture analysis; Finite element analysis; Molecular dynamics simulation

Student Number: 2011-20720

TABLE OF CONTENTS

1. INTRODUCTION	1
1.1. Multiscale Model of Self-Healing Polymers.....	1
1.2. Multiscale Analysis of Self-Healing Polymer Nanocomposites	2
1.3. Multiscale Analysis of Self-Healing Epoxy/Thermoplastic Blends.....	4
1.4. Outline of the Thesis	6
2. MULTISCALE MODEL OF SELF-HEALING POLYMERS	14
2.1. Model and Methods.....	15
2.1.1. Molecular modeling of bulk unit cells	15
2.1.1.1. Construction of crosslinked self-healing agents	15
2.1.1.2. Construction of crosslinked epoxy networks	16
2.1.1.3. Details of in-situ polymerization in molecular dynamics simulations.....	16
2.1.2. Curing kinetics model of self-healing agents.....	18
2.1.3. Characterization of mechanical behaviors of bulk unit cells	19
2.1.3.1. Elastic properties.....	19
2.1.3.2. Nonlinear stress-strain curves	20
2.1.3.3. Cohesive zone between healing agents and crosslinked epoxy ...	21
2.1.4. Characterization of mechanical behaviors of self-healing polymers ...	21
2.1.4.1. The homogenized elastic properties.....	21
2.1.4.2. The healed fracture toughness.....	22
2.2. Simulation Results and Discussions.....	23
2.2.1. Molecular dynamics simulation results of bulk healing agents	23
2.2.2. Predictive multiscale model of self-healing polymers	25
2.2.3. Time response of healing behaviors of self-healing polymers.....	26
2.3. Chapter Summary and Conclusions	27

3. MULTISCALE ANALYSIS OF SELF-HEALING POLYMER

NANOCOMPOSITES	36
3.1. Multiscale Model to Predict Fatigue Crack Growth of Thermoset Polymer	
Nanocomposites	37
3.1.1. Description of the multiscale-multimechanism strategy	37
3.1.2. Quantification of additive strain energy release rate due to toughening mechanisms.....	39
3.1.2.1. Nanoparticulate debonding-induced plastic yield of nanovoids ..	39
3.1.2.2. Localized shear banding	41
3.1.3. The overall strain energy release rate of the thermoset polymer nanocomposites.....	42
3.1.4. The prediction of overall fracture toughness of thermoset polymer nanocomposites.....	42
3.1.5. The prediction of overall fatigue crack propagation behaviors of thermoset polymer nanocomposites.....	43
3.1.5.1. without consideration of crack closure effect	43
3.1.5.2. with consideration of crack closure effect	44
3.1.6. Model validation by comparison with experimental data	45
3.1.6.1. System details for model validation.....	45
3.1.6.2. Experimental validation without crack closure effect.....	45
3.1.6.3. Influences of crack closure effects.....	46
3.2. Multiscale Analysis of Self-Healing Polymer Nanocomposites	48
3.3. Chapter Summary and Conclusions	49

4. MULTISCALE ANALYSIS OF SELF-HEALING

EPOXY/THERMOPLASTIC BLENDS	57
4.1. Multiscale Model of Epoxy/Thermoplastic Blends and Experimental Validations	57
4.1.1. Motivations	57
4.1.2. Thermoplastic particle yield-induced toughness enhancement.....	58
4.1.2.1. Description of the plastic energy from thermoplastic particles....	58

4.1.2.2. Modeling of toughness enhancement induced by thermoplastic particle yield	62
4.1.3. Thermoplastic particle bridging-induced toughness enhancement	64
4.1.4. Molecular modeling and molecular dynamics simulation of bulk polyethersulfone	65
4.1.4.1. Molecular modeling of bulk polyethersulfone	65
4.1.4.2. Simulation of triaxial tensile loading and unloading in bulk polyethersulfone	66
4.1.5. Simulation results and discussion	66
4.1.5.1. Molecular dynamics simulation results of polyethersulfone	66
4.1.5.2. Experimental validation of the proposed multiscale model	67
4.1.5.3. Dependence of the toughness enhancement on mechanical properties of thermoplastic particles	68
4.2. Multiscale Analysis of Self-Healing Epoxy/Thermoplastic Blends	69
4.3. Chapter Summary and Conclusions	70
5. CONCLUSIONS	78
APPENDIX A. STATISTICAL MULTISCALE HOMOGENIZATION	
APPROACH FOR ANALYZING POLYMER NANOCOMPOSITES THAT INCLUDE MODEL INHERENT UNCERTAINTIES OF MOLECULAR DYNAMICS SIMULATIONS	
81	
A.1. Introduction	81
A.2. Molecular Modeling and Simulation Methodology	84
A.2.1. Preparation of unit cell	84
A.2.2. Production run for elastic properties	86
A.2.3. Statistical analysis of epoxy nanocomposites	86
A.3. Statistical Multiscale Bridging Method	87
A.3.1. Brief review of previous multiscale bridging methodologies	87
A.3.2. Numerical algorithm for statistical multiscale bridging	89
A.3.3. Statistical analysis that considers filler geometric uncertainties	90
A.3.3.1. RVE setup	90

A.3.3.2. Review of two-scale homogenization method of linear elastic composites	92
A.4. Simulation Results and Discussion	93
A.4.1. Cumulative average response of Young's moduli	93
A.4.2. Mean and standard deviation of nanocomposite elastic properties	94
A.4.3. Uncertainties of interphase elastic properties.....	97
A.4.4. Propagation of inherent uncertainties of MD model	99
A.4.4.1. Verification of statistical three-phase multi-inclusion model through monoparticulate nanocomposites	99
A.4.4.2. Determination of RVE size and influence of geometric uncertainties	99
A.4.4.3. Discussion concerning the influence of inherent uncertainties of the MD model on the homogenized elastic properties of RVE	100
A.5. Summary of Appendix A	103

APPENDIX B. A MULTISCALE HOMOGENIZATION OF POLYMER NANOCOMPOSITES THAT INCLUDE AGGLOMERATED NANOPARTICLES	120
B.1. Introduction	120
B.2. Characterization of the Percolated Interphase Zone near the Agglomerated Nanofillers in Polymer Nanocomposites	122
B.2.1. Molecular modeling and simulation results	122
B.2.2. Multiscale homogenization modeling and verification	126
B.3. Homogenization Analysis of Polymeric Nanocomposites Containing Nanoparticulate Clusters	131
B.3.1. Models and methods.....	131
B.3.3.1. Preparation of finite element unit cells.....	131
B.3.3.2. Multiscale modeling of equivalent cluster	133
B.3.2. Homogenization results of polymeric nanocomposites unit cells including single clusters of nanoparticles	134
B.3.3. Homogenized elastic model of equivalent cluster and verification ...	136
B.4. Summary of Appendix B.....	137

REFERENCES	160
국문 요약.....	175

LIST OF TABLES

Table 3.1	Material properties of polymer nanocomposites used in the present analysis	50
Table 4.1	Comparison of linear elastic properties and glass transition temperature (T_g) of polyethersulfone obtained from molecular dynamics simulation with experimental literature	71
Table 4.2	Effect of stress-strain characteristics on the improvement in fracture toughness of a thermoplastic/epoxy composites at fixed fracture energy. (The critical radius of the yielded domain is normalized by the critical radius of the partially yielded domain at $m_x=m_y=1$.).....	72
Table A.1	Overview of model to understand how uncertainty that stems from initial velocity distribution of individual atoms is propagated to homogenized elastic properties of representative volume element that includes 30 nanoparticles	105
Table A.2	Chemical composition of crosslinked epoxy and crosslinked epoxy/SiC nanocomposites in MD simulation.....	106
Table A.3	Determination of interphase thickness from the result of a previous study [48] where r_p and t_{int} denote the nanoparticulate radius of SiC and the corresponding interphase thickness, respectively	107
Table A.4	The proposed algorithm to obtain probability distributions of the elastic properties of the interphase from MD and multi-inclusion results	108
Table A.5	Statistical parameters (mean, standard deviation, and coefficient of variation) of elastic properties obtained from MD simulation compared with those of other studies. V_f is the volume fraction of the filler.....	109

Table A.7	Homogenized Young's moduli of polydisperse multi-particulate nanocomposite systems that include various numbers of inclusions to determine the proper number of representative volume elements (RVE)	111
Table A.8	Influence of propagation of inherent uncertainties of the MD model on the homogenized Young's moduli of polydisperse multi-particulate nanocomposite systems	112
Table B.1	Longitudinal elastic properties of molecular system and corresponding interphase characteristics for various interparticulate distances ($r_p = 9.00 \text{ \AA}$)	139
Table B.2	Longitudinal elastic properties of the molecular system and the corresponding interphase characteristics for various interparticulate distances ($r_p = 5.18 \text{ \AA}$)	140
Table B.3	Centroids of each particle in the multiparticulate nanocomposite system.....	141
Table B.4	Elastic moduli of the multiparticulate nanocomposite obtained using various approaches	142
Table B.5	Homogenization results of polymeric nanocomposites unit cell including single cluster of nanoparticles	143
Table B.6	Geometry and elastic properties of equivalent clusters	144
Table B.7	Verification of the equivalent cluster approach	145

LIST OF FIGURES

Figure 1.1	A schematic diagram for description of self-healing mechanism.....	10
Figure 1.2	A schematic diagram of the microscopic energy dissipating mechanisms near the macroscopic crack tip and representative volume elements for the micromechanics analysis	11
Figure 1.3	A schematic diagram of the toughness enhancements mechanisms of thermoplastic/epoxy blends.....	12
Figure 1.4	The proposed multiscale approach to model the toughness enhancement induced by particle yield near a macroscopic crack in a thermoplastic/epoxy blend	13
Figure 2.1	Schematic of the reaction mechanism for ring-opening metathesis polymerization (ROMP) of dicyclopentadiene (DCPD) into a cross-linked polymer network: (a) DCPD monomer, (b) DCPD monomer that has experienced the opening of norbornene ring, which play a role as linear segment, (c) DCPD monomer that has experienced both the opening of norbornene ring and cyclopentene ring, which play a role as cross-linker, and (d) polymer networks of pDCPD. (Here, (b) and (c) exclude configuration of hydrogen bonds)	28
Figure 2.2	Unit cell configuration of crosslinked DCPD networks: (a) 26% crosslinking ratio, and (b) 96% crosslinking ratio. (crosslinked sites are highlighted by red colors).....	29
Figure 2.3	Bilayer unit cell models for characterization of cohesive zone model between polydicyclopentadiene (pDCPD) networks and epoxy networks	30
Figure 2.4	Molecular dynamics simulation results on mechanical behaviors of bulk healing agents: (a) Young's moduli, and (b) nonlinear stress-strain curves	31

Figure 2.5	Molecular dynamics simulation results on enthalpy of bulk healing agents.....	32
Figure 2.6	Effective mechanical properties of self-healing polymers: (a) homogenized elastic properties and experimental validation, (b) descriptive model of virgin fracture toughness, and (c) predictive model of healed fracture toughness.....	33
Figure 2.7	Mode I traction-separation behaviors of bilayer model between polydicyclopentadiene (pDCPD) networks and epoxy networks.....	34
Figure 2.8	Curing kinetics model: (a) the relationship between enthalpy-based curing ratio and actual curing ratio, (b) time response of enthalpy-based curing ratio, and (c) time response of actual curing ratio.....	35
Figure 3.1	Predicted mechanical properties of polymer nanocomposites and experimental validations: (a) elastic properties, (b) critical stress intensity factors, and (c) critical strain energy release rate. The details of experimental data can be found in Ref. 11.....	51
Figure 3.2	Fatigue crack growth behaviors of polymer nanocomposites: (a) predicted results using the proposed method without crack closure effect, (b) experimental results [11], predicted results with crack closure effects of (c) $K_{I,cl}=0.05 \text{ MPa} \cdot \text{m}^{1/2}$, (d) $K_{I,cl}=0.10 \text{ MPa} \cdot \text{m}^{1/2}$, (e) $K_{I,cl}=0.15 \text{ MPa} \cdot \text{m}^{1/2}$, (f) $K_{I,cl}=0.20 \text{ MPa} \cdot \text{m}^{1/2}$	52
Figure 3.3	Fatigue crack propagation behaviors of polymer nanocomposites: (a) crack extension-the number of load cycles curve, and (b) fatigue life (at $K_{I,cl}=0.20 \text{ MPa} \cdot \text{m}^{1/2}$).....	53
Figure 3.4	An influence of crack closure effects on the (a) m_{comp} , (b) ΔK_{th} , and (c) ΔK_{th} as a function of nanoparticulate contents and comparison with experimental data [11].....	54

Figure 3.5	Schematics of self-healing polymer nanocomposites: (a) virgin toughness, and (b) healed toughness	55
Figure 3.6	Basic mechanical properties of self-healing polymer nanocomposites: (a) elastic properties, (b) virgin fracture toughness, and (c) healed fracture toughness	56
Figure 4.1	Molecular modeling of polyethersulfone: (a) chemical structure of polyethersulfone [57], (b) monomer of polyethersulfone molecule, and (c) configuration of amorphous unit cell with five polyethersulfone chains.....	73
Figure 4.2	Stress-strain response of triaxial tensile simulation of polyethersulfone: (a) molecular dynamics data, and (b) fitted curve ..	74
Figure 4.3	Validation of multiscale model compared to experimental data [84,85]	75
Figure 4.4	Curve of hydrostatic stress versus volumetric strain of thermoplastic particles magnified view along strain direction (constant fracture energy)	76
Figure 4.5	Basic mechanical properties of self-healing epoxy/thermoplastic blends: (a) elastic properties, (b) virgin fracture toughness, and (c) healed fracture toughness	77
Figure A.1	Molecular modeling: (a) Polymer nanocomposite unit cell with spherical silicon carbide (SiC) filler, and (b) crosslinked epoxy network (crosslinking ratio, 0.61)	113
Figure A.2	Major model uncertainties: (a) uncertainties that stem from chaotic flow of molecules during ensemble averages; (b) randomness of initial ensemble velocity distribution despite identical macroscopic temperature; and (c) lognormal distribution of the obtained elastic properties of polymer nanocomposites including single particles (radius = 5.18 Å)	114

Figure A.3	Statistical multiscale bridging method that reflects inherent uncertainty of MD model	115
Figure A.4	Representative volume element (RVE) with 30 nanoparticles and corresponding interphase inside the matrix phase. DIGIMAT [®] was used for modeling CAD geometry of randomly distributed nanoparticles and corresponding interphase. (a) Finite element model (Figure includes mesh configuration of matrix and particle only), and (b) probability density distribution of particle radii	116
Figure A.5	Cumulative average of normalized Young's moduli for polymer nanocomposites	117
Figure A.6	Comparison of nanocomposites elastic properties between statistical multiscale bridging method and molecular dynamics simulation to validate the proposed statistical multiscale bridging method.....	118
Figure A.7	Influence of uncertainty in the material properties of each spring on the mean material property of the effective spring element	119
Figure B.1	Multiscale homogenization strategy of polymeric nanocomposites containing the clustered nanoparticles: (a) TEM image of silica nanocomposites [125], (b) direct modeling, and (c) equivalent cluster modeling.....	146
Figure B.2	Cross section of nanocomposite molecular model and equivalent finite element model (HNR. II): (a) MD model, and (b) Finite element model.....	147
Figure B.3	(a) Definition of interparticular region for the structural analysis B: overlap region, C: gallery region. (b) Density profile of PP molecules of slab A (HNR. II, $d = 4.7\text{\AA}$)	148
Figure B.4	The proposed percolation interphase model: interphase Young's modulus when the nanoparticulate radius is (a) $r_p=9.00\text{\AA}$, and (b) $r_p=5.18\text{\AA}$, and corresponding longitudinal elastic modulus of nanocomposites predicted from the two-scale homogenization method using the interphase percolation model: (c) $r_p=9.00\text{\AA}$, and (d) $r_p=5.18\text{\AA}$.	149

Figure B.5	A multiparticulate nanocomposite systems that includes four agglomerated nanoparticles: (a) TEM image of silica nanocomposites [125], (b) MD model, and (c) equivalent finite element model (Figure includes mesh configuration of matrix and particle only).....	150
Figure B.6	Finite element models of a single cluster of nanoparticles for different numbers of nanoparticles (4, 10, 18, and 30) at a fixed volume fraction (3%) and radii (9Å) of nanoparticles (the schematics include a mesh configuration of the interphase only)	151
Figure B.7	Schematics representation of the flow diagram of the processing steps used to determine the coordinates of the clustered nanoparticles	152
Figure B.8	Interaction energy between interparticles.....	153
Figure B.9	The schematics of the equivalent cluster-based homogenization approach	154
Figure B.10	Variation of the radius of the cluster with respect to the number of clustered nanoparticles at a nanoparticulate radius of 9Å when nanoparticles are closely-packed.....	155
Figure B.11	Characteristics of percolated interphase zone: (a) volume fraction of interphase and overlapping density, and (b) Young’s moduli of percolated interphase zone	156
Figure B.12	Homogenization results of polymeric nanocomposites unit cell including single cluster of nanoparticles: (a) Young’s modulus, and (b) shear modulus.....	157
Figure B.13	Various types of elastic model of overlapped interphase zone	158
Figure B.14	Finite element models of polymeric nanocomposites including the clustered nanoparticles: (a) direct computation, and (b) equivalent cluster-based approach (figures include only the mesh configuration of the interphase)	159

1. INTRODUCTION

1.1. Multiscale Model of Self-Healing Polymers

Self-healing polymeric materials have been focused as a new route to safer and longer-lasting polymeric materials and structures. Self-detects and repairs of the intrinsic damage enables to continue mechanical performances of polymer-based industrial systems. In the initial stage, thermal interdiffusion and solvent-mediated interdiffusion are key ideas of self-healing polymeric systems [1-3]. However, interdiffusion-based healing systems are not focused due to slow healing behaviors that come from low mobility of polymeric chains. White et al. proposed innovative self-healing systems by embedding the microencapsulated self-healing agents [4-6], as shown in Fig. 1.1. It mimics the self-healing biomimetic systems that blood coagulates around the wound. The approaching microcracks rupture the embedded microcapsules, and healing agents are released into the crack plane through capillary action. The dispersed catalysts in the matrix enable the autonomous polymerization of healing agents, and bond the crack faces.

These autonomous self-healing procedures of the embedded microcapsules are a typical multiscale mechanical stimuli-response process [7]. Even though a lot of studies on the self-healing chemistries, such as the curing kinetics of healing agents for different concentrations of catalysts and manufacturing procedures of microcapsules with precise control of radius and thickness of microcapsules, have been achieved, the multiscale models for the prediction of elastic properties, virgin fracture toughness, and healed fracture toughness have not been reported. The

development of these predictive multiscale models can be applied for the proper selection of the weight fraction of microcapsules. Meanwhile, the theoretical predictive model for the maximum healing efficiency of self-healing polymers has not been treated, even though it can provide useful guideline for the material design such as the selection of healing agents. Moreover, the predictive model for the time response of healing behaviors of self-healing polymers for different amount of catalysts can be used as the indicators for the determination of concentrations of catalysts.

1.2. Multiscale Analysis of Self-Healing Polymer Nanocomposites

Self-healing polymers have weak mechanical properties (elastic properties and virgin toughness) due to low stiffness and fracture toughness of healing agents-filled microcapsules at the liquid states. To overcome this weak point of self-healing polymer nanocomposites, nanoparticles (e.g., carbon nanotube) are embedded into the self-healing materials as hybrid multiscale composite systems [8]. However, the determination of master curves for various concentrations of microcapsules and nanoparticles is hard due to the difficulty on the interpretation due to the manufacturing uncertainties during the material processing and production such as nanoparticulate dispersion and size distribution. Therefore, the development of the multiscale model to predict mechanical behaviors (elastic properties, fracture toughness, and fatigue crack growth behaviors) will be very useful for the mechanical design.

Rigid nanoparticles have attracted attention as good candidates to enhance the mechanical properties of thermoset polymer-based composites. It has been reported

that the addition of rigid nanoparticles increases the cyclic-fatigue crack propagation behavior [9-11] of the polymer nanocomposites as well as the stiffness [12-18], yield strength [19-21], and fracture toughness [22-30]. While the numerous experimental and theoretical model studies have been studied for the stiffness, yield strength, and quasi-static fracture toughness of thermoset polymer nanocomposites, there are very few studies about the fatigue crack growth behaviors [9-11].

Blackman et al. [9] investigated the fracture and fatigue behavior of epoxy-based nanocomposites. The addition of nano-silica particles has clearly enhanced the cyclic-fatigue behavior of epoxy-based nanocomposites as well as fracture toughness. The threshold value of fatigue crack propagation is improved as the filler concentration increases. Recently, Kothmann et al. [11] investigated the fatigue crack growth behaviors of silica nanoparticles-filled epoxy resins in all three stages of fatigue crack growth. Fractographic analysis of the fracture surfaces was carried out to observe the major energy dissipating mechanisms for the enhancement of fatigue crack growth behaviors. In spite of low ΔK_I values, neither crack deflection nor crack bridging was observed because the estimated size of the crack tip opening displacement is more than order of magnitude larger than the particulate radius [31]. It was concluded that the main mechanisms are interfacial debonding-induced plastic nanovoid growth and shear banding between nanoparticles in every fatigue crack propagation regimes, which are same with the well-understood toughening mechanisms [22-30]. The experimental characterization of fatigue crack growth involves huge efforts and time including the massive experimental tests, and difficulty on the interpretation due to the

manufacturing uncertainties during the material processing and production such as nanoparticulate dispersion and size distribution. Therefore, the development of multiscale model to predict fatigue crack propagation behavior of thermoset polymer nanocomposites is useful and essential, as shown in Fig. 1.2.

Meanwhile, the self-healing polymer nanocomposites are the heterogeneous materials including the two different scale inclusions. The mechanics of self-healing polymer nanocomposites has the complexity due to the combination of the extrinsic crack shielding mechanisms inside the macroscopic cracks due to the adhesion between healing agents and epoxy networks, and extrinsic toughening mechanisms that come from the microscopic energy dissipation due to the reinforced nanoparticles. Therefore, the multiscale models of self-healing nanocomposites have to include both mechanisms for the mechanical description, and it is necessary for material analysis of self-healing polymer nanocomposites.

1.3. Multiscale Analysis of Self-Healing Epoxy/Thermoplastic Blends

In spite of intrinsic healing nature of self-healing epoxy systems, the low virgin fracture toughness and healed fracture toughness are still limitations on the material design of self-healing epoxy-based systems due to intrinsic brittleness of highly crosslinked epoxy. For the purpose of the enhancement of virgin fracture toughness and healed fracture toughness, some studies have been conducted by blending thermoplastic particles into the self-healing epoxy systems [32]. However, the determination of master curves for various concentrations of microcapsules and thermoplastic particles is hard due to the difficulty on the interpretation due to the manufacturing uncertainties during the material processing and production such as

nanoparticulate dispersion and size distribution. In this chapter, the multiscale models to predict elastic properties, and fracture toughness of epoxy/thermoplastic blends are proposed, which are applied to the prediction of mechanical behaviors (elastic properties, virgin fracture toughness, and healed fracture toughness) of self-healing epoxy/thermoplastic blends.

A highly crosslinked epoxy system has excellent properties such as good thermal stability, creep resistance, excellent adhesion properties, and relatively high modulus [33]. However, the high crosslink density leads to low fracture toughness, and inferior impact strength, which limit their application in high performance areas such as the automotive, aerospace, and defense industries [34]. Therefore, it has been a challenging issue to improve the fracture toughness of an epoxy by modifying the resin with a secondary phase such as rubber [35-37], thermoplastic [38-42], and inorganic particles [24,43,44]. In particular, thermoplastic/epoxy blends are widely employed, because the high toughness enhancement through modification by the thermoplastic was not accompanied by critical reduction in the elastic modulus [38,40]. Despite the importance of thermoplastic-toughened epoxy systems in various sectors, there have been insufficient studies to predict the toughness enhancement by thermoplastic polymers as the secondary phase [41].

Based on the experimental observations, it was reported that the ductile thermoplastic particle plays two key roles in toughening mechanism of thermoplastic/epoxy blends plastic deformation in the material near the macroscopic crack tip, and particle bridging in the crack wake [45,46], as shown in Fig. 1.3. For the first mechanism, multiscale approach [26-28] is useful when developing an analytical model with an infinite number of particles embedded in

the matrix domain. The density of energy dissipated by the damage mechanism of the representative volume element (RVE) near the crack tip can be described by micromechanics models as shown in Fig. 1.4. The fracture toughness enhancement of the composites can be obtained quantitatively through the J -integral near the macroscopic crack tip [29]. However, multiscale models for the toughness enhancements of thermoplastic/epoxy blends have not been reported, unlike rigid nanoparticles [26,27]. For this reason, we focused on the development of a model to describe the fracture toughness improvement by thermoplastic particle yield near the crack tip. The main objective of the present paper is to quantify the toughness enhancement due to the plastic yield of the thermoplastic particle.

Meanwhile, the self-healing epoxy/thermoplastic blends are the heterogeneous materials including the two different scale inclusions. The mechanics of self-healing epoxy/thermoplastic blends has the complexity due to the combination of the extrinsic crack shielding mechanisms inside the macroscopic cracks due to the adhesion between healing agents and epoxy networks, and extrinsic toughening mechanisms that come from the microscopic energy dissipation due to the plastic yield of toughening agents. Therefore, the multiscale models of self-healing epoxy/thermoplastic blends have to include both mechanisms for the mechanical description, and it is necessary for the material design of self-healing epoxy/thermoplastic blends.

1.4. Outline of the Thesis

The main objectives of this thesis are the multiscale mechanical analysis of self-healing polymer composites (including self-healing polymer nanocomposites and

self-healing epoxy/thermoplastic blends). To achieve these objectives, we firstly develop the multiscale model of self-healing polymeric material systems including the homogenized elastic properties, virgin fracture toughness, and healed fracture toughness in **Chapter 2**. For the mechanical description of self-healing polymer systems in the molecular scales, the full atomistic molecular dynamics simulations are conducted to characterize the elasto-plastic behaviors of healing agents, and interfacial fracture toughness between healing agents and crosslinked epoxy for different curing ratio of healing agents. Using the multi-inclusion model, the homogenized elastic properties are obtained and validated with satisfactory agreement with the experimental reference data. Using the interfacial fracture toughness between healing agents and crosslinked epoxy, the healed fracture toughness of self-healing polymer systems is theoretically characterized for different curing ratio of healing agents. Using the experimentally quantified curing kinetics of healing agents, the necessary times for the enough extrinsic healing of macroscopic cracks are characterized for different concentrations of catalysts. Additionally, the maximum theoretical healing efficiency is also provided. After the development of the multiscale model of self-healing polymer systems, the multiscale analysis of self-healing polymer nanocomposites and self-healing epoxy/thermoplastic blends are conducted.

For the multiscale mechanical analysis of self-healing polymer nanocomposites, the microscopic energy dissipating mechanisms due to the embedded nanoparticles and the extrinsic crack healing mechanisms within the macroscopic cracks should be considered. In **Chapter 3**, we firstly develop the multiscale model to predict fatigue crack propagation behaviors of thermoset polymer nanocomposites using

the multiscale-multimechanism strategy. Here, the experimentally observed microscopic energy dissipating mechanisms (interfacial debonding, the subsequent plastic nanovoid growth, and shear banding) are considered. Theoretical predictions for the fatigue crack growth of thermoset polymer nanocomposites are compared with experimental data of the literature, which shows a satisfactory agreement. By the consideration of the extrinsic crack healing mechanisms, the multiscale mechanical analysis of self-healing polymer nanocomposites is conducted for various concentrations of microcapsules and nanoparticles. Here, the macroscopic crack healing mechanisms due to the adhesion between healing agents and epoxy networks are quantified by the full atomistic molecular dynamics simulations.

Similarly, **Chapter 4** focuses on the multiscale mechanical analysis of self-healing epoxy/thermoplastic blends. Firstly, we develop the multiscale model to predict fracture toughness of epoxy/thermoplastic blends using the multiscale-multimechanism strategy. Here, the experimentally observed microscopic energy dissipating mechanisms (the plastic yield of thermoplastic particles) are considered. Theoretical predictions for the fracture toughness of epoxy/thermoplastic blends are compared with experimental data of the literature, which shows a satisfactory agreement. To quantify the plastic dissipation energy of thermoplastic particles, the full atomistic molecular dynamics simulation is conducted to obtain the curve of nonlinear hydrostatic stress versus volumetric strain. Based on results obtained using the multiscale model, design guidelines regarding the proper selection of toughening agents are proposed for enhancing the fracture toughness of thermoplastic/epoxy blends. By the consideration of the extrinsic crack healing

mechanisms, multiscale mechanical analysis of self-healing epoxy/thermoplastic blends is conducted for various concentrations of microcapsules and thermoplastic particles. Here, the macroscopic crack healing mechanisms due to the adhesion between healing agents and epoxy networks are quantified by the full atomistic molecular dynamics simulations. Here, the macroscopic crack healing mechanisms due to the adhesion between healing agents and epoxy networks are quantified by the full atomistic molecular dynamics simulations.

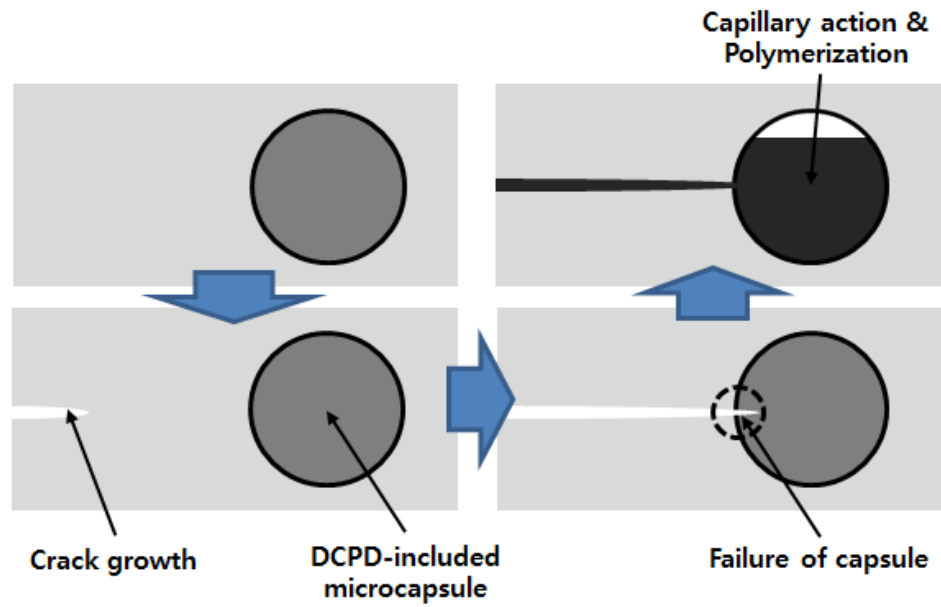
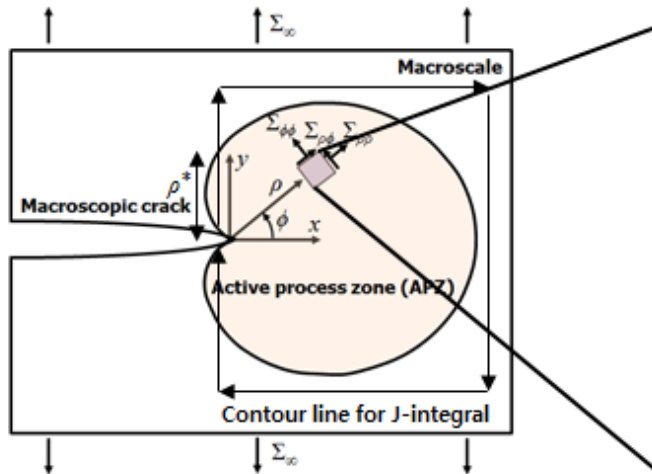


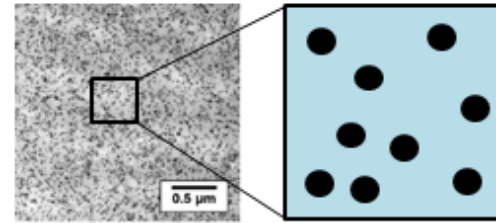
Fig. 1.1. A schematic diagram for description of self-healing mechanism

Macroscale continuum analysis

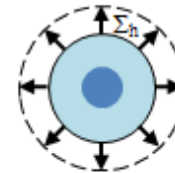


Microscale continuum analysis

Representative volume element



Debonding mechanism



Shear band mechanism

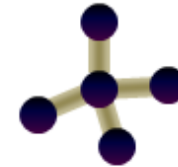


Fig. 1.2. A schematic diagram of the microscopic energy dissipating mechanisms near the macroscopic crack tip and representative volume elements for the micromechanics analysis

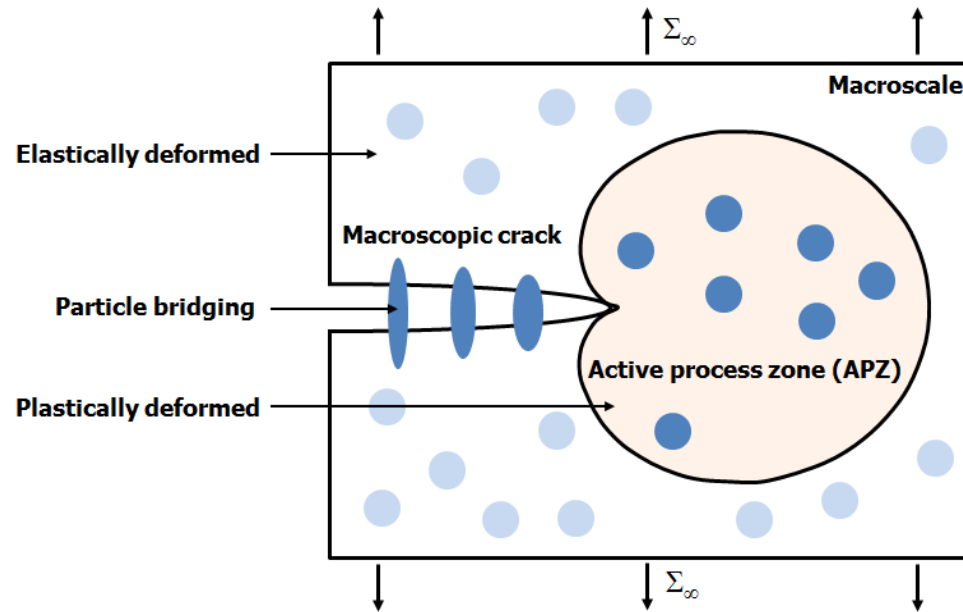


Fig. 1.3. A schematic diagram of the toughness enhancements mechanisms of thermoplastic/epoxy blends

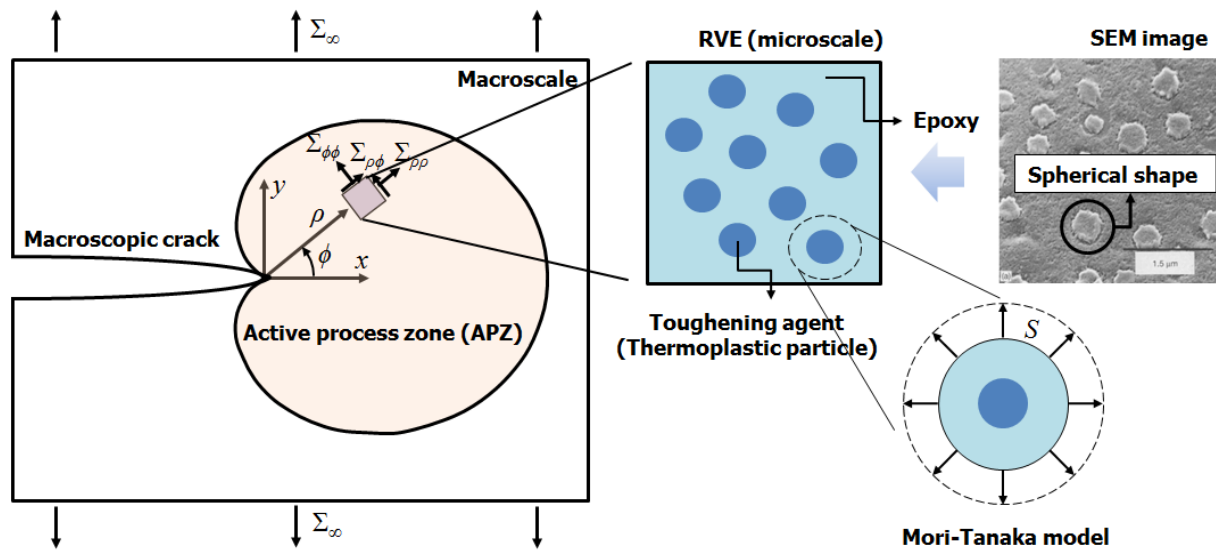


Fig. 1.4. The proposed multiscale approach to model the toughness enhancement induced by particle yield near a macroscopic crack in a thermoplastic/epoxy blends

2. MULTISCALE MODEL OF SELF-HEALING POLYMERS

In this chapter, a multiscale model of self-healing polymers that include the microencapsulated self-healing agents is developed. Here, the crosslinked epoxy and the polydicyclopentadiene (pDCPD) are employed as the host material and healing agents, respectively. The major objectives of this study can be summarized as follows:

- To predict the maximum theoretical healing efficiency of self-healing polymers
- To predict the time response of the mechanical behaviors of self-healing polymers using the curing kinetics and the reactive mechanism of healing agents
- To establish foundation of multiscale analysis of self-healing composites including the nanoparticles and the thermoplastic particles

With these purposes, the molecular dynamics simulations are carried out for the characterization of mechanical behaviors of bulk pDCPD networks and epoxy networks, and cohesive zone model between pDCPD networks and epoxy networks is obtained. Using these simulation results, the predictive multiscale models that consider the homogenized elastic properties and fracture toughness of virgin and healed states are developed.

2.1. Model and Methods

2.1.1. Molecular modeling of bulk unit cells

2.1.1.1. Construction of crosslinked self-healing agents

The reactive mechanism for ring-opening metathesis polymerization (ROMP) of dicyclopentadiene (DCPD) is schematically described in the Fig. 2.1. The DCPD monomer includes two cyclic olefins (norbornene and cyclopentene rings). It was reported that the opening of cyclopentene ring occurs after the norbornene ring is opened [47]. During the ROMP of DCPD, the pDCPD networks can be simplified as the following three types of components:

- Monomer in which no ring-opening procedure has been undergone, Fig. 2.1 (a)
- Linear segment in which the only norbornenic ring has been opened, Fig. 2.1 (b)
- Crosslinker structure in which both the cyclopentenic and norbornenic rings have undergone the opening of rings, Fig. 2.1 (c)

The reactive sites of DCPD monomer are described in Fig. 2.1 (a). The openings of norbornenic ring and cyclopentenic ring make two reactive sites (R1 and R2 in norbornenic ring, and R3 and R4 in cyclopentenic ring), respectively. There are three pairs of crosslinks between two reactive sites (R1-R2, R2-R3, and R1-R4).

Using these reactive mechanisms, the pDCPD networks (Fig. 2.1 (d)) are constructed before the molecular dynamics simulations. The idealized unit cell that includes the uncrosslinked healing agent molecules is initially constructed in an amorphous state with periodic boundary conditions, whose details are listed in Table 2.1. Here, the crosslinking ratio is defined as the number of reactions over the number of possible reactive sites. An initially defined density of bulk unit cells

is set as 0.7 g/cc. The pDCPD unit cells are prepared with varying crosslink densities of 12.6, 40.6, 56.6, 69.8, and 85.2%, respectively. The details of intermolecular distance-based polymerization procedures in molecular dynamics simulations are described in the following subsection (section 2.1.1.3).

2.1.1.2. Construction of crosslinked epoxy networks

The molecular models of an epoxy resin (EPON862[®]) compound and a hardener (TETA[®]) compound for curing the resin are considered as a host polymer [48]. The idealized unit cell of uncrosslinked polymer that contains the resin and hardener molecules is initially constructed in an amorphous state with periodic boundary conditions. The ratio of resin to hardener in the modeled unit cell is 3:1 in order to provide a satisfactory number of chemical reactive sites for the two molecules available for crosslinking (four nitrogen atoms in the single hardener molecule can be reacted with up to six carbon atoms of the epoxide rings). In this study, the only fully crosslinked epoxy networks are considered.

2.1.1.3. Details of in-situ polymerization in molecular dynamics simulations

The in-situ polymerization approach [13,49-51] is used to generate the pDCPD networks and epoxy networks. Using the predefined polymerization mechanisms (section 2.1.1.1 & 2.1.1.2), the formation of crosslinking networks is carried out in the full atomistic molecular dynamics models. Every molecular modeling of the complex atomic structures is carried out using the commercial molecular dynamics simulation package, Materials Studio 5.5 (Accelrys[®] Inc.). Both the bonding and non-bonding interactions between the adjacent atoms are represented by the

polymer-consistent force field (PCFF) potential [52]. For the efficient calculation of the electrostatic potential energy, the distance-dependent dielectric method with a constant of 1.6 is applied in order to ensure that the values of the mechanical response of the current model are similar to those in the literature [13,48-50].

The idealized unit cell of uncrosslinked polymer that includes the healing agent molecules or epoxy resins and curing agents is initially constructed in an amorphous state with periodic boundary conditions. The uncrosslinked polymer unit cells undergo energy minimization of its total potential energy by using a conjugated gradient method with an energy deviation convergence cutoff of 0.1 kcal/mol·Å, followed by an NVT (isothermal) ensemble simulation at 300 K for 500 ps and NPT (isothermal–isobaric) ensemble simulation at 300 K and 1 atm for 2 ns.

For simulation of the crosslinking reaction, all the interatomic distances between the reactive sites in a given unit cell are calculated. If the distance between the reactive sites is within the designated cutoff, a new covalent bond is artificially created between the sites. The reaction cutoff distance starts at the value of 1 Å, and gradually increases with the step size increment of 0.5 Å until the final crosslinking ratio is reached. The atomic structure is repeatedly minimized using a conjugated gradient method with refreshed potential energy components, while the reaction cutoff distance is iteratively updated. After the crosslinking procedure is completed, final equilibration runs are executed in an NVT ensemble simulation at 300 K for 2 ns, followed by an NPT ensemble at 300 K and 1 atm for 3 ns. As shown in Fig. 2.2, the inter-DCPDs crosslinks are uniformly distributed where the crosslinked sites are denoted by red colors.

It is worth noting that many other methods can be used for the modeling of the crosslink distribution in epoxy resin in the molecular dynamics simulation, such as representative network element generation [13,48-50] and real-time observation of the chemical reaction in a dynamic ensemble [51,53,54]. None of these models are perfect, each having its own merits and demerits and being limited only to the targeted properties under specific conditions. Nevertheless, it is generally known that these methods are all well correlated to the experimental methods on the thermal and mechanical behavior of the crosslinked epoxy.

2.1.2. Curing kinetics model of self-healing agents

The ring-opening metathesis polymerization (ROMP) is highly exothermic due to the release of ring strain energy [55]. The curing kinetics of DCPD was examined by Kessler *et al.* [55] for different concentrations of Grubbs' catalyst, which is ruthenium-based catalyst that shows high metathesis activity. The differential scanning calorimetry (DSC) was used to determine the curing kinetics of DCPD. The time response of enthalpy-based curing ratio was defined as the following form:

$$\alpha_H(t) = \frac{H(t)}{H_R} \quad (2.1)$$

where $H(t)$ is the enthalpy of reaction up to time t , and H_R is the total enthalpy of reaction. In the curing kinetics analysis, the rate of reaction is separated into the temperature-dependent rate constant, $K(T)$ and the reaction model, $f(\alpha_H)$.

$$\dot{\alpha}_H(\alpha_H, T; t) = K(T) \times f(\alpha_H) \quad (2.2)$$

Here, $K(T)$ and $f(\alpha_H)$ are defined as the following forms:

$$K(T) = A \cdot \exp\left(-\frac{E_a}{RT}\right) \quad (2.3a)$$

$$f(\alpha_H) = (1 - \alpha_H)^n \quad (2.3b)$$

where A is the pre-exponential factor, E_a is the activation energy, R is the universal gas constant, and T is the absolute temperature. In the molecular dynamics simulations, the description of crosslinking ratio based on the number of reaction is easier than the enthalpy-based description, which is used in the experimental characterization. Therefore, to bridge the experimental observation and the molecular dynamics description, the enthalpy of bulk unit cell of healing agents is characterized for various curing ratio.

2.1.3. Characterization of mechanical behaviors of bulk unit cells

2.1.3.1. Elastic properties

The elastic moduli of the bulk unit cells were obtained using the Parrinello-Rahman strain fluctuation method [56] combined with the $N\sigma T$ (constant stress) ensemble simulation, which allows both normal deformations and distortions of the simulation cells. The Parrinello-Rahman strain fluctuation is carried out using the commercial MD simulation package, Materials Studio 5.5 (Accelrys[®] Inc.) [57]. In the $N\sigma T$ ensemble simulation, diagonal components of the internal stress tensor were set at 1 atm (equivalent to atmospheric pressure condition) and fluctuations of both normal and shear strain components are stored to apply the strain fluctuation formula. In the strain fluctuation method, the elastic stiffness tensor C_{ijkl} of the unit cell is defined as,

$$C_{ijkl} = \frac{k_B T}{\langle V \rangle} \langle \delta \varepsilon_{ij} \delta \varepsilon_{kl} \rangle^{-1} \quad (2.4)$$

where ε_{ij} , V , and T are the strain tensor, volume, and temperature of the unit cell, respectively, and k_B is the Boltzmann constant. Here, the symbol $\langle \cdot \rangle$ indicates the ensemble average of physical quantity. To apply the fluctuation method, the bulk DCPD unit cells were again equilibrated at 300 K and 1 atm through the $N\sigma T$ ensemble simulation for 500 ps. As a final production run for the strain fluctuation data, the same $N\sigma T$ ensemble simulation was followed for 100 ps with the time step of 1 fs and all the thermodynamic quantities including the volume and strain fluctuations are stored at every 10 fs to apply Eq. (2.4). For the computational accuracy, the final production runs were repeated eight times and the elastic moduli of each unit cell were averaged over eight different simulation results.

2.1.3.2. Nonlinear stress-strain curves

The nonlinear stress-strain curves of bulk unit cells are estimated along the x , y , and z directions through uniaxial tensile loading simulations. The tensile simulations for the cases considered were carried out using the Large-Scale Atomic/Molecular Massively Parallel Simulator, an open source code (LAMMPS, Sandia Lab) [58]. According to the tensile tests, stresses for each atom in both the axial and transverse directions can be obtained. From an atomic viewpoint, the potential energy increase can be explained with an atomic stress tensor σ_{ij} based on the virial theorem defined as follows:

$$\sigma_{ij} = \frac{1}{V} \left(-\sum_i^N m_i \mathbf{v}_i \mathbf{v}_i^T + \frac{1}{2} \sum_i^N \sum_{j<i}^N r_{ij} F_{ij} \right) \quad (2.5)$$

where V is the atomic volume, N is the total number of atoms, \mathbf{v}_i and m_i are the thermal excitation velocity and the mass of atom i , respectively, \mathbf{r}_{ij} is the relative position between atoms i and j , and \mathbf{F}_{ij} is the atomic force on atom i due to atom j .

2.1.3.3. Cohesive zone between healing agent and crosslinked epoxy

For characterization of cohesive zone model between healing agent networks and crosslinked epoxy networks, periodic unit cell including bilayer model composed of healing agents and crosslinked epoxy networks is constructed as shown in Fig. 2.3. The total number of atoms is 22,228, and unit cell size is $42.16 \times 40.64 \times 136.35 \text{ \AA}^3$. During the molecular dynamics simulations for mode I separation behaviors, bottom layer (epoxy networks) is fixed and top layer (healing agent networks) is moved toward z-direction with velocity of 0.005 \AA/ps . Here, the Large-Scale Atomic/Molecular Massively Parallel Simulator, an open source code (LAMMPS, Sandia Lab) is employed for the molecular dynamics simulations [58].

2.1.4. Characterization of mechanical behaviors of self-healing polymers

2.1.4.1. The homogenized elastic properties

In this subchapter, the multi-inclusion model of Hori and Nemat-Nasser [59] is employed to characterize the homogenized elastic properties of self-healing polymers. The overall elastic stiffness tensor of a composite including the R number of phase is given as follows:

$$\mathbf{C}_{\text{comp}} = \mathbf{C}_{\text{inf}} \left[\mathbf{I} + (\mathbf{S} - \mathbf{I}) \left(\sum_{r=1}^R f_r \mathbf{\Phi}_r \right) \right] \left[\mathbf{I} + \mathbf{S} \left(\sum_{r=1}^R f_r \mathbf{\Phi}_r \right) \right]^{-1} \quad (2.6)$$

where \mathbf{C}_{inf} is the stiffness tensor of the infinite medium; f_r is the volume fraction of

the r th phase; and \mathbf{S} and \mathbf{I} are Eshelby's tensor and the identity tensor, respectively.

The eigenstrain concentration tensor of r th phase Φ_r is expressed as follows:

$$\Phi_r = \left[\left(\mathbf{C}_{\text{inf}} - \mathbf{C}_r \right)^{-1} \mathbf{C}_{\text{inf}} - \mathbf{S} \right]^{-1} \quad (2.7)$$

where \mathbf{C}_r is the stiffness tensor of the r th phase, and eigenstrain of r th phase $\boldsymbol{\varepsilon}_r^*$ could be represented by $\boldsymbol{\varepsilon}_r^* = \Phi_r \boldsymbol{\varepsilon}^0$ where $\boldsymbol{\varepsilon}^0$ is macroscopic strain. For the experimental validation, self-healing polymers that include microcapsule of 180nm thickness and 180 μm diameter is considered [60]. Here, the multi-inclusion model is composed of matrix ($r = 1$), filled healing agents ($r = 2$), and microcapsule ($r = 3$). Using the dilute concentration condition, \mathbf{C}_{inf} is assumed to have the same value with that of matrix domain, \mathbf{C}_{mat} .

2.1.4.2. The healed fracture toughness

For the mode I fracture toughness, the healed fracture toughness can be quantified as follows:

$$K_I^{\text{heal,max}} = K_I^{\text{virgin}} \times \frac{\sigma_{\infty}^{\text{heal}}}{\sigma_{\infty}^{\text{virgin}}} = K_I^{\text{virgin}} \times \frac{\sigma_{\text{cr}}^{\text{cohesive}}}{\sigma_{\text{ultimate}}^{\text{epoxy}}} \quad (2.8)$$

where $K_I^{\text{heal,max}}$, K_I^{virgin} , $\sigma_{\infty}^{\text{heal}}$, $\sigma_{\infty}^{\text{virgin}}$, $\sigma_{\text{cr}}^{\text{cohesive}}$, and $\sigma_{\text{ultimate}}^{\text{epoxy}}$ are the fracture toughness of healed/virgin states, far-field macroscopic stress of healed/virgin states, critical traction force of cohesive zone model between epoxy and healing agents, and ultimate stress of epoxy domain, respectively. Here, $\sigma_{\text{cr}}^{\text{cohesive}}$ and $\sigma_{\text{ultimate}}^{\text{epoxy}}$ are obtained from the molecular dynamics simulations.

2.2. Simulation Results and Discussions

2.2.1. Molecular dynamics simulation results of bulk healing agents

Through the molecular dynamics simulations, elastic properties, nonlinear stress-strain curves, and enthalpy of bulk healing agents are obtained. Before the prediction of these quantities, the density of bulk unit cells is compared to the experimental reference data. After the relaxation of bulk unit cell, the densities of bulk unit cells are obtained for different curing ratio, which shows 0.967 g/cm^3 at the high crosslinking ratio (94.3%). This shows similar to the experimental reference data (0.978 g/cm^3). Therefore, we predicted aforementioned quantities using these relaxed unit cells. Here, we conducted parametric studies on the crosslinking ratio of healing agents, whose definition is based on the number of crosslinking sites.

As shown in Fig. 2.4 (a), Young's moduli of bulk healing agents are clearly increased as the crosslinking ratio increases. It shows similar tendency to the other brittle network chemistries like epoxy. In spite of 61.8% crosslinking ratio of healing agents, it has small elastic modulus below 0.6GPa, which is just 25% of fully crosslinking system result. At high crosslinking ratio range (>75%), the elastic moduli of bulk healing agents are enhanced rapidly, which are attained near 2.0GPa at fully crosslinking ratio (>90%). These tendencies are also investigated at the nonlinear stress-strain curves as shown in Fig. 2.4 (b). At high crosslinking ratio, the bulk healing agents show high brittleness.

For the bulk healing agents, enthalpy analysis is carried out as shown in Fig. 2.5. Actually, the crosslinking reaction of healing agents is known as exothermic

reaction [55]. Therefore, it can be concluded that the molecular dynamic simulation results reflect exothermic reactions because the total enthalpies of healing agents are monotonically decreased as the crosslinking ratio of healing agents are increased. In the molecular dynamics simulation results, some fluctuations that stem from the model uncertainties of molecular dynamics simulations cause non-monotonically decreasing tendency for increasing crosslinking ratio of healing agents. For the one-to-one correspondence between crosslinking ratio and total enthalpies of bulk unit cells, the raw molecular dynamics simulation results are fitted by the simple cubic polynomial curves. The fitted curves show monotonically decreasing tendency for increasing crosslinking ratio of healing agents, which can be applied to the bridging two different definitions of the crosslinking ratio (enthalpy-based definition and the number of crosslinking sites-based definition) in the following subsection.

Although this dissertation does not focus on the treatment of model uncertainties of molecular dynamics simulations in the multiscale analysis, it should be emphasized that the model uncertainties of molecular dynamics simulations can generate the numerical noise in the prediction of mechanical property, thermal property, and other quantities. Regarding this, the statistical multiscale framework by consideration of model uncertainty of molecular dynamics simulations that stems from randomness of initial velocity was developed, which are described in Appendix A.

2.2.2. Predictive multiscale model of self-healing polymers

The homogenized elastic properties of self-healing polymers are obtained and compared with experimental data [60], as shown in Fig. 2.6 (a). Due to the weak stiffness of microcapsules including the uncrosslinked healing agents, the homogenized elastic properties of self-healing polymers are clearly decreased as the weight fraction of microcapsules increases. This micromechanics-based homogenization approach is employed to predict the homogenized elastic properties of self-healing polymer nanocomposites and self-healing epoxy/thermoplastic blends in the following sections (sections 3 and 4). Likewise, the virgin fracture toughness of self-healing polymers is also clearly decreased as shown in Fig. 2.6 (b). The decrease of virgin fracture toughness is experimentally acknowledged as the reduction of domain size of plastic deformations [61]. Using this experimental knowledge, the descriptive model of virgin fracture toughness is constructed as follows:

$$K_{lc}^{\text{virgin}} = K_{lc}^{\text{mat}} \times e^{-\beta^{\text{virgin}} \times f_{\text{capsule}}} \quad (2.9)$$

where f_{capsule} is volume fraction of microcapsule, and β^{virgin} is obtained as 10.7 from nonlinear least square fit method. This descriptive model is applied to the prediction of virgin fracture toughness of self-healing polymer nanocomposites and self-healing epoxy/thermoplastic blends in the sections 3 and 4.

For the purpose of the characterization of mode I fracture toughness for self-healing polymers at the healed states, the traction-separation curves between pDCPD networks and epoxy networks are quantified for different curing ratio of pDCPD networks using the molecular dynamics simulations. As shown in Fig. 2.7, there is clear contribution of curing ratio of pDCPD networks on the traction forces

of bilayer models. As mentioned before (section 2.2.1), the pDCPD networks of low curing ratio have low stiffness. Even though the non-bond interaction between pDCPD networks and epoxy networks are non-negligible as the adhesives, the pDCPD networks cannot play a role as a healing agent due to the low stiffness. On the other hands, the pDCPD networks can play a role as healing agents, with sufficiently high adhesive force and stiffness, at the high curing ratio ranges (>70%). From the molecular dynamics simulations, the ultimate stress of crosslinked epoxy networks is determined by 170 MPa, which is necessarily higher than experimental data due to high strain rate effects. The maximum traction force of epoxy/pDCPD bilayer model is 130 MPa, as shown in Fig. 2.7. From Eq. (2.8), the maximum healed fracture toughness is determined as $1.95 \text{ MPa}\cdot\text{m}^{1/2}$, and the predictive curve of healed fracture toughness is obtained as the following form:

$$K_{\text{Ic}}^{\text{heal}} = K_{\text{Ic}}^{\text{heal,max}} \times \left(1 - e^{-\beta^{\text{heal}} \times f_{\text{capsule}}} \right) \quad (2.10)$$

where β^{heal} is obtained as 7.55 from nonlinear least square fit method. The predictive curve is described in Fig. 2.6 (c).

2.2.3. Time response of healing behaviors of self-healing polymers

Using the enthalpy of bulk healing agents (described in Fig. 2.5), the relationship between enthalpy-based curing ratio and actual curing ratio is obtained as shown in Fig. 2.8 (a). The detail form can be described as follows:

$$\alpha_H = -0.75\alpha_N^2 + 1.75\alpha_N \quad (2.11)$$

where α_H and α_N are enthalpy-based curing ratio and actual curing ratio, respectively. As mentioned in section 2.1.2, the enthalpy-based curing kinetics of

DCPD was examined by Kessler *et al.* [55] for different concentrations of Grubbs' catalyst, which is ruthenium-based catalyst that shows high metathesis activity as shown in Fig. 2.8 (b). Using the Eq. (2.11) and the enthalpy-based curing kinetics, the actual curing ratio of healing agents can be obtained as shown in Fig. 2.8 (c). As shown in Fig. 2.7, the maximum traction force has rapid transition near the 52.5-77.5% curing ratio of healing agents. From the actual curing ratio-based kinetics (Fig. 2.8 (c)), it can be concluded that 5-12 hours are necessary to heal the macroscopic cracks at low concentration of catalyst. Meanwhile, at the medium and high concentrations of catalysts, 1.5-5.5 hours are necessary.

2.3. Chapter Summary and Conclusions

In this chapter, a multiscale model of self-healing polymers has been developed including the homogenized elastic properties, virgin fracture toughness, and healed fracture toughness using the micromechanics and the full atomistic molecular dynamics simulations. The maximum theoretical healing efficiency of self-healing polymers was predicted using the molecular dynamics simulations. The time response of mechanical behaviors of self-healing polymers has been characterized using the experiments-based curing kinetics model and the reactive mechanism of healing agents. In the following chapters, the multiscale analysis of self-healing polymer nanocomposites and self-healing epoxy/thermoplastic blends will be conducted using the established multiscale model of self-healing polymers herein.

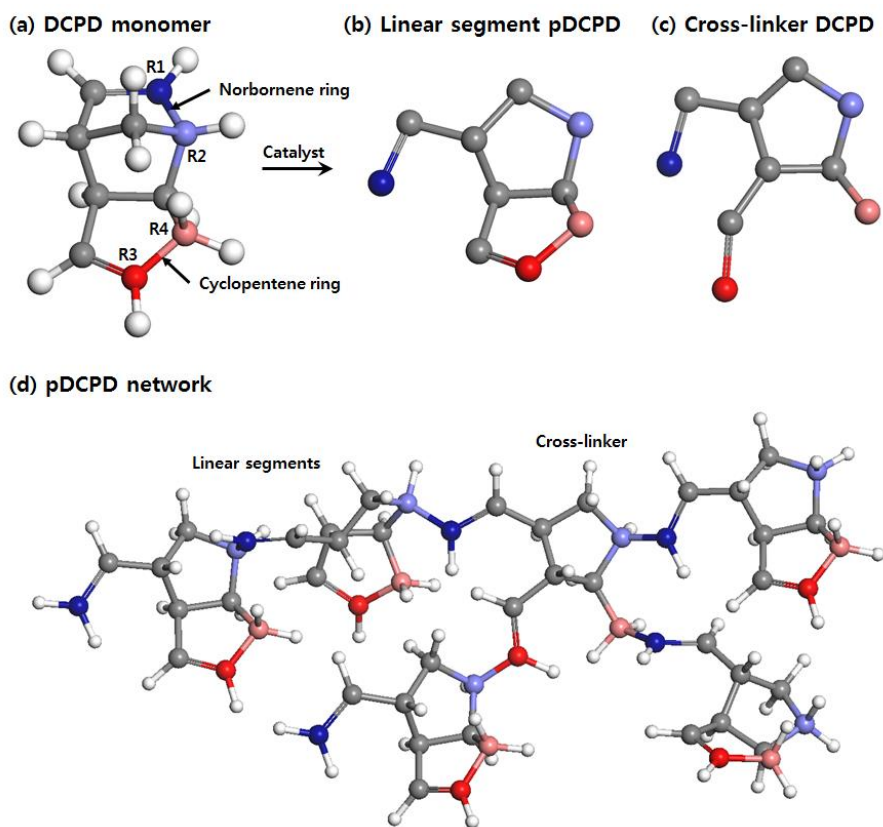
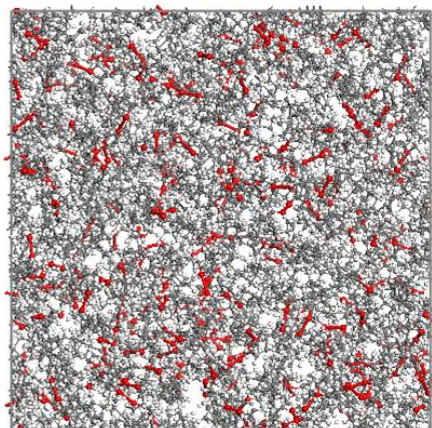


Fig. 2.1. Schematic of the reaction mechanism for ring-opening metathesis polymerization (ROMP) of dicyclopentadiene (DCPD) into a cross-linked polymer network: (a) DCPD monomer, (b) DCPD monomer that has experienced the opening of norbornene ring, which play a role as linear segment, (c) DCPD monomer that has experienced both the opening of norbornene ring and cyclopentene ring, which play a role as cross-linker, and (d) polymer networks of pDCPD. (Here, (b) and (c) exclude configuration of hydrogen bonds)

(a) Crosslinking ratio: 26%



(b) Crosslinking ratio: 96%

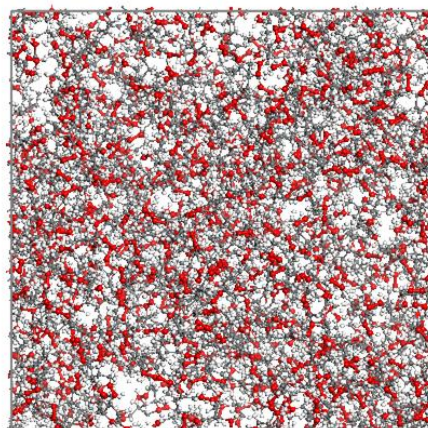


Fig. 2.2. Unit cell configuration of crosslinked DCPD networks: (a) 26% crosslinking ratio, and (b) 96% crosslinking ratio. (crosslinked sites are highlighted by red colors)

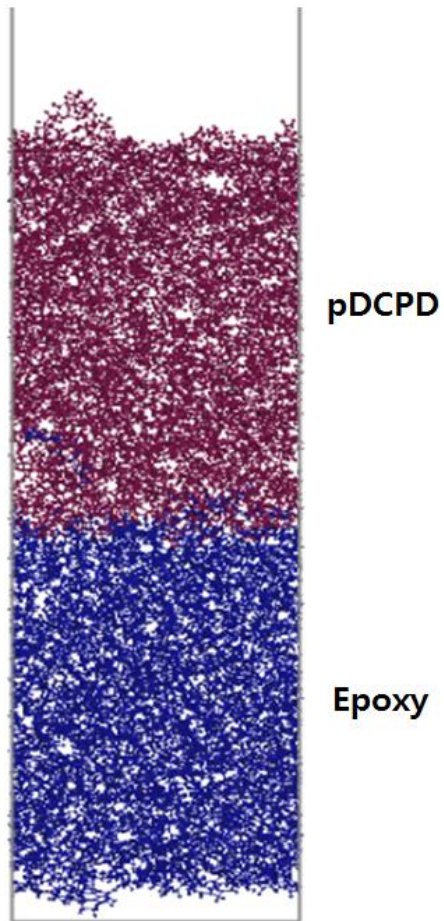


Fig. 2.3. Bilayer unit cell models for characterization of cohesive zone model between polycyclopentadiene (pDCPD) networks and epoxy networks.

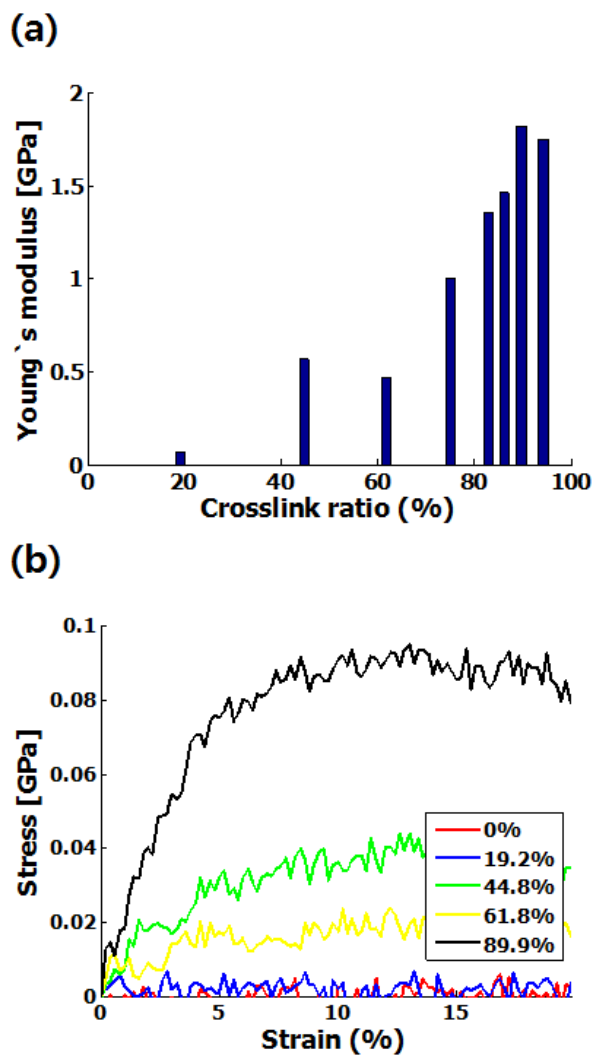


Fig. 2.4. Molecular dynamics simulation results on mechanical behaviors of bulk healing agents: (a) Young's moduli, and (b) nonlinear stress-strain curves

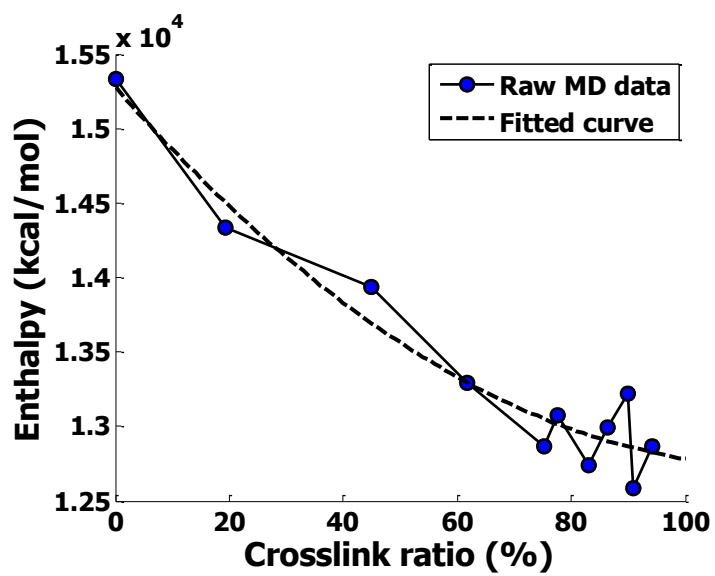


Fig. 2.5. Molecular dynamics simulation results on enthalpy of bulk healing agents

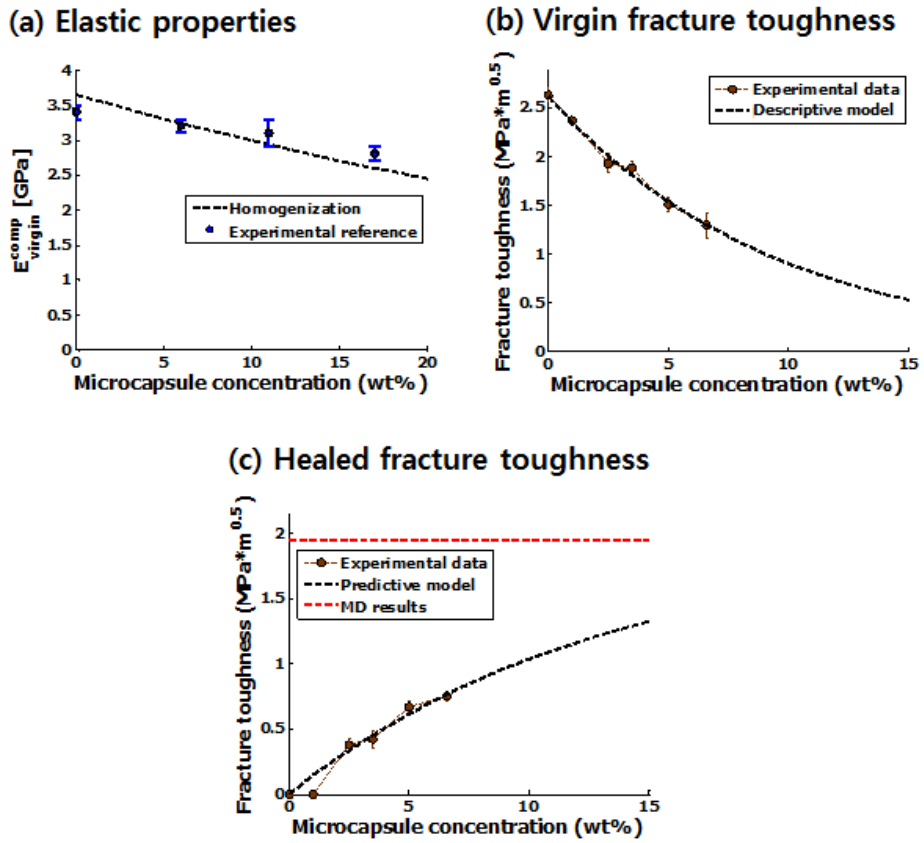


Fig. 2.6. Effective mechanical properties of self-healing polymers: (a) homogenized elastic properties and experimental validation, (b) descriptive model of virgin fracture toughness, and (c) predictive model of healed fracture toughness

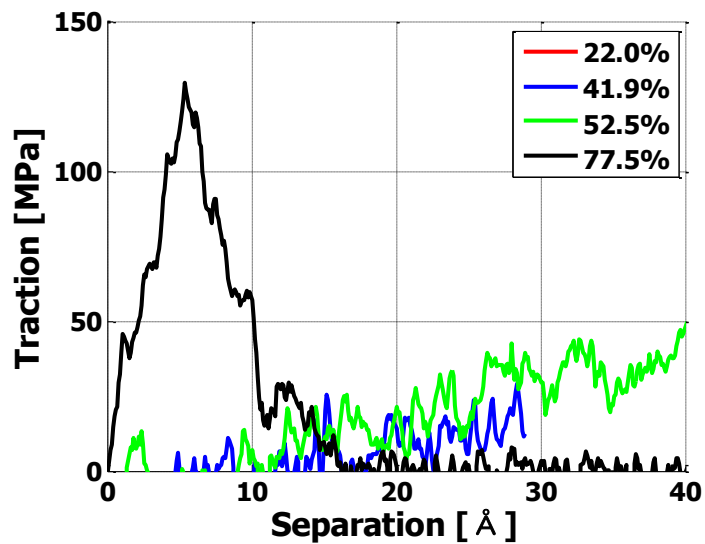


Fig. 2.7. Mode I traction-separation behaviors of bilayer model between polydicyclopentadiene (pDCPD) networks and epoxy networks

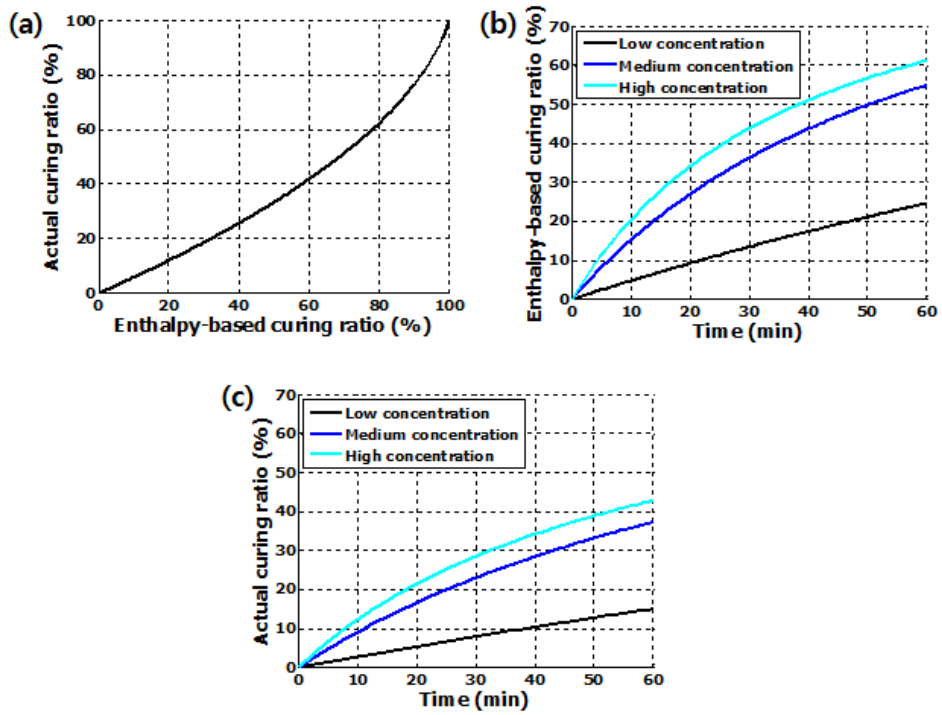


Fig. 2.8. Curing kinetics model: (a) the relationship between enthalpy-based curing ratio and actual curing ratio, (b) time response of enthalpy-based curing ratio, and (c) time response of actual curing ratio

3. MULTISCALE ANALYSIS OF SELF-HEALING POLYMER NANOCOMPOSITES

In this chapter, a multiscale mechanical analysis framework of self-healing polymer nanocomposites is developed. The mechanics of self-healing polymer nanocomposites includes the healing behavior of macroscopic crack and the reinforcing and toughening behaviors that come from the rigid nanoparticles. Firstly, a multiscale model to predict fatigue crack propagation behavior of polymeric nanocomposites is proposed. The major novelty of this work is that the enhancement of strain energy release rate due to major toughening mechanisms, which are experimentally observed, is considered for the prediction of fatigue crack propagation behavior of polymeric nanocomposites using the multiscale approach. The merit of this approach is that this proposed model is just necessary for the experimental data of neat matrix about fatigue crack growth. The prediction by the proposed multiscale model provides a satisfactory agreement for experimental data at low weight fraction range of nanoparticles. Finally, by extension of the proposed multiscale model to the self-healing polymer nanocomposites, the multiscale analysis of self-healing polymer nanocomposites is conducted with providing the master curves of mechanical properties and fatigue crack growth behaviors for various concentrations of nanoparticles and microcapsules including healing agents.

3.1. Multiscale Model to Predict Fatigue Crack Growth of Thermoset Polymer Nanocomposites

3.1.1. Description of the multiscale-multimechanism strategy

Fracture toughness and fatigue crack propagation behavior are critically related to the strain energy release rate that is the dissipated energy per unit of newly created fracture surface area. A multiscale-multimechanism approach to quantify the strain energy release rate of thermoset polymer nanocomposites is employed to predict fracture toughness and fatigue crack propagation behaviors. The experimental observations showed that the embedded nanoparticles played three key roles in microscopic energy dissipation mechanisms of “nanoparticulate debonding”, “the subsequent plastic yield of nanovoids” [22,23,26], and “localized shear banding” [27]. For the mode I crack separation behavior, the strain energy release rate of thermoset polymer nanocomposites, G_1^{comp} , can be written as the following simple summation form:

$$G_1^{\text{comp}} = G_1^{\text{mat}} + \sum_i \Delta G_i \quad (3.1)$$

where G_1^{mat} and ΔG_i are the strain energy release rate of unmodified matrix and the enhancement due to the i th damage mechanisms ($i=1$: particle debonding, $i=2$: plastic yielding of nanovoids, and $i=3$: localized shear band). By taking J -integral near the crack tip, ΔG_i can be obtained as follows [28,29]:

$$\Delta G_i = 2 \times \int_0^{\rho^* (\phi=\pi/2)} u_i d\rho \quad (3.2)$$

where u_i is the microscopic dissipation energy produced by i th damage mechanisms in the representative volume element that is entirely typical of the whole mixture on average.

A multiscale strategy to calculate the dissipated energy by considering the damage mechanism on the microscale near the crack tip of macroscopic structures has been developed [26-28]. The multiscale analysis includes the combined continuum analysis of macroscale (length scale of specimen) and microscale (length scale of nanoparticle). The link between the macroscopic quantities and the microscopic quantities is made by considering the volume average of microscopic quantities defined in the representative volume elements:

$$\{\Sigma, \mathbf{E}\} = \frac{1}{|Y|} \int_Y \{\boldsymbol{\sigma}, \boldsymbol{\varepsilon}\} dV \quad (3.3)$$

where $\{\Sigma, \mathbf{E}\}$ and $\{\boldsymbol{\sigma}, \boldsymbol{\varepsilon}\}$ are the macroscopic and microscopic stress/strain fields, respectively, and Y is domain of the representative volume elements. Through the theory of linear fracture mechanics under the assumption of plane strain conditions, hydrostatic and von Mises macroscopic stress fields are described as follows:

$$\Sigma_h = \frac{\Sigma_{xx} + \Sigma_{yy} + \Sigma_{zz}}{3} = \frac{2(1 + \nu_{\text{comp}})K_I}{3\sqrt{2\pi\rho}} \cos \frac{\phi}{2} \quad (3.4)$$

$$\Sigma_{\text{vM}} = \frac{K_I}{\sqrt{4\pi\rho}} \cos \frac{\phi}{2} \sqrt{2(1 - 2\nu_{\text{comp}})^2 + 3(1 - \cos \phi)} \quad (3.5)$$

where K_I and ν_{comp} are the stress intensity factor of the macroscopic stress field and the Poisson's ratio of the composites, respectively. Using the micromechanics approach, the dissipated energy of representative volume elements due to damage mechanisms can be obtained as a function of ρ . By computing the J -integral (Eq. (3.2)), the strain energy release rate enhancement of thermoset polymer nanocomposites can be quantified. In the following sections, the analytic solutions of the dissipated energy will be briefly reviewed for each mechanism.

3.1.2. Quantification of additive strain energy release rate due to toughening mechanisms

3.1.2.1. Nanoparticulate debonding-induced plastic yield of nanovoids

The energy dissipating mechanism due to nanoparticulate debonding-induced plastic yield of nanovoids includes “nanoparticulate debonding” and “the subsequent plastic yield of nanovoids”. With an assumption that interface between nanoparticle and matrix is debonded uniformly, the enhancement in strain energy release rate due to this mechanism can be quantified as the analytic form. The microscopic strain energy density dissipated by the interfacial debonding can be calculated as the following form:

$$u_{db} = 3 \times \frac{\gamma_{db}}{r_p} \times f_p \quad (3.6)$$

where γ_{db} , r_p , and f_p are interfacial fracture toughness of nanoparticle, radius and volume fraction of nanoparticles, respectively. The enhancement of the strain energy release due to interfacial debonding mechanism can be estimated by the following form:

$$\Delta G_{db} = f_p \times \psi_{db} \times G_I^{comp} \quad (3.7)$$

where ψ_{db} is a contribution of interfacial debonding mechanism per unit volume fraction of nanoparticles on the strain energy release rate enhancement [26]:

$$\psi_{db} = \frac{2}{3\pi} \times \frac{\gamma_{db}}{r_p} \times \frac{1 + \nu_{comp}}{1 - \nu_{comp}} \times \frac{E_{comp}}{\sigma_{cr}^2 \times C_h^2} \quad (3.8)$$

where E_{comp} and ν_{comp} are Young’s modulus and Poisson’s ratio of nanocomposites, respectively, σ_{cr} is the critical debonding stress of the interface [62]:

$$\sigma_{cr} = \sqrt{\frac{4\gamma_{db}}{r_p} \times \frac{E_{mat}}{1+\nu_{mat}}} \quad (3.9)$$

and C_h is the reciprocal of the hydrostatic part of the global stress concentration tensor [63]:

$$C_h = \frac{K_{mat}}{K_{par}} \times \frac{3K_{par} + 4G_{mat}}{3K_{mat} + 4G_{mat}} \quad (3.10)$$

The debonded nanoparticles cannot play a role as the reinforcements. It was reported that the debonded nanoparticles could be regarded as the nanovoids that has the same diameter of the initial nanoparticles [26]. The high stress fields in the vicinity of the nanovoids cause local yielding of the nanovoids, which dissipates the energy plastically and enhances the strain energy release rate of polymer nanocomposites. The enhancement of the strain energy release due to plastic yielding of nanovoids can be described as the following forms:

$$\Delta G_{py} = f_p \times \psi_{py} \times G_I^{comp} \quad (3.11)$$

where ψ_{py} is a contribution of plastic yielding of nanovoids mechanism per unit volume fraction of nanoparticles on the enhancement of the strain energy release [26]:

$$\psi_{py} = \frac{4}{9\pi C_h} \times \frac{E_{comp}}{E_{mat}} \times \frac{(1+\nu_{comp})(1+\nu_{mat})}{1-\nu_{comp}} \times \frac{\sigma_{Ym}}{\sigma_{cr}} \times e^{\left(3C_h \times \frac{\sigma_{cr}}{\sigma_{Ym}} - 1\right)} \quad (3.12)$$

for an elastic-perfectly plastic behavior of the matrix, where σ_{Ym} is the yield stress of matrix.

3.1.2.2. Localized shear banding

The microscopic stress concentrations around nanoparticles promote the formation of localized plastic shear banding between nanoparticles, which causes highly dissipated plastic energy. With an assumption that interparticulate distances are uniform, the enhancement of the strain energy release due to this mechanism can be quantified as the analytic form. Using a multiscale analysis framework, the enhancement of the strain energy release due to localized shear banding can be described as the following forms:

$$\Delta G_{sb} = f_p \times \psi_{sb} \times G_I^{\text{comp}} \quad (3.13)$$

where ψ_{sb} is a contribution of localized shear banding mechanism per unit volume fraction of nanoparticles on the enhancement of strain energy release rate [27]:

$$\psi_{sb} = \frac{I_{sb}}{4\pi\sigma_{ycm}^2 (1 - \mu/\sqrt{3})^2} \times \frac{E_{\text{comp}}}{1 - \nu_{\text{comp}}^2} \times \Gamma \quad (3.14)$$

where μ is a non-dimensional pressure coefficient, σ_{ycm} is the compressive yield stress of matrix, Γ is a function to quantify the production of microscopic energy, I_{sb} is for the stress concentration near the nanoparticles:

$$\Gamma = \sigma_{ym} \gamma_{fm} \left\{ \left(\frac{\pi}{6f_p} \right)^{\frac{1}{3}} - \frac{52}{63} \right\} \quad (3.15)$$

$$I_{sb} = \frac{1}{2\pi} \times (pH_{vm}^2 + k\mu H_{vm} H_h + j\mu H_h^2) \quad (3.16)$$

where σ_{ym} is the shear yield stress of matrix, γ_{fm} is the shear fracture strain, and parameters (p, k, j) are function of Poisson's ratio. Here, the parameters (p, k, j) are determined by the listed data in Ref. 27.

3.1.3. The prediction of overall strain energy release rate of the thermoset polymer nanocomposites

The overall strain energy release rate of thermoset polymer nanocomposites can be written as the following form:

$$G_I^{\text{comp}} = \frac{G_I^{\text{mat}}}{1 - f_p (\psi_{\text{db}} + \psi_{\text{py}} + \psi_{\text{sb}})} \quad (3.17)$$

This relationship of the strain energy release rate between nanocomposites and neat matrix can be applied to the estimation of the fracture toughness and fatigue crack propagation behavior.

3.1.4. The overall fracture toughness of thermoset polymer nanocomposites

From Eq. (3.17), the critical strain energy release rate of thermoset polymer nanocomposites can be determined as the following form:

$$G_{\text{Ic}}^{\text{comp}} = \frac{G_{\text{Ic}}^{\text{mat}}}{1 - f_p (\psi_{\text{db}} + \psi_{\text{py}} + \psi_{\text{sb}})} \quad (3.18)$$

Through the strain energy release rate failure criterion, the mode I fracture toughness, which is same with the critical mode I stress intensity factor, is related to the critical strain energy release rate as the following form:

$$K_{\text{Ic}}^{\text{comp}} = K_{\text{Ic}}^{\text{mat}} \times \zeta \quad (3.19)$$

where ζ is defined as the following form:

$$\zeta = \sqrt{\frac{1}{1 - f_p (\psi_{\text{db}} + \psi_{\text{py}} + \psi_{\text{sb}})} \times \frac{E_{\text{comp}}}{1 - \nu_{\text{comp}}^2} \times \frac{1 - \nu_{\text{mat}}^2}{E_{\text{mat}}}} \quad (3.20)$$

3.1.5. *The prediction of overall fatigue crack propagation behaviors of thermoset polymer nanocomposites*

3.1.5.1. without consideration of crack closure effect

The fatigue crack propagation behaviors of neat matrix and nanocomposites can be described as the following forms:

$$\frac{da_{\text{mat}}}{dN} = f_{\text{mat}}(\Delta K_{\text{I}}^{\text{mat}}), \quad \frac{da_{\text{comp}}}{dN} = f_{\text{comp}}(\Delta K_{\text{I}}^{\text{comp}}) \quad (3.21)$$

For the same crack length extension of specimen per unit cycle, the necessary range of stress intensity factors can be described as follows:

$$\Delta K_{\text{I}}^{\text{mat}} = f_{\text{mat}}^{-1}\left(\frac{da}{dN}\right), \quad \Delta K_{\text{I}}^{\text{comp}} = f_{\text{comp}}^{-1}\left(\frac{da}{dN}\right) \quad (3.22)$$

From the relationship between stress intensity factor and strain energy release rate, the stress intensity factors of thermoset polymer nanocomposites can be described as follows because the microscopic energy dissipating mechanisms are identical in all three fatigue crack propagation regimes:

$$\left(K_{\text{I,max}}^{\text{comp}}, K_{\text{I,min}}^{\text{comp}}, \Delta K_{\text{I}}^{\text{comp}}\right) = \left(K_{\text{I,max}}^{\text{mat}}, K_{\text{I,min}}^{\text{mat}}, \Delta K_{\text{I}}^{\text{mat}}\right) \times \zeta \quad (3.23)$$

By substituting Eq. (3.23) into Eq. (3.22), the relationship of fatigue crack propagation behavior between neat matrix and nanocomposites can be described as follows:

$$f_{\text{comp}}^{-1} = f_{\text{mat}}^{-1} \times \zeta \quad (3.24)$$

Paris law of the nanocomposites, which is famous calibration model of the linear interval around the center, can be described as follows:

$$\begin{aligned}\frac{da}{dN} &= C_{\text{mat}} \times (\Delta K_{\text{I}}^{\text{mat}})^{m_{\text{mat}}} \\ &= C_{\text{mat}} \times \left(\frac{1}{\zeta} \times \Delta K_{\text{I}}^{\text{comp}} \right)^{m_{\text{mat}}} = C_{\text{comp}} \times (\Delta K_{\text{I}}^{\text{comp}})^{m_{\text{comp}}}\end{aligned}\quad (3.25)$$

where the coefficients of the Paris law can be obtained as follows:

$$C_{\text{comp}} = C_{\text{mat}} \times \zeta^{-m_{\text{mat}}}, \quad m_{\text{comp}} = m_{\text{mat}} \quad (3.26)$$

3.1.5.2. with consideration of crack closure effect

Fatigue crack propagation is mutual competition between intrinsic mechanism of damage/crack advance and extrinsic mechanism of crack tip shielding involved in crack growth. The fatigue crack propagation behaviors and the domain size of fatigue process zone [64] are determined by the following effective range of stress intensity factors [65]:

$$\Delta K_{\text{I,eff}} = \begin{cases} K_{\text{I,max}} - K_{\text{I,cl}} & (K_{\text{I,min}} \leq K_{\text{I,cl}}) \\ K_{\text{I,max}} - K_{\text{I,min}} & (K_{\text{I,cl}} \leq K_{\text{I,min}}) \end{cases} \quad (3.27)$$

where $K_{\text{I,cl}}$ is the mode I stress intensity factor to close the crack. The relationship of the effective range of stress intensity factors between nanocomposites and neat matrix can be described as the following forms:

$$\Delta K_{\text{I,eff}}^{\text{comp}} = \Delta K_{\text{I,eff}}^{\text{mat}} \times \zeta \quad (3.28)$$

Therefore, the fatigue crack propagation behavior of thermoset polymer nanocomposites can be described as the following form:

$$f_{\text{comp}}^{-1} \left(\frac{da}{dN} \right) = \zeta \times f_{\text{mat}}^{-1} \left(\frac{da}{dN} \right) + (K_{\text{I,cl}}^{\text{comp}} - K_{\text{I,cl}}^{\text{mat}} \times \zeta) \times (1 - R) \quad (3.29)$$

where the minimum-to-maximum load ratio R is defined as $K_{\text{min}}/K_{\text{max}}$.

3.1.6. Model validation by comparison with experimental data

3.1.6.1. System details for model validation

For the purpose of model validation, the theoretically estimated fatigue crack growth of the epoxy/silica nanocomposites are compared to the experimental reference data [11]. Sinusoidal loads were applied and the minimum-to-maximum load ratio R was set to 0.1 with a frequency of 10 Hz and constant ΔK_I . The diameter of silica nanoparticles is set as 20nm, which is same with that of reference systems [11]. The summary of the system details of the experimental data are listed in Table 3.1. With symmetric yielding assumption, the non-dimensional pressure coefficient, μ , is set as zero. The length of specimen and initial pre-crack are assumed as 80mm and 20mm, respectively.

3.1.6.2. Experimental validation without crack closure effect

Before the model validation of fatigue crack growth, we compared the basic mechanical properties (elastic properties, critical strain energy release rate, and critical stress intensity factor) to the experimental reference data [11]. As shown in Fig. 3.1, the theoretically estimated basic effective mechanical properties are well matched to the experimental reference data. Despite the negligence of the additional interphase zone and simplified representative volume elements, the multiscale model provides highly satisfactory predictions. The decreasing slope including plateau in high weight fraction range is commonly understood due to the influence of filler agglomeration [28]. The related works are on-going research including the percolated interphase zone and the clustered nanoparticles (Appendix

B).

Finally, the predicted fatigue crack propagation behaviors of epoxy/silica nanocomposites using the proposed multiscale model are compared with experimental reference data [11]. The results show satisfactory predictions, as shown in Figs. 3.2 (a) and (b). As shown in Fig. 3.3, the addition of rigid nanoparticles has clear contribution on the extension of fatigue life. Despite the reliable prediction of fatigue crack propagation behaviors of epoxy/silica nanocomposites at low weight fraction range (<12%), the prediction in the high weight fraction range is unfortunately way off. The origin of this limitation is expected due to the filler agglomeration that is same with the case of fracture toughness, and the related works are on-going research including the percolated interphase zone [66] and the clustered nanoparticles. Meanwhile, it is worth mentioning that the major contribution of this work is that master curves of thermoset polymeric nanocomposites can be predicted for various weight fractions of nanoparticles when the fatigue crack growth behavior of neat thermoset polymer matrix is predetermined. In Fig. 3.2 (a), we employed the experimental data of fatigue crack growth behavior of neat epoxy matrix as base curve for generation of master curves.

3.1.6.3. Influences of crack closure effects

Unfortunately, there are very few studies on the fatigue crack closures of the thermoset polymers and polymer-based composite materials due to their intrinsic brittleness [67]. Even though this class of materials experiences only the small amount of plasticity-induced crack closure effects unlike the ductile metallic

composites ($K_{I,cl} \sim 0.4-0.8K_{Ic}$) [68], an influence of crack closure mechanisms on the fatigue crack growth behaviors should be investigated because the domain size of fatigue process zone involving the microscopic energy dissipating mechanisms is highly sensitive to the crack closure stress intensity factors despite the small amount. Furthermore, the achievement of fatigue life-extended materials [69,70] using the artificial infiltration of a viscous fluid or a solid wedge in the wake of the crack motivates the understanding of influences of the crack closure phenomena. The precise quantification of actual crack closure stress intensity factor is not the scope of this study, and we conducted parametric studies on the crack closure stress intensity factor (in the range of $K_{I,cl} \sim 0.0-0.5K_{Ic}$) that is independent on the weight fraction of nanoparticles.

Without crack closure effects, fatigue crack propagation behaviors of thermoset polymer nanocomposites are simply shifted along with horizontal axes of a log-log plot as weight fraction of nanoparticles increases as shown in Fig. 3.2 (a). When we consider the crack closure effects, the slope (m_{comp}) in the Paris regime is clearly reduced by the addition of nanoparticles, as shown in Figs. 3.2 (c)-(f) and Fig. 3.4 (a). The decreasing slope in the Paris regime has been observed in the recently reported experimental studies [10,11]. In spite of the negligibly small amount of crack closure ($K_{I,cl} \sim 0.1K_{Ic}$), the decreasing slope in the Paris regime is clearly observed as shown in Fig. 3.4 (a) of $K_{I,cl} = 0.05\text{MPa}\cdot\text{m}^{1/2}$. Due to the lack of the studies on the crack closure effects of thermoset polymer nanocomposites, there is no clear experimental evidence. However, it is seemingly that the recently reported decreasing slope in the Paris regime [10,11] could be related to crack closure effects. The stress intensity factor leading to instable crack growth (ΔK_{cf}) and the

threshold of the fatigue crack growth (ΔK_{th}) are also listed and compared with experimental data, as shown in Figs. 3.4 (b) and (c). Meanwhile, the proposed multiscale model can be applied to the weight fraction-dependent crack closure effects, and the slope in Paris regime will be decreased at $K_{I,cl}^{comp} < K_{I,cl}^{mat} \times \zeta$, and increased at $K_{I,cl}^{comp} > K_{I,cl}^{mat} \times \zeta$, from Eq. (3.29).

3.2. Multiscale Analysis of Self-Healing Polymer Nanocomposites

In this chapter, multiscale analysis for the self-healing polymer nanocomposites is conducted. For the prediction of elastic properties of self-healing polymer nanocomposites, multi-inclusion models are used. The details are described in the section 2.1.4.1. To predict the virgin fracture toughness of self-healing polymer nanocomposites, the mechanism-based multiscale approach is used. As mentioned in previous section, the total area of active process zone is reduced due to the embedded microcapsules. Therefore, the microscopic energy dissipation is also reduced in proportion to the reduced area of active process zone as follows:

$$K_{Ic}^{virgin,comp} = K_{Ic}^{comp} \times e^{-\beta^{virgin} \times f_{capsule}} \quad (3.30)$$

Here, β^{virgin} is determined same as previous chapter (Eq. 2.9). Finally, with the consideration of weak interfacial adhesion, the healed fracture toughness of self-healing polymer nanocomposites can be obtained as follows:

$$K_{Ic}^{healed,comp} = K_{Ic}^{comp} \times \frac{\sigma_{cr}^{cohesive}}{\sigma_{ultimate}} \quad (3.31)$$

Using these multiscale descriptions for the prediction of elastic properties, virgin fracture toughness, and healed fracture toughness of self-healing polymer nanocomposites, the predicted results are described in Fig. 3.6. For various weight

fractions of microcapsules and nanoparticles, the master curves of self-healing polymer nanocomposites are constructed.

3.3. Chapter Summary and Conclusions

In this chapter, the multiscale analysis of self-healing polymer nanocomposites is conducted. Before the multiscale analysis, the multiscale models to predict elastic properties, fracture toughness and fatigue crack growth behaviors of thermoset polymer nanocomposites are firstly developed. The proposed models show highly satisfactory agreement with experimental data. This is the first attempt to predict fatigue crack growth behaviors of thermoset polymer nanocomposites using the microscopic energy dissipating mechanisms (nanoparticulate debonding-induced plastic yield of nanovoids, and localized shear banding). We believe that the proposed multiscale model can act as the guideline of the characterization of master curves of fatigue crack growth behaviors for various weight fraction systems and the foundation of the fatigue design of the thermoset polymer nanocomposites with design of microscopic energy dissipating mechanisms. In future development, it is expected that the actual crack closure stress intensity factors can be predicted, even though it is still challenging issue [71,72]. This study can be extended to the autonomous healing systems [4,5,68] and biomimetic structures [73,74]. Using the microscopic dissipating energy mechanisms, intrinsic toughening mechanism, and macroscopic crack shielding effects, the useful multiscale models have been developed. It is expected that this multiscale model can provide useful guidelines for the design of self-healing polymer nanocomposites.

Table 3.1. Material properties of polymer nanocomposites used in the present analysis

Material properties	γ_{db} [J/m ²]	Matrix					Particle	
		E [GPa]	ν	σ_{Ym} [MPa]	G_{Im^2} [J/m ²]	γ_{fm}	E [GPa]	ν
Values	0.04	2.9	0.4	120	66	0.06	104	0.3

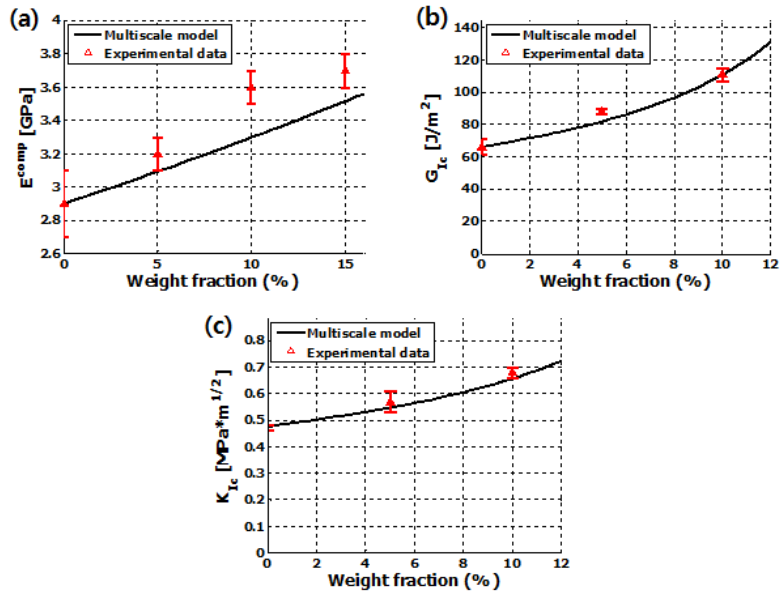


Fig. 3.1. Predicted mechanical properties of polymer nanocomposites and experimental validations: (a) elastic properties, (b) critical stress intensity factors, and (c) critical strain energy release rate. The details of experimental data can be found in Ref. 11.

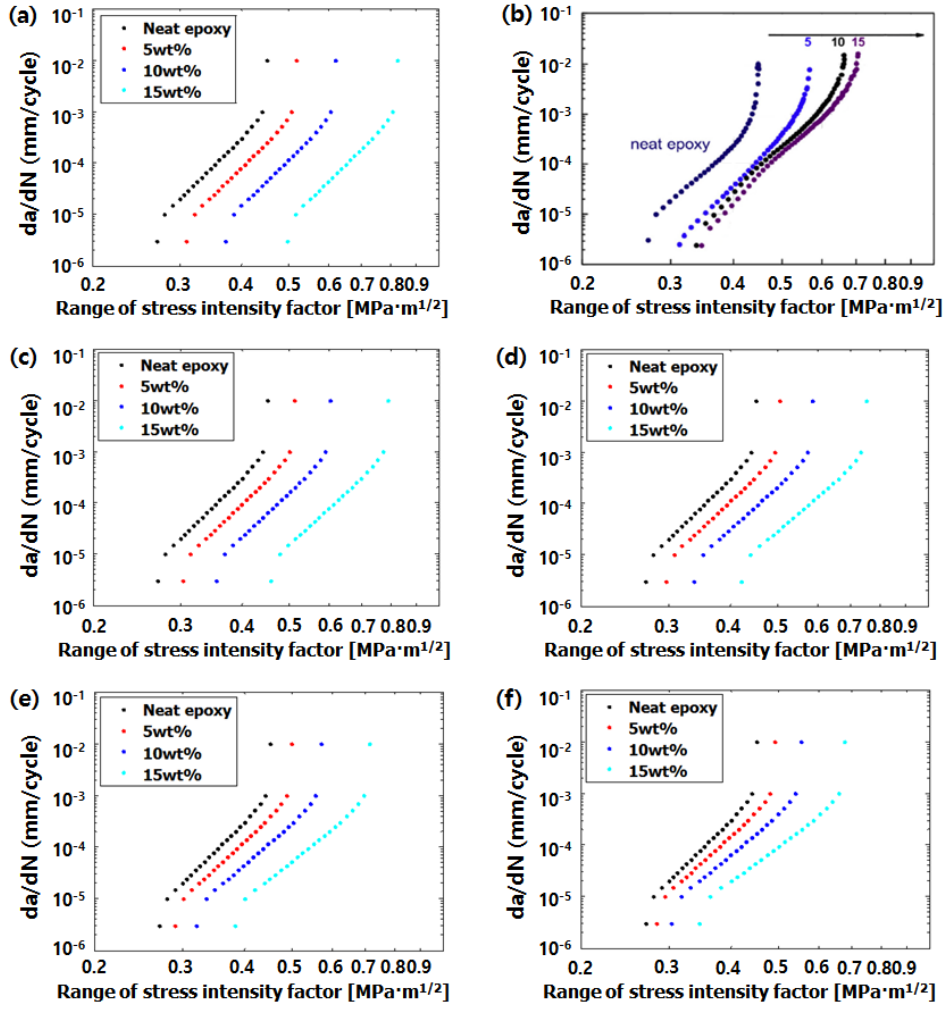


Fig. 3.2. Fatigue crack growth behaviors of polymer nanocomposites: (a) predicted results using the proposed method without crack closure effect, (b) experimental results [11], predicted results with crack closure effects of (c) $K_{I,cl}=0.05 \text{ MPa}\cdot\text{m}^{1/2}$, (d) $K_{I,cl}=0.10 \text{ MPa}\cdot\text{m}^{1/2}$, (e) $K_{I,cl}=0.15 \text{ MPa}\cdot\text{m}^{1/2}$, (f) $K_{I,cl}=0.20 \text{ MPa}\cdot\text{m}^{1/2}$.

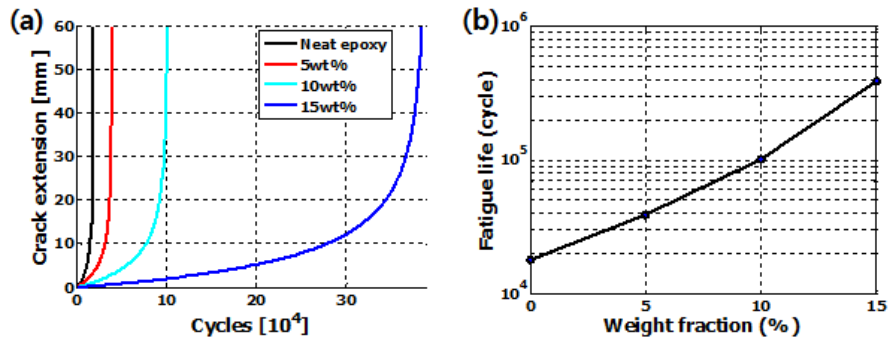


Fig. 3.3. Fatigue crack propagation behaviors of polymer nanocomposites: (a) crack extension-the number of load cycles curve, and (b) fatigue life (at $K_{I,cl}=0.20 \text{ MPa} \cdot \text{m}^{1/2}$)

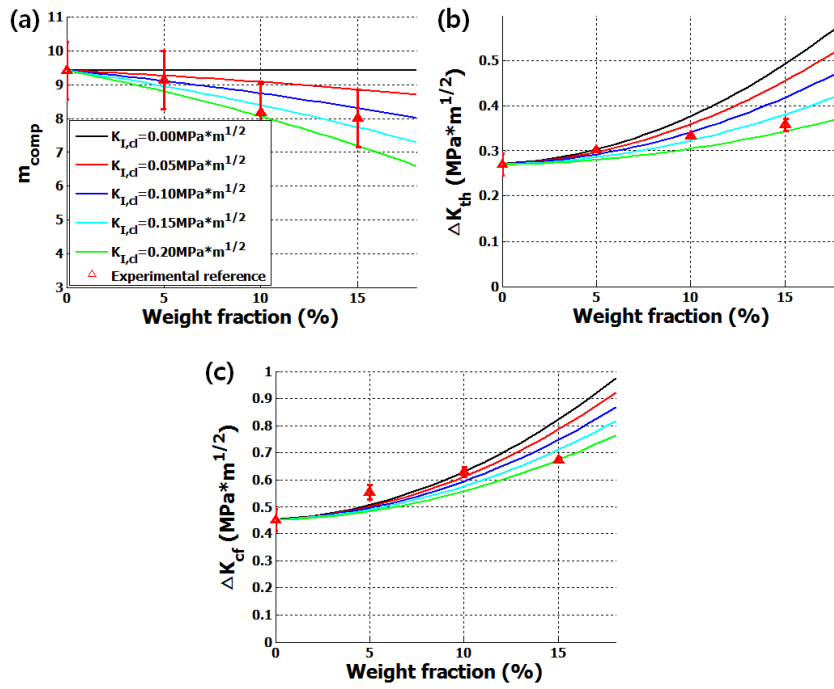
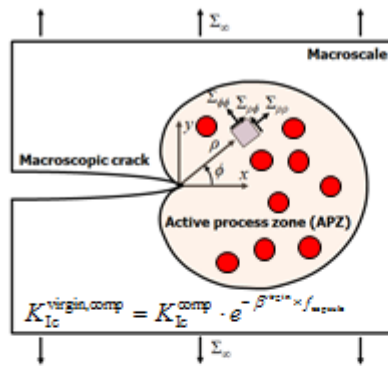


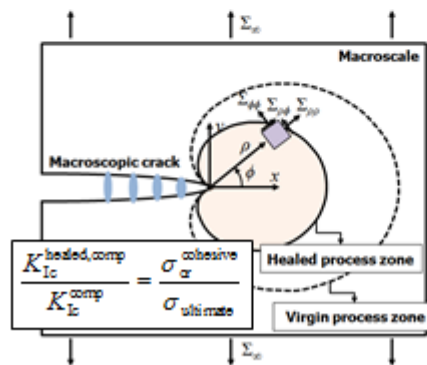
Fig. 3.4. An influence of crack closure effects on the (a) m_{comp} , (b) ΔK_{th} , and (c) ΔK_{th} as a function of nanoparticulate contents and comparison with experimental data [11].

(a) Virgin toughness



➤ Consideration of reduced damage zone

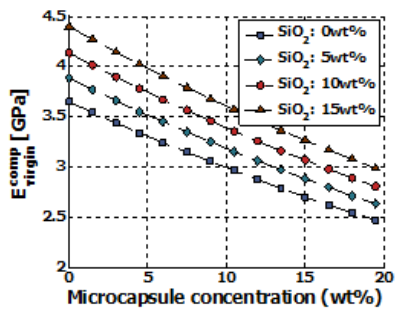
(b) Healed toughness



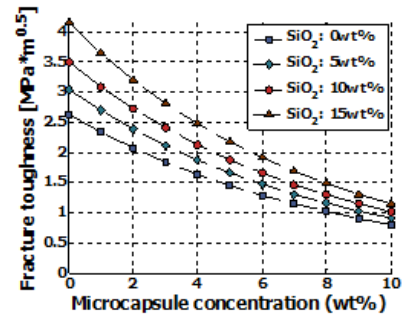
➤ Consideration of weak interfacial adhesion

Fig. 3.5. Schematics of self-healing polymer nanocomposites: (a) virgin toughness, and (b) healed toughness

(a) Elastic properties



(b) Virgin fracture toughness



(c) Healed fracture toughness

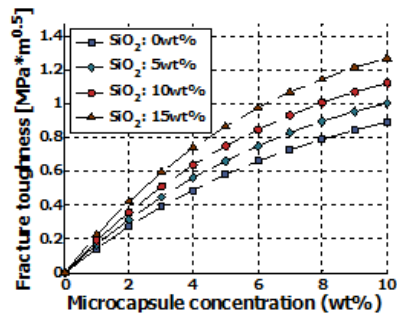


Fig 3.6. Basic mechanical properties of self-healing polymer nanocomposites: (a) elastic properties, (b) virgin fracture toughness, and (c) healed fracture toughness

4. MULTISCALE ANALYSIS OF SELF-HEALING EPOXY/THERMOPLASTIC BLENDS

In this chapter, a multiscale mechanical analysis framework of self-healing epoxy/thermoplastic blends is developed. To achieve this objective, a multiscale model to predict fracture toughness of epoxy/thermoplastic blends is developed and validated with experimental data. By extension of the proposed multiscale model, elastic properties and fracture toughness of self-healing epoxy/thermoplastic blends are obtained with the purpose of multiscale analysis.

4.1. Multiscale Model of Epoxy/Thermoplastic Blends and Experimental Validations

4.1.1. Motivations

Based on the experimental observations, it was reported that the ductile thermoplastic particle plays two key roles in toughening mechanism of thermoplastic/epoxy blends plastic deformation in the material near the macroscopic crack tip, and particle bridging in the crack wake [45,46], as shown in Fig. 1.3. For the first mechanism, multiscale approach [26-28] is useful when developing an analytical model with an infinite number of particles embedded in the matrix domain. The density of energy dissipated by the damage mechanism of the representative volume elements near the macroscopic crack tip can be described by micromechanics models as shown in Fig. 1.4. The fracture toughness enhancement of the composites can be obtained quantitatively through the J -

integral near the macroscopic crack tip [29]. However, multiscale models for the toughness enhancements of thermoplastic/epoxy blends have not been reported, unlike rigid nanoparticles [26,27]. For this reason, we focused on the development of a model to describe the fracture toughness improvement by thermoplastic particle yield near the crack tip. The main objective of the present paper is to quantify the toughness enhancement due to the plastic yield of the thermoplastic particle.

With this motivation, we conducted the formulation to quantify the plastic dissipation energy of thermoplastic particles near the macroscopic crack tip. To quantify the plastic dissipation energy of thermoplastic particles, molecular dynamics simulation was then conducted to obtain the curve of nonlinear hydrostatic stress versus volumetric strain. The proposed multiscale model is validated through the reported experimental data. Based on results obtained using the multiscale model, design guidelines regarding the proper selection of toughening agents are proposed for enhancing the fracture toughness of thermoplastic/epoxy blends.

4.1.2. Thermoplastic particle yield-induced toughness enhancement

4.1.2.1. Description of the plastic energy from thermoplastic particles

It is assumed that the thermoplastic particles are well separated from the epoxy domain as a continuous and homogeneous phase, as shown in the scanning electron microscope image in Fig. 1.3 [41]. The embedded thermoplastic phase is assumed to be spherical in shape. The calculation ignores the presence of microcracks [40] (in the particles, in the matrix, and at the interface) during the plastic deformation

and fracture of the thermoplastic particles. Therefore, the particle and matrix can be considered as a continuous and homogeneous phase. It is acknowledged that the particle diameter of the thermoplastic polyethersulfone phase, which is employed as toughening agent in this study, of the epoxy-rich composites is 0.1-1.5 μm [41].

The hardening behavior of the matrix was simplified as the following linear elasto-power law [76,77]:

$$\begin{cases} \bar{\varepsilon}^{-(\text{el}),m} = E_m^{-1} \bar{\sigma}^{-(\text{el}),m} & \text{if } \bar{\sigma}^{-(\text{el}),m} \leq \sigma_{Ym} \\ \frac{\bar{\varepsilon}^{-(\text{pl}),m}}{\varepsilon_{Ym}} = \left(\frac{\bar{\sigma}^{-(\text{pl}),m}}{\sigma_{Ym}} \right)^{n_m} & \text{if } \bar{\sigma}^{-(\text{pl}),m} \geq \sigma_{Ym} \end{cases} \quad (4.4a, b)$$

where $\bar{\sigma}$ and $\bar{\varepsilon}$ are the equivalent stress and the equivalent strain, respectively, and E_m , n_m , ε_{Ym} and σ_{Ym} are Young's modulus, hardening exponent, yield strain, and yield stress, respectively, of the matrix. The radial component of stress, $\sigma_r^{(\text{pl}),m}$, effective stress, $\bar{\sigma}^{(\text{pl}),m}$, and radial displacement fields, $u_r^{(\text{pl}),m}$, in the plastic zone ($r < R_p$) of the matrix are defined as:

$$\sigma_r^{(\text{pl}),m} = C_2 - \frac{2}{3} C_1 n_m r^{-3/n_m} \quad (4.5a)$$

$$\bar{\sigma}^{(\text{pl}),m} = C_1 r^{-3/n_m} \quad (4.5b)$$

$$u_r^{(\text{pl}),m} = \frac{1}{2} \frac{\varepsilon_{Ym}}{r^2} \left(\frac{C_1}{\sigma_{Ym}} \right)^{n_m} \quad (4.5c)$$

Outside the plastic core ($r > R_p$), the stress components and displacement fields of linear elastic matrix zone can be expressed as:

$$\sigma_r^{(\text{el}),m} = E_m \left[\frac{C_3}{1-2\nu_m} - 2 \frac{C_4}{r^3(1+\nu_m)} \right], \quad \sigma_{\theta\theta}^{(\text{el}),m} = E_m \left[\frac{C_3}{1-2\nu_m} + \frac{C_4}{r^3(1+\nu_m)} \right] \quad (4.6a, b)$$

$$u_r^{(el),m} = C_3 r + \frac{C_4}{r^2} \quad (4.6c)$$

where ν_m is Poisson's ratio of the matrix [78]. To avoid the singular solution of the equivalent stress at the center of particle ($r = 0$), we introduced the curve of nonlinear hydrostatic stress versus volumetric strain as a constitutive model. We defined the radial component of strain, $\varepsilon_{rr}^{(pl),p}$, as one of the unknown variables, C_5 , as follows:

$$\varepsilon_{rr}^{(pl),p} = C_5 \quad (4.7a)$$

$$u_r^{(pl),p} = C_5 r \quad (4.7b)$$

There are actually two types of yield state of the composites near the crack tip:

- Partially yielded domain: yielding occurs in the entire particle and a part of the matrix ($r_p < R_p < r_m$)
- Fully yielded domain: yielding occurs in the entire particle and the entire matrix ($R_p = r_m$)

Firstly, microscopic displacement and stress fields of partially yielded domain ($r_p < R_p < r_m$) are obtained. Through perfect bonding between the particle and the matrix, the continuity in displacement and stress is satisfied as follows:

$$\left\{ \begin{array}{l} \sigma_{rr}^{(el),m} \Big|_{r=R_p} = \sigma_{rr}^{(pl),m} \Big|_{r=R_p} \\ \sigma_{rr}^{(pl),m} \Big|_{r=r_p} = \sigma_{rr}^{(pl),p} \Big|_{r=r_p} \\ u_r^{(el),m} \Big|_{r=R_p} = u_r^{(pl),m} \Big|_{r=R_p} \\ u_r^{(pl),m} \Big|_{r=r_p} = u_r^{(pl),p} \Big|_{r=r_p} \end{array} \right. \quad (4.8a-d)$$

From the definition of R_p and traction boundary condition, the additional boundary conditions are defined as:

$$\begin{cases} \sigma_{rr}^{(pl),m} \Big|_{r=R_p} = \sigma_{Ym} \\ \sigma_{rr}^{(el),m} \Big|_{r=r_m} = S \end{cases} \quad (4.9a, b)$$

The solutions of the coefficients (C_1 - C_5) are then

$$\begin{cases} C_1 = \sigma_{Ym} R_p^{3/n_m} \\ C_2 = \frac{2}{3} \left(\sigma_{Ym} R_p^{3/n_m} \right) n_m r_p^{-3/n_m} + \sigma_{h,MD}^{(pl),p} \left(\varepsilon_v = \frac{3}{2} \frac{\varepsilon_{Ym}}{r_p^3} R_p^3 \right) \\ C_3 = \left\{ \frac{S}{E_m} + 2 \frac{C_4}{r_m^3 (1 + \nu_m)} \right\} (1 - 2\nu_m) \\ C_4 = \left\{ \frac{2E_m}{(1 + \nu_m)} \left(\frac{1}{r_m^3} - \frac{1}{R_p^3} \right) \right\}^{-1} \left[\frac{2}{3} \sigma_{Ym} n_m \left\{ \left(\frac{R_p}{r_p} \right)^{3/n_m} - 1 \right\} + \sigma_{h,MD}^{(pl),p} \left(\varepsilon_v = \frac{3}{2} \frac{\varepsilon_{Ym}}{r_p^3} R_p^3 \right) - S \right] \\ C_5 = \frac{1}{2} \frac{\varepsilon_{Ym}}{r_p^3} R_p^3 \end{cases} \quad (4.10a-e)$$

where R_p can be obtained from the following equation:

$$f(R_p) = R_p^3 - \frac{2C_4(R_p)}{\varepsilon_{Ym} - 2C_3(C_4(R_p))} = 0, \quad R_p \in (r_p, r_m) \quad (4.11)$$

The numerical solution of R_p is obtained by the bisection method within the interval (r_p, r_m) .

Secondly, microscopic displacement and stress fields of fully yielded domain ($R_p = r_m$) are obtained. Through the condition of perfect bonding between the particle and the matrix, the continuity in displacement and stress is satisfied as follows:

$$\begin{cases} \sigma_{rr}^{(pl),m} \Big|_{r=r_p} = \sigma_{rr}^{(pl),p} \Big|_{r=r_p} \\ \mathbf{u}_r^{(pl),m} \Big|_{r=r_p} = \mathbf{u}_r^{(pl),p} \Big|_{r=r_p} \end{cases} \quad (4.12a, b)$$

From the definition of the traction boundary condition, the additional boundary condition is given as:

$$\sigma_{rr}^{(el),m} \Big|_{r=r_m} = S \quad (4.13)$$

The solutions C_1 - C_5 are

$$\begin{cases} C_1 = \left(\frac{2r_p^3 C_5}{\varepsilon_{Ym}} \right)^{1/n_m} \\ C_2 = \frac{2}{3} C_1 n_m r_p^{-3/n_m} + \sigma_{h,MD}^{(pl),p} (\varepsilon_v = 3C_5) \end{cases} \quad (4.14a, b)$$

where the solutions of C_5 can be obtained from

$$\begin{aligned} C_5 &= \begin{cases} C_{5,1} & (S < S|_{C_5=C_{5,double\ root}}) \\ C_{5,2} & (S > S|_{C_5=C_{5,double\ root}}) \end{cases} \\ \{C_{5,1}, C_{5,2}\} &= \left\{ C_5 \left| \frac{2}{3} \sigma_{Ym} \cdot \left(\frac{2C_5}{\varepsilon_{Ym}} \right)^{1/n_m} n_m (1 - f_p^{1/n_m}) = S - \sigma_{h,MD}^{(pl),p} (\varepsilon_v = 3C_5) \right. \right\} \end{aligned} \quad (4.15a-c)$$

where S has double roots at $C_5 = C_{5,double\ root}$, and $C_{5,1} < C_{5,2}$. Through the limit computation of the stress fields of Eq. (4.11) as R_p converges to r_m , the critical traction force to characterize the fully yielded domain, S^{**} , can be computed:

$$S^{**} = \frac{2}{3} \sigma_{Ym} n_m (f_p^{-1/n_m} - 1) + \sigma_h^{(p)} \left(\varepsilon_v = \frac{3\varepsilon_{Ym}}{2f_p} \right) \quad (4.16)$$

The density of plastic energy dissipated by the particle yield in the composites, u_p , can be expressed as the following simplified form:

$$u_p = U_p \times \frac{3f_p}{4\pi r_p^3} = f_p \left[\int_0^{\varepsilon_v} \sigma_{h,MD}^{(pl),p} d\varepsilon_v - \frac{1}{2} \sigma_{h,MD}^{(pl),p} (\varepsilon_v) \cdot \varepsilon_v \right]_{\varepsilon_v=3C_5} = f_p u_p \quad (4.17)$$

where U_p is the dissipated plastic energy of a particle.

4.1.2.2. Modeling of toughness enhancement induced by thermoplastic particle yield

The partially yielded domain must be determined for the numerical analysis of the toughness enhancement of the thermoplastic/epoxy blend. At the macroscopic crack tip, Σ_h can be obtained using Eq. (4.1) based on linear fracture mechanics, which can be applied to the thermoplastic/epoxy system because the crosslinked

epoxy system is a brittle structure. S^* , which is the minimum traction force to cause plastic yield of particle, is defined as the critical surface traction force such that R_p is equal to the particulate radius r_p . Finally, the critical radius of the partially yield domain, ρ^* , in which yielding of a particle occurs, can be described by the following equation because it is preferable for the contour line for the J -integral to be parallel to the y -axis ($\varphi=\pi/2$) [29]:

$$\rho^* = \frac{2(1+\nu_{\text{comp}})^2 K_{\text{Ic}}^2}{9\pi S^{*2}} \cdot \cos^2 \frac{\varphi}{2} \Big|_{\varphi=\pi/2} = \frac{(1+\nu_{\text{comp}})^2 K_{\text{Ic}}^2}{9\pi S^{*2}} \quad (4.18)$$

Similarly, the critical radius of the fully yielded domain, ρ^{**} , can be defined as:

$$\rho^{**} = \frac{(1+\nu_{\text{comp}})^2 K_{\text{Ic}}^2}{9\pi S^{**2}} \quad (4.19)$$

The toughness enhancement can be described by the contour integral (Eq. (4.2)) of u_p . For the particle yield mechanism, u_p is not a constant in the process of contour integration. Therefore, numerical integration is employed to compute the contour integral as follows:

$$\begin{aligned} \Delta G_p &= 2 \times \int_0^{\rho^* (\phi=\pi/2)} u_p d\rho = 2 \times \sum_{k=1}^N u_p(\rho_k) \Delta\rho \\ \rho_k &= k \times \Delta\rho \\ \Delta\rho &= \rho^* / N \end{aligned} \quad (4.20\text{a-c})$$

where N is the number of integration points (set as 10^4 in this study). By introducing Eq. (4.18), Eq. (4.20b, c), and Eq. (4.17) into Eq. (4.20a), the toughness enhancement, ΔG_p , can then be represented by

$$\Delta G_p = 2 \times \sum_{k=1}^N f_p u_p(\rho_k) \left\{ \frac{(1+\nu_{\text{comp}})^2 K_{\text{Ic}}^2}{9\pi S^{*2}} \cdot \frac{1}{N} \right\} \quad (4.21)$$

With the definition of the fracture toughness as $G_{\text{Ic}} = K_{\text{Ic}}^2 (1-\nu_{\text{comp}}^2) / E_{\text{comp}}$, ΔG_p

can be simplified as

$$\Delta G_p = f_p \times G_{Ic} \times \psi_p = G_{Im} \times \frac{f_p \times \psi_p}{1 - f_p \times \psi_p} \quad (4.22)$$

where the contribution of the thermoplastic-particle yield mechanism of the blended toughening agents, ψ_p , is

$$\psi_p = 2 \times E_{comp} \times \frac{(1 + \nu_{comp})^2}{(1 - \nu_{comp})^2} \times \frac{1}{9\pi S^{*2}} \times \left\{ \frac{1}{N} \sum_{k=1}^N u_p(\rho_k) \right\} \quad (4.23)$$

In order to compute Eq. (4.23), E_{comp} , ν_{comp} , and $u_p(\rho_k)$ must be obtained first.

The elastic moduli of the composites is determined by the Mori-Tanaka model [75],

while $u_p(\rho_k)$ can be determined by the proposed formulation in section 4.1.2.1.

For the k th integration point, the hydrostatic tension, S_k , can be determined as

$$S_k = \frac{(1 + \nu_{comp}) K_{Ic}}{3\sqrt{\pi\rho_k}} = \frac{S^*}{\sqrt{\rho_k / \rho^*}} = \frac{S^*}{\sqrt{k/N}} \quad (4.24)$$

4.1.3. Thermoplastic particle bridging-induced toughness enhancement

Douglass *et al.* [37] proposed the toughness enhancement due to rubbery particle bridging mechanism. We quantified the thermoplastic particle bridging-induced toughness enhancement in a similar way. Even though the fracture toughness of PES has not been reported, the elongation limit, Young's modulus, and tensile strength were reported as 6-80%, 2.41-2.83 GPa, and 67.6-95.2 MPa, respectively [79]. Using the linear elasto-perfect plastic model, the dissipated energy density of PES due to tearing, w_0 , can be estimated as 5-75 MPa. Then, toughness enhancement due to tearing can be obtained as the following equation [37]:

$$\Delta G_t \approx 2w_0 r_p f_p \quad (4.25)$$

where r_p is the mean radius of thermoplastic particles. Therefore, the total toughness enhancement can be described as the following form:

$$\Delta G_{ic} = \Delta G_p + \Delta G_t \approx G_{lm} \times \frac{f_p \times \psi_p}{1 - f_p \times \psi_p} + 2w_0 r_p f_p \quad (4.26)$$

4.1.4. Molecular modeling and molecular dynamics simulation of bulk polyethersulfone

4.1.4.1. Molecular modeling of bulk polyethersulfone

For the molecular modeling and relaxation simulation, commercial molecular simulation software Material Studio 5.5 was used [57], and the polymer consistent force-field [80] was employed to describe both the inter- and intra-atomic interactions. Polyethersulfone, the thermoplastic toughening agent, is a typical amorphous engineering thermoplastic with high toughness, strength and rigidity. The chemical structure of polyethersulfone is given in Fig. 4.1. In this study, a polyethersulfone chain containing 60 repeating units was used as an end group. The initial target density of the unit cell containing five polyethersulfone chains was set to 0.01 g/cm^3 for modeling of a dilute condition and periodic boundary conditions were applied in all directions. The initial molecular structure of polyethersulfone was gradually compressed and equilibrated, using the *NVT* ensemble (with constant number of particles, volume, and temperature) at 300K followed by the *NPT* ensemble (with constant number of particles, pressure, and temperature) at 300K and 1atm.

4.1.4.2. Simulation of triaxial tensile loading and unloading in bulk polyethersulfone

Molecular dynamics simulation was employed to obtain the triaxial tensile loading and unloading simulation response of polyethersulfone. A small displacement was applied to the atoms on the surface of the unit cell according to the predefined strain rate of 0.0001/ps along every axis, and the system was relaxed via the *NVT* ensemble simulation. After the relaxation process, the atoms on the surface of the unit cell were displaced again, followed by the same relaxation process. In each relaxation process, the time-averaged stress tensors calculated from the virial theorem were stored as the stress components corresponding to the strain state. This process was repeated until the volumetric strain of the unit cell reached 120%. After the loading simulation, unloading simulations followed at strains of 15%, 45%, 90%, and 120%. During the unloading simulation, the atoms on the surface of the unit cell were displaced according to the predefined strain rate of -0.0001/ps along every axis. For all the ensemble simulations, an open source code for large-scale atomic and molecular simulation tool (LAMMPS) [58] was used with the same force field (PCFF).

4.1.5. Simulation results and discussion

4.1.5.1. Molecular dynamics simulation results of polyethersulfone

To validate the unit cell model of polyethersulfone, we compared the Young's modulus (E), density (ρ), and glass-transition temperature (T_g) of polyethersulfone obtained by molecular dynamics simulation with experimental data reported in the literature [81], as shown in Table 4.1. The procedure for this simulation is

described elsewhere [14,82]. This unit cell model was used for triaxial tensile simulation with LAMMPS. The obtained nonlinear hydrostatic stress-volumetric strain curve is as shown in Fig. 4.2, which shows trends similar to those reported in the literature [83]. Molecular dynamics data were by the least squares method using the following equation:

$$\sigma_h = f_{\text{PES}}(\varepsilon_v) = \frac{a_1}{\varepsilon_v} \exp \left[-0.5 \times \left\{ \ln \left(\frac{\varepsilon_v}{a_2} \right) \times \frac{1}{a_3} \right\}^2 \right] \quad (4.27)$$

where a_1 , a_2 , and a_3 are 56.694MPa, 0.523, and 1.229, respectively. The fracture energy of polyethersulfone by volumetric tension was then determined as follows:

$$\int_0^\infty \sigma_h d\varepsilon_v \approx 174.65\text{MPa} \quad (4.28)$$

The unloading simulations were conducted at strains of 15%, 45%, 90%, and 120%. As shown in Fig. 4.2, the simulation results indicate that the unloading tangent modulus is constantly held as the secant modulus. The unloading curve recovers to the free stress state at a strain state of 0. Therefore, the unloading curves are approximated as a linear function whose slope is the secant modulus.

4.1.5.2. Experimental validation of the proposed multiscale model

To validate the proposed multiscale model, we compared the normalized toughness of thermoplastic/epoxy blends with experimental data as shown in Fig. 4.3. The values of G_{Im} , E_{m} , ν_{m} , σ_{Ym} , and n_{m} were set as 150 J/m², 3.36 GPa, 0.38, 68 MPa, and 3.4, respectively [13,26]. A satisfactory agreement with experimental data is evident as shown in Fig. 4.3.

4.1.5.3. Dependence of the toughness enhancement on mechanical properties of thermoplastic particles

The effect of the nonlinear hydrostatic stress-volumetric strain response of thermoplastic particles on the toughness enhancement of the thermoplastic/epoxy composites was investigated to determine which materials are appropriate for the particles. Two parameters, m_x and m_y , were introduced to simplify the description of various hydrostatic stress-volumetric strain responses of the particles. The stress-strain curves are magnified by m_x and m_y along strain and stress direction, respectively, as shown in Fig. 4.4. For fixed fracture energy of thermoplastic particle ($m_x \cdot m_y = 1$), parametric studies are conducted to provide design guideline.

As shown in Table 4.2, it can be concluded that optimal selection of particles to enhance the fracture toughness through the plastic yield of the particles can be achieved at high m_x and low m_y . Even though the fracture energy of particle is fixed, the toughness enhancement can be improved dramatically by increasing m_x and decreasing m_y . As the ultimate stress of the thermoplastic particles increases, the critical radius of yielded domain decreases. Moreover, the density of dissipated plastic energy increases as the ultimate stress of the thermoplastic particles decreases. In other words, total dissipated energy density induced by plastic deformation of thermoplastic particles clearly decreases as the ultimate stress of the thermoplastic particles increases. In spite of the fixed fracture energy of the employed thermoplastic particle, the fracture toughness of thermoplastic/epoxy blends can be enhanced as the ultimate stress of thermoplastic particle changes.

4.2. Multiscale Analysis of Self-Healing Epoxy/Thermoplastic Blends

In this chapter, multiscale analysis for the self-healing epoxy/thermoplastic blends is conducted. For the prediction of elastic properties of self-healing epoxy/thermoplastic blends, multi-inclusion models are used. The details are described in the section 2.1.4.1. To predict the virgin fracture toughness of self-healing epoxy/thermoplastic blends, the mechanism-based multiscale approach is used. As mentioned in previous section, the total area of active process zone is reduced due to the embedded microcapsules. Therefore, the microscopic energy dissipation is also reduced in proportion to the reduced area of active process zone as follows:

$$K_{Ic}^{\text{virgin,comp}} = K_{Ic}^{\text{comp}} \times e^{-\beta^{\text{virgin}} \times f_{\text{capsule}}} \quad (4.29)$$

Here, β^{virgin} is determined same as previous chapter (Eq. 2.9). Finally, with the consideration of weak interfacial adhesion, the healed fracture toughness of self-healing epoxy/thermoplastic blends can be obtained as follows:

$$K_{Ic}^{\text{healed,comp}} = K_{Ic}^{\text{comp}} \times \frac{\sigma_{\text{cr}}^{\text{cohesive}}}{\sigma_{\text{ultimate}}} \quad (4.30)$$

Using these multiscale descriptions for the prediction of elastic properties, virgin fracture toughness, and healed fracture toughness of self-healing epoxy/thermoplastic blends, the predicted results are described in Fig. 4.5. For various weight fractions of microcapsules and thermoplastic particles, the master curves of self-healing epoxy/thermoplastic blends can be constructed. Using the microscopic dissipating energy mechanisms, intrinsic toughening mechanism, and macroscopic crack shielding effects, the useful multiscale models have been developed. It is expected that this multiscale model can provide useful guidelines

for the analysis of self-healing epoxy/thermoplastic blends.

4.3. Chapter Summary and Conclusions

In this chapter, the multiscale analysis of self-healing epoxy/thermoplastic blends is conducted. Before the multiscale analysis, the multiscale models to predict elastic properties and fracture toughness of epoxy/thermoplastic blends are firstly developed. As the main mechanisms of toughness enhancement of thermoplastic/epoxy blends, we considered plastic deformation in the material near the macroscopic crack tip, and particle bridging in the crack wake. The proposed multiscale model shows a satisfactory agreement with experimental data. From the viewpoint of the plastic yield of toughening agents, the some design guidelines to enhance the fracture toughness of thermoplastic/epoxy blends are provided. Using the microscopic dissipating energy mechanisms, intrinsic toughening mechanism, and macroscopic crack shielding effects, the useful multiscale models have been developed. It is expected that this multiscale model can provide useful guidelines for the design of self-healing epoxy/thermoplastic blends.

Table 4.1. Comparison of linear elastic properties and glass transition temperature (T_g) of polyethersulfone obtained from molecular dynamics simulation with experimental literature.

Present study					Experiment [81]		
E (GPa)	G (GPa)	ν	ρ (g/cm ³)	T_g (K)	E (GPa)	ρ (g/cm ³)	T_g (K)
2.68	0.99	0.36	1.32	499	2.5	1.37	499.15

Table 4.2. Effect of stress-strain characteristics on the improvement in fracture toughness of a thermoplastic/epoxy composites at fixed fracture energy. (The critical radius of the yielded domain is normalized by the critical radius of the partially yielded domain at $m_x=m_y=1$.)

Volume fraction (%)	Magnitude		$\Delta G_p/G_{Im}$	Critical radius of yielded domain		Density of dissipated plastic energy density [MPa]	
	m_x	m_y		Partially yielded	Fully yielded	Partially yielded	Fully yielded
10.57	0.80	1.25	1.176	0.661	0.386	2.433	136.6
	0.90	1.11	1.209	0.818	0.401	6.214	147.0
	1.00	1.00	1.246	1.000	0.419	7.522	157.5
	1.10	0.91	1.286	1.208	0.438	7.739	167.1
	1.20	0.83	1.318	1.443	0.458	7.533	171.4

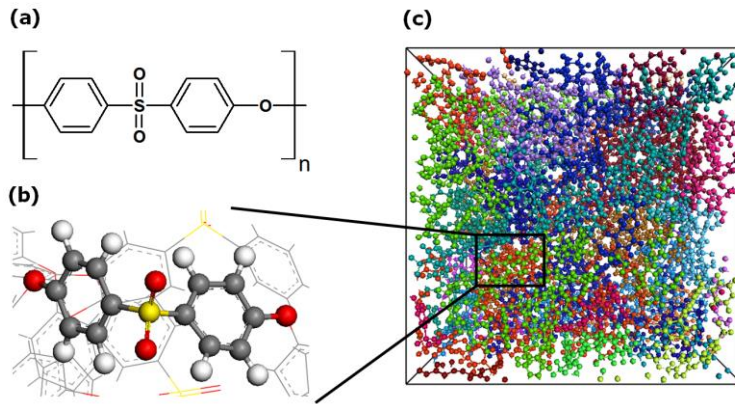


Fig. 4.1. Molecular modeling of polyethersulfone: (a) chemical structure of polyethersulfone [57], (b) monomer of polyethersulfone molecule, and (c) configuration of amorphous unit cell with five polyethersulfone chains.

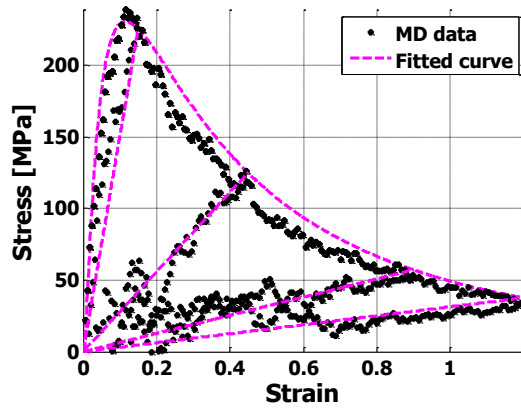


Fig. 4.2. Stress-strain response of triaxial tensile simulation of polyethersulfone: (a) molecular dynamics data, and (b) fitted curve

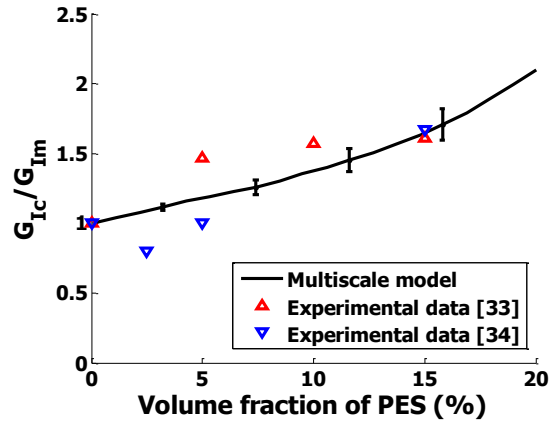


Fig. 4.3. Validation of multiscale model compared to experimental data [84,85].

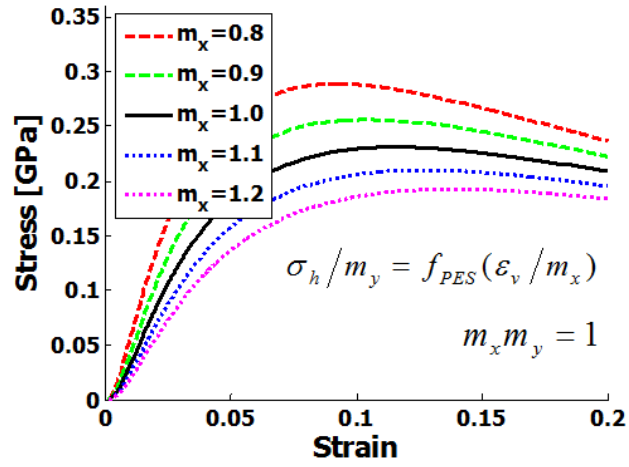


Fig. 4.4. Curve of hydrostatic stress versus volumetric strain of thermoplastic particles magnified view along strain direction (constant fracture energy).

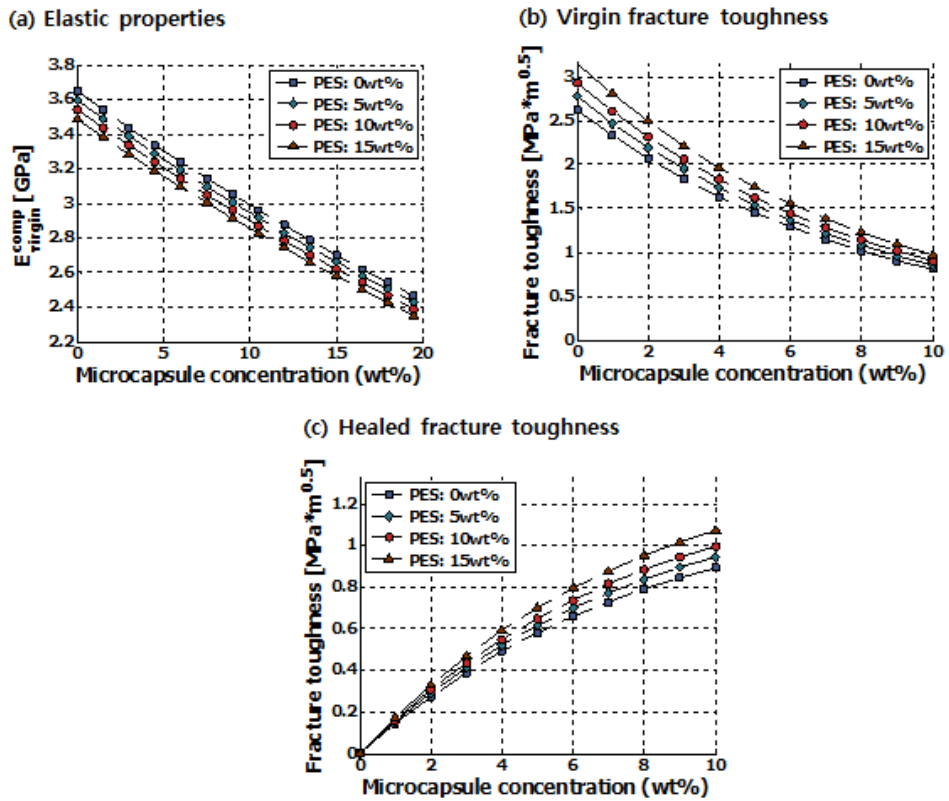


Fig. 4.5. Basic mechanical properties of self-healing epoxy/thermoplastic blends: (a) elastic properties, (b) virgin fracture toughness, and (c) healed fracture toughness.

5. CONCLUSIONS

In this study, we examined the methodology of multiscale mechanical analysis of the self-healing polymer composites that include rigid nanoparticles or thermoplastic particles. Before the multiscale mechanical analysis, we developed multiscale model of self-healing polymer systems for elastic properties, virgin fracture toughness and healed fracture toughness. Using the extrinsic crack healing mechanism and the microscopic energy dissipating mechanisms, the elastic properties, virgin fracture toughness and healed fracture toughness of self-healing composites are quantified. It is expected that the proposed multiscale models can provide useful guidelines for the multiscale design of self-healing polymer composites. The detail conclusions are summarized in the following paragraphs.

A multiscale model of self-healing polymers has been developed including the homogenized elastic properties, virgin fracture toughness, and healed fracture toughness using the micromechanics and the full atomistic molecular dynamics simulations. The maximum theoretical healing efficiency of self-healing polymers was predicted using the molecular dynamics simulations. The time response of mechanical behaviors of self-healing polymers has been characterized using the experiments-based curing kinetics model and the reactive mechanism of healing agents. Using this multiscale model of self-healing polymers, the multiscale analysis of the self-healing polymer nanocomposites and the self-healing epoxy/thermoplastic blends are conducted.

For the multiscale mechanical analysis of self-healing polymer nanocomposites,

the multiscale models to predict elastic properties, fracture toughness and fatigue crack growth behaviors of thermoset polymer nanocomposites are firstly developed. The proposed models show highly satisfactory agreement with experimental data. This is the first attempt to predict fatigue crack growth behaviors of thermoset polymer nanocomposites using the microscopic energy dissipating mechanisms (nanoparticulate debonding-induced plastic yield of nanovoids, and localized shear banding). We believe that the proposed multiscale model can act as the guideline of the characterization of master curves of fatigue crack growth behaviors for various weight fraction systems and the foundation of the fatigue design of the thermoset polymer nanocomposites with design of microscopic energy dissipating mechanisms. Using the microscopic dissipating energy mechanisms, intrinsic toughening mechanism, and macroscopic crack shielding effects, the useful multiscale models have been developed.

For the multiscale analysis of self-healing epoxy/thermoplastic blends, the multiscale models to predict elastic properties and fracture toughness of epoxy/thermoplastic blends are firstly developed. As the main mechanisms of toughness enhancement of thermoplastic/epoxy blends, we considered plastic deformation in the material near the macroscopic crack tip, and particle bridging in the crack wake. The proposed multiscale model shows a satisfactory agreement with experimental data. From the viewpoint of the plastic yield of toughening agents, the some design guidelines to enhance the fracture toughness of thermoplastic/epoxy blends are provided. Using the microscopic dissipating energy mechanisms, intrinsic toughening mechanism, and macroscopic crack shielding effects, the useful multiscale models have been developed.

The proposed multiscale method can be applied to the average diameter of nanoparticle, the molecular structure of thermoplastic particles, and concentration of catalysts in the self-healing polymer composites. In future works, the multiscale method will be extended to consider the design of the functionality and the molecular weight of healing agents, the diameter and the thickness of microcapsules, the aspect ratio and the dispersion of nanoparticles in the mechanical design of the self-healing polymer composites. Furthermore, the current multiscale model cannot reflect the failure fraction of microcapsules and diffusion of healing agents into the crack plane. To achieve the more realistic description of multiscale mechanics for self-healing polymer composites, the failure fraction of microcapsules and diffusion of healing agents will be considered in future works.

**APPENDIX A. STATISTICAL MULTISCALE HOMOGENIZATION
APPROACH FOR ANALYZING POLYMER NANOCOMPOSITES THAT
INCLUDE MODEL INHERENT UNCERTAINTIES OF MOLECULAR
DYNAMICS SIMULATIONS**

A.1. Introduction

To assess the structure-to-properties or nanoparticle size-to-properties relationships through experimental measurement or atomistic simulations of nanocomposites, certain stochastic variations in microstructural parameters and their effect on the properties of nanocomposites must be clearly defined and understood. For instance, fine control of the size of nanofillers for composites remains a challenge and there are mean and standard deviations in the size of nanoparticles inside a nanocomposite [89]. Moreover, the properties of the base polymer matrix, interfacial strength between the nanoparticle and matrix of concern, and spatial distribution of nanoparticles are neither deterministic nor homogeneous [90,91].

Full-atomistic molecular dynamics (MD) simulations have been widely employed to investigate the size-dependent properties of the embedded nanoparticles and to characterize the interphase zone of nanocomposites [16,88,92-96]. The concentration and properties of the interphase zone confirmed from the MD simulation are more easily identified in conjunction with continuum micromechanics than solely by MD simulations. For this reason, attempts to hierarchically bridge MD simulation results to composite micromechanics

[16,49,92-95] or mathematical homogenization [50,88] have been proposed. In a series of successive studies, incorporation of the interphase zone as an additional phase within nanocomposite structures has been proposed to characterize the elastic, thermoelastic, and thermal transport properties—all of which depend on the size of the embedded filler [50,97]. In these computational studies, however, structural uncertainties that may affect the properties of nanocomposites have rarely been considered. In particular, for the dependencies of the physical properties of the nanocomposites on filler size, sufficient microstructural sampling of molecular structures is required to derive statistically convincing conclusions.

In addition to adequate sampling of initial molecular structures, MD simulations depend on the simulation setup, such as the initial random number seed to assign the starting kinetic energy of individual atoms to be further controlled to satisfy Boltzmann's distribution [98]. According to statistical mechanics, the ergodic hypothesis states that the average of sufficiently long simulations provides a reliable ensemble average of the same thermodynamic properties regardless of the initial velocity distribution. Despite the typical long relaxation time (3–5 ns) of the molecular unit cell through isothermal-isobaric ensemble simulations prior to the production runs, the average thermodynamic quantities of polymeric systems in MD simulations cannot avoid model-inherent uncertainties that stem from initial conditions. In MD simulations of polymeric nanostructures, a chaotic flow distribution of the polymer molecules is induced by the initial position and velocity of individual atoms as well as the chain conformation. However, such a chaotic flow distribution in an amorphous polymer is not homogeneous and can generate non-negligible local fluctuations in field quantities unless an enormous number of

atoms is simulated. On the other hand, such uncertainties are not serious factors for simulating ordered crystalline structures. Moreover, the free volume in an amorphous polymer can lead to a local plasticizing effect, which in turn leads to non-negligible deviations in the properties of the same conformations depending on the initial velocity distributions of the atoms.

Minimizing the influence of conformation-dependent local field fluctuations caused by chaotic flows and free volume requires sufficiently long simulations and an enormous number of atoms to represent amorphous states. To reduce unavoidable model-inherent uncertainties, at least 10^7 ensemble frames should be considered [57]. However, MD simulations of polymeric structure cannot fulfill this requirement owing to the limitation of current computational power and memory. Therefore, a mean value-based statistical approach has been the preferred method to obtain reliable elastic properties, in which over 6–10 MD simulations are replicated on the same molecular structure while varying the initial velocity distributions of atoms in the system [13,16,88,99-101]. To reduce the errors originating from uncertain factors in predicting the properties of polymeric systems, for example, Yu et al. [13], Wei et al. [103], and others have typically demonstrated mean values of the properties of polymeric structures with standard deviations over 3 to 6 replications [13,99-102]. Despite the necessity of repeated calculations, however, there have been few attempts to explore the optimal number of repetitions to minimize the influence of model-inherent uncertainty on the properties of polymer nanocomposites obtained from MD simulations. Therefore, to increase the application of MD simulations to explore the multifunctional properties of nanocomposites, proper investigations should be performed to provide useful

guidelines in assessing the inherent uncertainties in MD simulations. Moreover, uncertainties in the properties of interphases that surround embedded nanoparticles in nanocomposites have never been addressed in multiscale modeling approaches.

In this appendix, we performed stochastic analysis of nanocomposites to provide useful guidelines in determining the elastic properties of epoxy-based SiC composites from MD simulations. To determine the proper number of trials, the cumulative average is calculated and discussed. By adopting an inverse analysis scheme that equates the MD simulation results to a three-phase micromechanics model, we propose a novel inverse statistical multiscale bridging method to obtain the probability density of the interphase properties. Propagation of the model-inherent uncertainty described in Table A.1 is addressed by the proposed statistical multiscale bridging method. To the best of our knowledge, this study is the first to quantify the influence of the model inherent uncertainty of MD simulations on the elastic modulus, and to construct a multiscale model that systematically includes this uncertainty. Based on a monoparticulate level multiscale model, an extension to the uncertainties in the size and spatial distribution of SiC nanoparticles inside the epoxy resin was realized by considering a large number of polydisperse representative volume elements (RVE) of nanocomposites.

A.2. Molecular Modeling and Simulation Methodology

A.2.1. Preparation of unit cell

In this study, molecular models of epoxy nanocomposites with a single spherical SiC nanoparticle embedded at the center of the periodic unit cell were employed (Fig. A.1a). To investigate the particle size dependency of elastic properties, four

different epoxy/SiC nanocomposites unit cell systems (Particle radius: 5.18, 7.54, 9.00, or 10.00 Å) were modeled under the same volume fraction (5.8%). Details of the epoxy/SiC nanocomposite unit cell systems and pure epoxy systems are listed in Table A.2. The epoxy resin is composed of triethylenetetramine (TETA[®]) and a diglycidyl ether of bisphenol F (EPON862[®]) as the curing agent and epoxy monomer, respectively. To describe crosslinking between the epoxy monomer and curing agent, a unit model of the representative crosslinked network is employed (Fig. A.1b). This crosslinking method yields accurate results for the elastic properties [49,97], density [49,50,94,97], glass transition temperature [94], and thermal conductivity [50,97]. There are 2 and 6 curing sites in single molecules of EPON862[®] and TETA[®], respectively. In this study, the molecular ratio of epoxy monomer to curing agent was set to 3:1 to equate the number of curing sites between the two molecules. The curing ratio of the crosslinked epoxy was also set to 0.61 in line with a previous study [94].

All molecular modeling and MD simulations were conducted with Materials Studio 5.5.3. The COMPASS (ab initio Condensed-phase Optimized Molecular Potential for Atomistic Simulation Studies) [57] force field, which is built into Materials Studio 5.5.3, was used to describe the inter- and intra-atomic interaction forces. The target density of the neat epoxy and epoxy/SiC nanocomposite periodic unit cell systems was set to 1.20 g/cm³ in accordance with experimental results [104]. The Amorphous Cell module[®] was used to construct the amorphous unit cell system of neat epoxy and epoxy/SiC nanocomposites with the target density at 300 K and 1 atm. After constructing the initially defined unit cell system, the total potential energy of the unit cell was minimized, using the conjugate gradient

method. Then, NVT (isothermal)-ensemble and NPT (isothermal and isobaric) simulations were performed to equilibrate the unit cell systems at 300 K and 1 atm for 500 and 2000 ps, respectively.

A.2.2. Production run for elastic properties

Here, the elastic stiffness tensor was calculated from the Parrinello-Rahman fluctuation method with an ensemble average of 10^4 strain fluctuated frames. More procedures that are detailed are introduced in Chapter 2.

A.2.3. Statistical analysis of epoxy nanocomposites

To quantify the model-inherent uncertainty of the epoxy nanocomposites, a medium-sized statistical approach (including approximately 30 times replications) was employed. Such an approach is widely used to obtain statistics such as the mean and standard deviation. The average shifted histogram method [106] was employed to minimize the dependence of the bin origin on the shape of the histogram. The estimated probability density distribution (Fig. A.2) shows a lognormal distribution. In the following sections, data fit to a lognormal distribution with approximately 32 replications were used. The lognormal approximation requires only two statistical parameters, the mean and standard deviation, of logarithmically mapped data. These parameters were obtained for the elastic properties and discussed in view of the size-dependency of the reinforced filler.

A.3. Statistical Multiscale Bridging Method

In this section, a statistical multiscale bridging method is proposed after a brief review of previous studies on multiscale bridging methodologies. In a previous study, Yang and Cho proposed a multiscale-analysis scheme to characterize the filler size-dependent interface effect (size effect) of silica nanoparticles on the elastic properties of spherical nanoparticle-reinforced polymer nanocomposites [16]. The interphase characteristics were extracted from an inverse analysis of the multi-inclusion model, after obtaining the elastic properties from the atomistic structures.

The statistical multiscale bridging method proposed here includes the model uncertainty (Fig. A.3); in this model, the elastic properties of the interphase are defined as uncertain as are those of the matrix and composites. To include the model uncertainty of the interphase, a Monte Carlo-based approach (including 10^5 trials) is conducted. After identifying the probability density distributions of the interphase elastic properties, an investigation is conducted on how the model-inherent uncertainties are propagated to the homogenized elastic properties for complex RVE systems whose reinforced fillers include geometric uncertainties of filler radius and location.

A.3.1. Brief review of previous multiscale bridging methodologies

The reinforced filler-size dependent interface effect stems from the structural change of adsorption layer in the vicinity of the embedded fillers [16,49,88,92-95]. To describe the variation in filler-size dependency of the overall elastic properties, the equivalent micromechanics model (i.e., multi-inclusion model of Hori and

Nemat-Nasser [59]) of the nanocomposites has been defined. Yang and Cho proposed a multiscale bridging modeling procedure through a multi-inclusion model [16] in which the overall elastic stiffness tensor \mathbf{C} of a composite composed of matrix ($r = 1$), interphase ($r = 2$), and nanoparticle ($r = 3$) is given as follows:

$$\mathbf{C} = \mathbf{C}_{\text{inf}} \left[\mathbf{I} + (\mathbf{S} - \mathbf{I}) \left(\sum_{r=1}^3 f_r \mathbf{\Phi}_r \right) \right] \left[\mathbf{I} + \mathbf{S} \left(\sum_{r=1}^3 f_r \mathbf{\Phi}_r \right) \right]^{-1} \quad (\text{A.2})$$

where \mathbf{C}_{inf} is the stiffness tensor of the infinite medium; f_r the volume fraction of the r^{th} phase; and \mathbf{S} and \mathbf{I} are Eshelby's tensor and the identity tensor, respectively. The eigenstrain concentration tensor of the r^{th} phase $\mathbf{\Phi}_r$ is expressed as follows:

$$\mathbf{\Phi}_r = \left[(\mathbf{C}_{\text{inf}} - \mathbf{C}_r)^{-1} \mathbf{C}_{\text{inf}} - \mathbf{S} \right]^{-1} \quad (\text{A.3})$$

where \mathbf{C}_r is the stiffness tensor of the r^{th} phase, and eigenstrain of r^{th} phase $\boldsymbol{\varepsilon}_r^*$ could be represented by $\boldsymbol{\varepsilon}_r^* = \mathbf{\Phi}_r \boldsymbol{\varepsilon}^0$ where $\boldsymbol{\varepsilon}^0$ is macroscopic strain. For example, eigenstrain of interphase zone $\boldsymbol{\varepsilon}_{\text{int}}^*$ is obtained by $\boldsymbol{\varepsilon}_{\text{int}}^* = \mathbf{\Phi}_{\text{int}} \boldsymbol{\varepsilon}^0$. To characterize the effective interphase thickness, we have previously proposed an approach based on the second moment strain energy [48]. The interphase thickness and its elastic properties are determined by the particle size-dependent stiffness of the nanocomposites and by matching the deformation energy to a full atomic model. As shown in the results (interphase thickness and its elastic properties) of a previous study (Table A.3), the interphase thickness is proportional to the reinforced filler radius. Therefore, in this study, the relative interphase thickness (t_{int}/r_p) was used to reflect the proportionality constant that defines the dependency

of the interphase thickness on the filler size (0.840). In fact, the interphase thickness converged at 1 nm, as discussed previously [48]. The relative thickness was constant when the filler radius was below 1 nm.

A.3.2. Numerical algorithm for statistical multiscale bridging

Here, a numerical iterative inverse algorithm is proposed to characterize the uncertainty of the interphase elastic properties. The uncertainties in the elastic properties of the matrix and composite, calculated from the MD simulations, follow a lognormal distribution. This distribution can be represented by two statistical parameters, i.e., the mean and standard deviation of the logarithmically mapped elastic properties. Therefore, we can set this inverse problem as a system of four simultaneous nonlinear equations as follows:

$$\begin{aligned}
 &\text{Unknowns: } \text{avg}(\log(E_{\text{int}})), \text{std}(\log(E_{\text{int}})), \text{avg}(\log(G_{\text{int}})), \text{std}(\log(G_{\text{int}})) \\
 &\text{Equilities: } \text{avg}(\log(E_{\text{comp}}^{\text{micromech}})) \approx \text{avg}(\log(E_{\text{comp}}^{\text{MD}})), \text{std}(\log(E_{\text{comp}}^{\text{micromech}})) \approx \text{std}(\log(E_{\text{comp}}^{\text{MD}})) \quad (\text{A.4}) \\
 &\quad \text{avg}(\log(G_{\text{comp}}^{\text{micromech}})) \approx \text{avg}(\log(G_{\text{comp}}^{\text{MD}})), \text{std}(\log(G_{\text{comp}}^{\text{micromech}})) \approx \text{std}(\log(G_{\text{comp}}^{\text{MD}}))
 \end{aligned}$$

where $E_{\text{comp}}^{\text{micromech}}$, $G_{\text{comp}}^{\text{micromech}}$ and $E_{\text{comp}}^{\text{MD}}$, $G_{\text{comp}}^{\text{MD}}$ are the effective Young's and shear moduli of nanocomposites obtained from the multi-inclusion model and MD simulations, respectively; E_{int} , and G_{int} are the Young's and shear moduli, respectively, of the interphase; and $\text{avg}(x)$ and $\text{std}(x)$ are mean and standard deviation, respectively, of x . The inverse algorithm is proposed to match only the mean and standard deviation of the logarithmically mapped elastic properties between the MD and multi-inclusion model results. The nanoparticle elastic properties were obtained from experimental reference data ($E_{\text{par}} = 451.6$ GPa, $G_{\text{par}} = 182.5$ GPa).

Details of the iterative inverse algorithm are described in Table. A.4. Initially,

the elastic properties of the interphase were assigned the same probability density distributions as those of the elastic properties of the matrix. Through lognormal random generation of the elastic properties of the matrix and interphase, the probability density distribution of the multi-inclusion solution was obtained using a Monte Carlo simulation. The obtained solutions were compared with the MD simulation results as shown in Eq. (A.4). To solve Eq. (A.4), a bi-section method-based solver is proposed. Efficient gradient-based methods such as steepest descent, line search, and conjugate gradient methods are widely used in a multivariate nonlinear system. However, in this particular problem, the mean and standard deviation of the equivalent micromechanics solutions are noisy because of the limited number of trials (10^5), which are nonetheless sufficient for the Monte Carlo simulation. Therefore, the micromechanics solution hyper-surface shows a non-differentiable, continuous, and monotonic tendency. Consequently, a modified bi-section method was employed to solve Eq. (A.4). The proposed algorithm converged at $k = 80\text{--}100$ where e_{tol} was set to 0.01. The micromechanical computation of the overall elastic properties through Eq. (A.2) and Eq. (A.3) required little computational time, e.g., only 3–5 s on an Intel Core i5 processor for 10^5 micromechanics computations.

A.3.3. Statistical analysis that considers filler geometric uncertainties

A.3.3.1. RVE setup

Cho et al. [88] and Shin et al. [50] analyzed a nanocomposite RVE that contained 27 (3^3) nanoparticles with stochastic variations in properties such as filler radius and location. Interphase elastic properties obtained from the MD

simulation results and two-scale homogenization method were applied to the multi-particulate RVE system. Each interphase zone had different elastic properties as a function of the corresponding particulate radius. In the present study, the influence of model-inherent uncertainty propagation on the elastic properties of multi-particulate RVE systems was investigated.

To determine how many nanoparticles were required to represent entire mixture on average, statistical treatments were carried out for three different types of microstructure, each of which included 10, 20, or 30 inclusions with the corresponding interphase and matrix phases. For each type, approximately 100 random microstructural models were constructed with DIGIMAT[®] software (Fig. A.4a) [107,108]. Every nanoparticle radius followed a beta distribution (mean: 7.54 Å, standard deviation: 2.44 Å). Although this distribution resembles that of a normal distribution in terms of having a single symmetric peak, the beta distribution (Fig. A.4b) has clear upper and lower limits (2.08 and 12.99 Å, respectively). The material properties of the interphase and matrix follow a lognormal distribution as predicted in the previous sections. The position of every particle is uniformly and randomly distributed, and satisfies the feasible condition of non-overlapping interphases. The overall volume fraction was fixed at 5.8%—the same global volume fraction as in the periodic unit-cell model that included a single particle in the previous sections. To conduct homogenization computations for the periodic microstructural models, an asymptotic homogenization scheme was employed. To determine the proper number of nanoparticles of an RVE, the relative error ε_{rel} was fixed at 2.5%. The number of nanoparticles was determined such that coefficient of variation ($\text{CoV} = \text{standard deviation} / \text{mean}$) of the elastic properties

was less than ε_{rel} when considering the geometric uncertainties of the fillers.

A.3.3.2. Review of two-scale homogenization method of linear elastic composites

Here, we employed the two-scale homogenization method, a well-established numerical method to describe mechanical, thermal, electrical, and other physical properties of macroscopic structures with periodic heterogeneous microstructures. Detailed formulations for the linear elastic homogenization are provided in references [109,110].

To effectively describe both macroscopic and microscopic fields, two scale coordinates \mathbf{X} (= macroscopic coordinates) and \mathbf{y} (= microscopic coordinates) are introduced. The displacement fields \mathbf{u} of the global coordinates can be asymptotically expanded by ε ($=|\mathbf{x}|/|\mathbf{y}| \ll 1$), as follows:

$$\mathbf{u} = \mathbf{u}_0 + \mathbf{u}_1\varepsilon + \mathbf{u}_2\varepsilon^2 + \dots \quad (\text{A.5})$$

By taking the limit ($\varepsilon \rightarrow 0$), the microscopic boundary value problem for the unit cell, denoted by Y , yields the following variational form:

$$\int_Y \frac{\partial \delta \mathbf{u}}{\partial \mathbf{y}} : \mathbf{C} : \left(\mathbf{I} - \frac{\partial \chi(\mathbf{x}, \mathbf{y})}{\partial \mathbf{y}} \right) d\mathbf{y} = 0 \quad (\text{A.6})$$

where the characteristic function χ is defined as follows:

$$\mathbf{u}_1(\mathbf{x}, \mathbf{y}) = -\chi(\mathbf{x}, \mathbf{y}) : \frac{\partial \mathbf{u}_0(\mathbf{x})}{\partial \mathbf{x}} \quad (\text{A.7})$$

In Eq. (A.7), χ indicates the microscopic deformation field under the unit macroscopic strain fields. By solving Eq. (A.6), the microscopic displacement fields can be obtained under the prescribed unit cell macroscopic strain. In the macroscopic problem, the constitutive equation is determined by the solution of the

microscopic boundary value problem; the homogenized elastic property \mathbf{C}^H provides the macroscopic stress $\boldsymbol{\Sigma}$ under the unit macroscopic strain \mathbf{E} as follows:

$$\boldsymbol{\Sigma}(\mathbf{x}) = \frac{1}{|Y|} \int_Y \boldsymbol{\sigma}(\mathbf{x}, \mathbf{y}) d\mathbf{y} = \left[\frac{1}{|Y|} \int_Y \mathbf{C} - \mathbf{C} : \frac{\partial \chi}{\partial \mathbf{y}} d\mathbf{y} \right] : \mathbf{E} = \mathbf{C}^H : \mathbf{E} \quad (\text{A.8})$$

Therefore, the homogenized elastic property \mathbf{C}^H can be computed from Eq. (A.9), which describes the macroscopic stress $\boldsymbol{\Sigma}$ (= volume average of microscopic stress $\boldsymbol{\sigma}$) under the unit macroscopic strain \mathbf{E} :

$$\mathbf{C}^H = \frac{1}{|Y|} \int_Y \mathbf{C} - \mathbf{C} : \frac{\partial \chi}{\partial \mathbf{y}} d\mathbf{y} \quad (\text{A.9})$$

To obtain the elastic modulus of a polycrystalline state, Hill's model is employed [50,88,105].

A.4. Simulation Results and Discussion

A.4.1. Cumulative average response of Young's moduli

Typically, 6–10 trials (replications) are carried out to obtain reliable elastic properties for the molecular unit cell systems. However, the reliability of the sample mean (obtained from an average of 6–10 trials) is not verified in other studies. In this section, a cumulative average (CMA) analysis of Young's moduli is carried out to characterize the reliability of the obtained elastic properties with respect to the number of trials. The normalized CMA of Young's moduli, defined as $\sum_{j=1}^i E_{\text{comp}}^{\text{MD}}(j) / \sum_{j=1}^{\text{Total \# of Trials}} E_{\text{comp}}^{\text{MD}}(j)$ where $E_{\text{comp}}^{\text{MD}}(j)$ is Young's modulus obtained from the MD simulation at the j^{th} trial, clearly converged to one (Fig. A.5). As shown in the figure, 8–10 trials provide reliable elastic properties, which deviate only 3% from the reference data (obtained elastic properties from 32 trials).

If 20–24 trials are considered, the deviation is only 1%. This shows convergence of the deviation. However, the deviation is nearly 10% for less than 5 trials. This critical deviation can be avoided through repeated simulations (Fig. A.5).

A.4.2. Mean and standard deviation of nanocomposite elastic properties

The mean and standard deviation of Young's and shear moduli are compared with the Mori-Tanaka solution those from other studies [16,88] (Table A.5). Although the statistical multiscale analysis is based on the lognormal distribution of the elastic properties, the mean and standard deviation of the elastic properties are listed in the table for ease of comparison with other studies. The Mori-Tanaka solution is a micromechanics solution without the interface effect, i.e., only two phases are considered (the matrix and particle). The reinforcing effect of the nanoparticle becomes more marked as the filler size decreases. Results for the mean elastic properties show a clear filler size-dependent effect of the interface. As the radius of the reinforced filler decreases, the impact of the interface on the elastic properties becomes more dominant because the surface area-to-volume ratio increases. Consequently, the effect of the interface on the elastic properties becomes more dominant as the reinforced particle radius decreases [16,49,88,92-95].

Table A.5 also shows that the particle radius and standard deviation of Young's and shear moduli of the nanocomposites tend to be inversely related. As mentioned earlier in Section A.1, the inherent uncertainties of the MD model depend on the unit cell size during ensemble simulations of polymeric structures, when each molecule shows chaotic mobility governed by the initial location and velocity of

the atoms. Such mobility exhibits an atomistic path-dependent plastic history around free volume, which causes statistical fluctuation of the elastic properties. This statistical fluctuation is reduced gradually as the unit cell size increases. In other words, the variance of the elastic properties stemming from the inherent uncertainty of the MD model decreases as the unit cell size increases. This could explain the trend invariance in Table A.5.

The unit cell size (\AA) is proportional to the reinforced filler radius (\AA) owing to the fixed volume fraction (5.8%) of the reinforced filler (Table A.2). Therefore, the decreases in the standard deviations of Young's and shear moduli as the filler radius increases are straightforward. As shown in Table A.5, this tendency was also observed in other studies [13,111]. Yang and Cho [111] conducted MD simulations to investigate the influence of filler volume fraction on the composite elastic properties. For the same filler radius, the employed unit cell systems have different filler volume fractions. The obtained results show a clear tendency for the standard deviation and CoV of the elastic properties to be inversely related to the unit cell size. Yu et al. [13] conducted MD simulations to determine the dependence of the elastic properties of crosslinked epoxy nanocomposites on the filler size for the same volume fraction of reinforced filler. Consistent with the present study, the standard deviation of the elastic properties clearly declined as the filler radius increased. Therefore, the standard deviation of the elastic properties clearly depends on the unit cell size.

Table A.5 also shows the size dependency of homogeneous unit cell systems that consist of pure epoxy. Despite the similar means of Young's moduli for the four different cases considered, the CoVs of Young's moduli decreased as the unit cell

size increased. The variance of the elastic properties decreased as the homogeneous unit cell size increased [112]. Therefore, the simulated results in Table A.5 are quite reasonable. At the same time, the CoVs of the elastic properties of pure epoxy decreased more rapidly than those of the nanocomposites in the considered dimension of employed unit cell systems whose cubic cell length is below 5 nm. This is because the variance of the elastic properties of the interface increases owing to the decrease in structural crystallinity as the particulate radius increases (see section A.4.3 for details). However, these tendencies are not expected for larger unit cells. As the filler radius increases, the surface of the nanoparticle becomes flatter, and the absolute interphase thickness converges to approximately 1 nm [48]. Therefore, these tendencies are expected to change as the particulate radius increases.

Before obtaining statistical response of interphase elastic properties, the mean and standard deviation of the nanocomposite elastic properties are fitted to smooth curve. The mean and standard deviation of Young's and shear moduli are fitted to an exponential function of the particle radius as follows:

$$E_{\text{comp}}^{\text{avg}}(G_{\text{comp}}^{\text{avg}}) = E_{\text{M-T}}(G_{\text{M-T}}) + \alpha_{E(G)} e^{-\beta_{E(G)} r_p}, \quad E_{\text{comp}}^{\text{stdev}}(G_{\text{comp}}^{\text{stdev}}) = \gamma_{E(G)} e^{-\zeta_{E(G)} r_p} \quad (\text{A.10})$$

where r_p is the particulate radius (\AA), and the coefficients α_E , α_G , β_E , β_G , γ_E , γ_G , ζ_E , and ζ_G are 1.57, 0.77, 0.081, 0.110, 0.558, 0.240, 0.055, and 0.064, respectively. The Mori-Tanaka solutions are 4.37 GPa for Young's modulus and 1.60 GPa for the shear modulus. To describe the dependence of pure epoxy systems on the unit cell size, the standard deviation of the matrix is fitted by an exponential function of the matrix volume (\AA^3) as follows:

$$E_{\text{mat}}^{\text{avg}}(G_{\text{mat}}^{\text{avg}}) = 3.87(1.46), \quad E_{\text{mat}}^{\text{stdev}}(G_{\text{mat}}^{\text{stdev}}) = \eta_{E(G)} e^{-\zeta_E(G)(V_{\text{mat}} - \zeta_E(G))} \quad (\text{A.11})$$

where V_{mat} is the matrix volume, and the coefficients η_E , ζ_E , ζ_E , η_G , ζ_G , and ζ_G are 0.42, 5.76×10^{-6} , 0.50, 0.156, 6.42×10^{-6} , and 0.50, respectively. In the following sections, Eq. (A.11) is employed to describe the standard deviation of the matrix phase as a function of the matrix volume.

A.4.3. Uncertainties of interphase elastic properties

Through the proposed numerical algorithm (Fig. A.3; Table A.4), the mean and standard deviation of the elastic properties of the interphase were estimated (Table A.6). As the radii of the nanoparticles increased, the moduli of the effective interphase decreased, in accord with previous studies [48]. As the particulate radius increased, the nanoparticle surface flattened. Fewer polymer molecules were then included in the van der Waals radius of the particulate surface atom because more nanoparticulate atoms occupied the space determined by this van der Waals radius owing to the lower surface curvature. This is the main reason for the structural weakness of the adsorbed polymer chains, which causes the mean elastic moduli of the interphase to increase with increasing nanoparticulate radii.

In contrast, the standard deviation of the elastic properties of the interphase shows a tendency contrary to the mean elastic properties of the interphase. Adsorbed polymer chains around a nanoparticle show crystallinity where strong nonbond interactions occur between the polymer chain and reinforced nanoparticles such as carbon material [95]. As discussed in Section A.1, the variance of the elastic properties of the amorphous state is higher than that of the

crystalline phase. Therefore, the variance of the elastic properties of the interphase is expected to decrease with the particulate radius (Table A.6) because the interphase around a smaller filler has a higher degree of crystallinity. Interestingly, the CoVs of the elastic properties of interphase are less than those of the matrix. This result is consistent with the view that a high degree of crystallinity of the interphase decreases the CoVs of its elastic properties.

To construct stochastic interphase model applicable to various particulate radii r_p , a simple mathematical form is proposed for the elastic properties of the interphase E_{int} :

$$E_{\text{int}}(r_p, w_{\text{MD}}) = E_{\text{int}}^{\text{avg}}(r_p) + E_{\text{int}}^{\text{stdev}}(r_p) \times (w_{\text{MD}} - 1) \quad (\text{A.12})$$

where w_{MD} , the normalized lognormal distribution with one mean and one variance, is introduced to consider the inherent uncertainty of the MD model. Specifically, w_{MD} is equal to one if there is no model-inherent uncertainty. The mean and standard deviation of the left-hand side of Eq. (A.12) are satisfied by $E_{\text{int}}^{\text{avg}}(r_p)$ and $E_{\text{int}}^{\text{stdev}}(r_p)$, respectively, which are obtained as follows by quadratic spline interpolation through four discrete data points with the different radii listed in Table A.6:

$$\begin{aligned} E_{\text{int}}^{\text{avg}}(r_p) &= 0.0207r_p^2 - 0.6471r_p + 10.747 \\ E_{\text{int}}^{\text{stdev}}(r_p) &= 0.0024r_p^2 - 0.0285r_p + 0.1257 \end{aligned} \quad (\text{A.13})$$

This stochastic interphase model is applied to the multi-particulate unit cell system in Section A.4.4.3.

A.4.4. Propagation of inherent uncertainties of MD model

A.4.4.1. Verification of statistical three-phase multi-inclusion model through monodisperse nanocomposites

In this study, only the mean and standard deviation of the logarithmically mapped elastic properties of the interphase are obtained from the proposed numerical iterative algorithm (Table A.4). As shown in Fig. A.6, the probability density distribution regenerated from the obtained statistical parameters (matrix, lognormal from MD; interphase, lognormal from Eqs. (A.12) and (A.13); and particle, deterministic from reference [94]) could generate probability density distributions for the elastic properties of the nanocomposite comparable in accuracy to the MD results through Monte Carlo simulations of the multi-inclusion model (Eqs. (A.2) and (A.3)). Fig. A.6 shows that the lognormal distribution of the elastic properties for the interphase enables a statistical response of the polymeric nanocomposites comparable to that of the MD results. In the following section, the stochastic interphase model (Eqs. (A.12) and (A.13)) is employed to analyze how the model-inherent uncertainties are propagated to the homogenized elastic properties of multi-particulate epoxy nanocomposite systems, including uncertainties in the size and spatial distribution of SiC nanoparticles.

A.4.4.2. Determination of RVE size and influence of geometric uncertainties

To determine the proper number of RVEs, three types of multi-particulate (MP) periodic unit cell systems with different numbers of inclusions are employed. As shown in Table A.7, the CoVs of homogenized Young's moduli decrease as the number of inclusions increases. Because the relative error ε_{rel} is fixed at 2.5% in

this study, we assume 30 inclusions to represent the macroscopic elastic behavior of nanocomposites, including uncertainties of the filler radii and location where the CoV of Young's moduli is lower than the relative error ε_{rel} .

To discuss the results in greater detail, homogenized Young's moduli about mono-particulate nanocomposites are computed for minimum radius ($r_p = 2.08 \text{ \AA}$), maximum radius ($r_p = 12.99 \text{ \AA}$), and average radius ($r_p = 7.54 \text{ \AA}$). Those Young's moduli provide upper bound, lower bound, and regular system values without any morphological uncertainties of reinforced fillers of homogenized Young's moduli of multi-particulate system are computed, respectively.

Interestingly, every multi-particulate system provided similar Young's moduli (5.46–5.53 GPa). However, these values were roughly 5% higher than the Young's modulus of the regular system. This is because the solution of the regular system does not consider the local non-dilute interaction between individual particles and the effective interphase. When the multi-particulate system is polydisperse, the stress concentration effect between individual particles and the effective interphase causes underestimation of the regularly assumed system. The mean homogenized Young's moduli of the multi-particulate system satisfies the upper and lower bounds, as proposed by Cho et al. [88]. In the following section, the propagation of model-inherent uncertainties to the homogenized elastic properties is investigated and discussed.

A.4.4.3. Discussion concerning the influence of inherent uncertainties of the MD model on the homogenized elastic properties of RVE

To investigate how propagation of inherent uncertainties of the MD model affect

the homogenized Young's moduli of polydisperse multi-particulate nanocomposite systems, repeated simulations were conducted (Table A.8). To compare the influence of MD uncertainty with that of geometric uncertainties, 100 replications with different MD uncertainty conditions were conducted for a fixed-geometry polydisperse multi-particulate system and (denoted as "Only MD uncertainty" in Table A.8). In this case, the influence of geometric uncertainty is not considered. To investigate the correlation between MD uncertainty and geometric uncertainty, repeated simulations that considered both uncertainties were conducted (denoted as "Both uncertainties" in Table A.8). MD uncertainty causes uncertainty in the material properties of the interphase and matrix. The former is obtained from Eq. (A.13) in Section A.4.3, whereas the mean for the latter is simply defined as 3.87 GPa (Table A.6). However, obtaining the standard deviation of the matrix from MD simulations for large systems (e.g., MP10, MP20, and MP30) is difficult owing to the high degrees of freedom. Here, it was simply defined as a function of the number of nanoparticles N_p , as proposed by Matheron et al. [113]:

$$E_{\text{mat}}^{\text{stddev}}(N) = \varpi / \sqrt{N_p} \quad (\text{A.14})$$

For a constant volume fraction system, the matrix volume is proportional to N_p . The coefficient ϖ is determined by Table A.6 as 0.38 because the standard deviation of Young's moduli for the matrix is 0.38 for nanocomposites having a single nanoparticle.

As shown in Table A.8, the mean homogenized Young's moduli decreases by roughly 1% when MD uncertainty is combined with geometric uncertainty. Directly proving why the mean homogenized elastic properties decrease due to uncertainty of the material properties that stems from the inherent uncertainty of

the MD model is difficult. However, the simple numerical examples of 1-D spring systems that provide relevant statistical insights. As shown in Fig. A.7, variation in the material properties of each spring does not influence the mean effective spring for the parallel system (Voigt bound). However, uncertainty in the material properties of the spring is important for a serial system (Reuss bound). The mean effective spring decreases owing to uncertainty in the material properties of each spring element. In this regard, the decrease in the mean homogenized Young's moduli (Table A.8) is explained because polydisperse multi-particulate nanocomposite systems are complicated combinations of serial and parallel systems. Hill's average that is arithmetic average of Voigt and Reuss bounds shows also decreasing tendency of effective material properties due to the influence of material properties uncertainties [114]. The inherent uncertainties of the MD model are reflected as uncertainties in the material properties of the interphase and matrix. Therefore, uncertainty in the material properties of each phase causes the mean homogenized Young's moduli to decrease for polydisperse multi-particulate nanocomposite systems (Table A.8).

In contrast, the MD uncertainty is nearly uncorrelated with the geometric uncertainty of reinforced fillers. As shown in Table A.8, the variance in the case where both geometric and MD uncertainty are considered is almost identical to the sum of each case (denoted as " $\text{Var}_{\text{Geo}} + \text{Var}_{\text{MD}}$ " in Table A.8). Therefore, the variance in the case where geometric uncertainty is combined with uncertainty in the material properties is roughly predicted by the simple summation of each case. The influence of MD uncertainty on the variance of the homogenized Young's moduli is half of that of geometric uncertainty. Although MP30 could be regarded

as an RVE without considering the inherent uncertainty of the MD model, representative characteristics of MP30 is not held when MD model inherent uncertainty is considered.

A.5. Summary of Appendix A

A statistical multiscale model of polymer nanocomposites was established to consider the inherent uncertainty of the MD model, which stems from randomness of the initial velocity distribution of the atoms. This was achieved by using MD simulations, three-dimensional micromechanics analysis, and finite-element homogenization analysis. The inherent uncertainty of the MD model causes uncertainties in the materials properties of each phase (nanoparticle, interphase, and matrix). We examined the influence of the unit cell size and the nanoparticle radius on the statistical nature of the elastic properties for polymer nanocomposites.

Three major conclusions were drawn:

- Uncertainties in the elastic properties obtained from MD simulations showed a lognormal distribution for every unit cell employed in the study. The typically used number of replications (6–10 trials) showed deviations of roughly 3% from the converged elastic properties obtained from MD simulations. Unlike in crystalline systems, this non-negligible MD uncertainty was unavoidable despite sufficient relaxation of polymer molecular systems.
- As the unit cell size increased, the overall elastic properties of pure epoxy matrix and polymer nanocomposites decreased. However, the standard deviation of the elastic properties increased as the nanoparticle radius increased at the interphase zone

- The proposed statistical multiscale model was verified through nanocomposite systems that included a single nanoparticle embedded in the center of a cubic system. For multi-particulate nanocomposite systems, the impact of MD uncertainty on the homogenized elastic properties of the polymer nanocomposites was half that of the geometric uncertainty. Additionally, the effect of MD uncertainty was almost uncorrelated with that of geometric uncertainty. Importantly, however, the mean homogenized Young's moduli decreased when MD uncertainty was combined with geometric uncertainty.

Therefore, we conclude that the current statistical multiscale model is essential for characterizing how propagation of inherent uncertainty of the MD model affects the homogenized Young's moduli of multi-particulate nanocomposite systems. In particular, the decrease in the mean homogenized Young's moduli is a critical issue for reliability-based design and optimization of polymer nanocomposites.

Table A.1. Overview of model to understand how uncertainty that stems from initial velocity distribution of individual atoms is propagated to homogenized elastic properties of representative volume element that includes 30 nanoparticles.

Multiscale simulation tool	Input uncertainties	Output uncertainties
Molecular Dynamics (Section A.2)	Initial velocity distribution of individual atoms	Elastic properties of ✓ Matrix ✓ Particle ✓ Nanocomposites
Multi-inclusion model (Section A.3.2)	Elastic properties of ✓ Matrix ✓ Particle ✓ Nanocomposites	Elastic properties of ✓ Interphase
Two-scale homogenization (Section A.3.3)	Elastic properties of ✓ Matrix ✓ Particle ✓ Interphase Filler morphology ✓ Filler location ✓ Filler radii	Elastic properties of ✓ Multiparticulate system (including 10, 20, and 30 nanoparticles)

Table A.2. Chemical composition of crosslinked epoxy and crosslinked epoxy/SiC nanocomposites in MD simulation.

System	SiC nanoparticle radius (Å)	No. of EPON862® resin molecule	No. of TETA® hardener molecule	Cubic cell length (Å)	Target density (g/cm ³)	Target volume fraction (%)
Epx06	-	18	6	21.22	1.20	-
Epx12		36	12	26.73		
Epx18		54	18	30.6		
Epx30		90	30	36.28		
Epx06 + 5.18 Å SiC	5.18	18	6	21.57		5.8
Epx18 + 7.54 Å SiC	7.54	54	18	31.40		
Epx30 + 9.00 Å SiC	9.00	90	30	37.32		
Epx42 + 10.00 Å SiC	10.00	126	42	41.73		

Table A.3. Determination of interphase thickness from the result of a previous study [48] where r_p and t_{int} denote the nanoparticulate radius of SiC and the corresponding interphase thickness, respectively.

System	r_p [Å]	t_{int} [Å]	t_{int}/r_p	Used t_{int}/r_p in this study
Epx06 + 5.18 Å SiC	5.18	4.48	0.865	0.840
Epx20 + 7.80 Å SiC	7.80	5.90	0.756	
Epx30 + 9.00 Å SiC	9.00	7.33	0.814	
Epx42 + 10.00 Å SiC	10.00	9.08	0.908	

Table A.4. The proposed algorithm to obtain probability distributions of the elastic properties of the interphase from MD and multi-inclusion results.

- 0. Unknowns:** $x_1 = \text{avg}(\log(E_{\text{int}})), x_2 = \text{std}(\log(E_{\text{int}})), x_3 = \text{avg}(\nu_{\text{int}}), x_4 = \text{std}(\nu_{\text{int}})$
- 1. Initialize:** $k = 0, x_1^{(0)} = \text{avg}(\log(E_{\text{mat}})), x_2^{(0)} = \text{std}(\log(E_{\text{mat}})), x_3^{(0)} = \text{avg}(\nu_{\text{mat}}), x_4^{(0)} = \text{std}(\nu_{\text{mat}})$
- 2. Compare mean and standard deviation of micromechanics and MD.**

$$f_1 = \frac{\text{avg}(\log(E_{\text{comp}}^{\text{micromech}})) - \text{avg}(\log(E_{\text{comp}}^{\text{MD}}))}{\text{avg}(\log(E_{\text{comp}}^{\text{MD}}))}, f_2 = \frac{\text{std}(\log(E_{\text{comp}}^{\text{micromech}})) - \text{std}(\log(E_{\text{comp}}^{\text{MD}}))}{\text{std}(\log(E_{\text{comp}}^{\text{MD}}))},$$

$$f_3 = \frac{\text{avg}(\log(G_{\text{comp}}^{\text{micromech}})) - \text{avg}(\log(G_{\text{comp}}^{\text{MD}}))}{\text{avg}(\log(G_{\text{comp}}^{\text{MD}}))}, f_4 = \frac{\text{std}(\log(G_{\text{comp}}^{\text{micromech}})) - \text{std}(\log(G_{\text{comp}}^{\text{MD}}))}{\text{std}(\log(G_{\text{comp}}^{\text{MD}}))}$$

$$f = \|(f_1, f_2, f_3, f_4)\|$$

IF: $f < e_{\text{tol}}$, THEN: *EXIT*

- 3. Solve the directional bi-section method**

- 3.1. Select direction**

$$j = \text{mod}(k, 4) + 1$$

- 3.2. Obtain $x_j^{(k+1)}$ through the bi-section method for the selected direction**

$$\text{Solve } x_j^{(k+1)} \text{ s.t. } f_j^{(k)}(x_1^{(k)}, \dots, x_j^{(k+1)}, \dots, x_4^{(k)}) < e_{\text{tol}} / 2$$

- 3.3 Update $\mathbf{x}^{(k+1)}$ of other non-selected directions**

$$x_m^{(k+1)} = x_m^{(k)} \text{ where } m \in \{1, 2, 3, 4\} - \{j\}$$

Set $k \leftarrow k + 1$ and GO TO 2.

Table A.5. Statistical parameters (mean, standard deviation, and coefficient of variation) of elastic properties obtained from MD simulation compared with those of other studies. V_f is the volume fraction of the filler.

System	Young's modulus			Shear modulus			No. of repetitive simulation	Researchers
	Average [GPa]	Standard deviation [GPa]	Coefficient of variation	Average [GPa]	Standard deviation [GPa]	Coefficient of variation		
Epx06	3.69	0.41	0.111	1.39	0.15	0.108	32	Current study
Epx12	3.80	0.40	0.105	1.44	0.14	0.097		
Epx18	3.99	0.31	0.078	1.52	0.12	0.079		
Epx30	3.98	0.33	0.083	1.49	0.12	0.081		
Epx06 + 5.18 Å SiC	5.38	0.42	0.078	2.03	0.17	0.085		
Epx18 + 7.54 Å SiC	5.27	0.36	0.069	1.95	0.15	0.076		
Epx30 + 9.00 Å SiC	5.09	0.36	0.071	1.86	0.14	0.074		
Epx42 + 10.00 Å SiC	5.07	0.31	0.062	1.86	0.12	0.066		
Mori-Tanaka	4.37	-	-	1.60	-	-		
Nylon6 + 9.97 Å SiO ₂ ($V_f = 10.0\%$)	4.28	0.70	0.164	1.57	0.28	0.178	5	Yang and Cho [33]
Nylon6 + 9.97 Å SiO ₂ ($V_f = 8.5\%$)	3.62	0.27	0.075	1.32	0.11	0.083		
Nylon6 + 9.97 Å SiO ₂ ($V_f = 7.5\%$)	3.20	0.34	0.106	1.16	0.13	0.112		
Nylon6 + 9.97 Å SiO ₂ ($V_f = 6.5\%$)	3.36	0.09	0.027	1.22	0.03	0.025		
Nylon6 + 9.97 Å SiO ₂ ($V_f = 6.0\%$)	3.10	0.19	0.061	1.12	0.08	0.071		
Epx09 + 6.0 Å Al ₂ O ₃	6.22	0.72	0.115	2.32	0.304	0.131	10	Yu et al. [21]
Epx21 + 7.9 Å Al ₂ O ₃	5.14	0.83	0.162	1.91	0.347	0.182		
Epx30 + 8.9 Å Al ₂ O ₃	4.42	0.46	0.104	1.64	0.186	0.113		
Epx42 + 10.0 Å Al ₂ O ₃	4.00	0.53	0.132	1.47	0.207	0.141		

Table A.6. Statistical parameters (mean, standard deviation, and coefficient of variation) of Young's moduli of matrix and interphase for unit cell system.

System	Matrix					Interphase		
	MD results		Fitted data			Average [GPa]	Standard deviation [GPa]	Coefficient of variation
	Average [GPa]	Standard deviation [GPa]	Average [GPa]	Standard deviation [GPa]	Coefficient of variation			
Epx06	3.69	0.41	3.87	0.41	0.105	-	-	-
Epx12	3.80	0.40		0.38	0.099			
Epx18	3.99	0.31		0.36	0.094			
Epx30	3.98	0.33		0.33	0.084			
Epx06 + 5.18 Å SiC	-	-		0.41	0.107	7.95	0.34	0.043
Epx18 + 7.54 Å SiC				0.38	0.099	7.04	0.34	0.048
Epx30 + 9.00 Å SiC				0.35	0.092	6.60	0.43	0.065
Epx42 + 10.00 Å SiC				0.33	0.085	6.34	0.52	0.082

Table A.7. Homogenized Young's moduli of polydisperse multi-particulate nanocomposite systems that include various numbers of inclusions to determine the proper number of representative volume elements (RVE).

System	No. of inclusions	Volume fraction (%)	Particulate Radius (Å)		Homogenized Young's moduli [GPa]		
			Average	Standard deviation	Average	Standard deviation	Coefficient of variation
MP10	10	5.8	7.54	2.44	5.53	0.227	0.041
MP20	20				5.46	0.147	0.027
MP30	30				5.51	0.132	0.024
Upper bound	1		2.08	-	5.70	-	
Lower bound			12.99		4.92		
Regular system			7.54		5.22		

Table A.8. Influence of propagation of inherent uncertainties of the MD model on the homogenized Young's moduli of polydisperse multi-particulate nanocomposite systems.

System	No. of inclusions	Only geometric uncertainty		Only MD uncertainty		Both uncertainties		
		Average	Variance (Var _{Geo})	Average	Variance (Var _{MD})	Average	Variance	Var _{Geo} + Var _{MD}
MP10	10	5.53	0.0514	5.65	0.0212	5.49	0.0706	0.0726
MP20	20	5.46	0.0217	5.73	0.0107	5.42	0.0312	0.0324
MP30	30	5.51	0.0175	5.21	0.0065	5.47	0.0238	0.0240
Regular system	1	5.22	-	5.22	0.1359	-	-	-

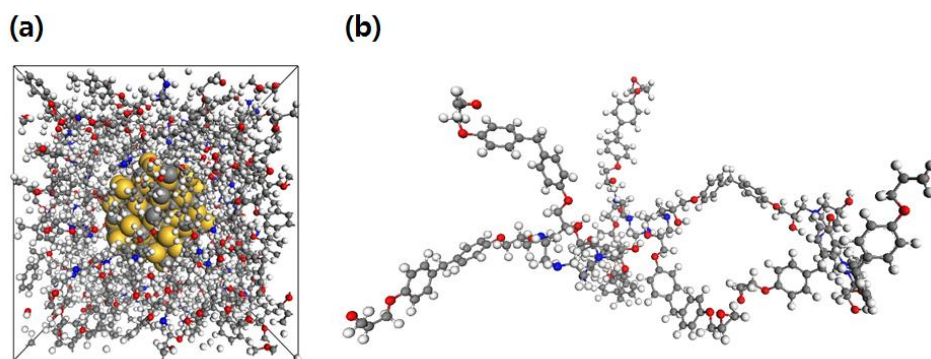


Fig. A.1. Molecular modeling: (a) Polymer nanocomposite unit cell with spherical silicon carbide (SiC) filler, and (b) crosslinked epoxy network (crosslinking ratio, 0.61).

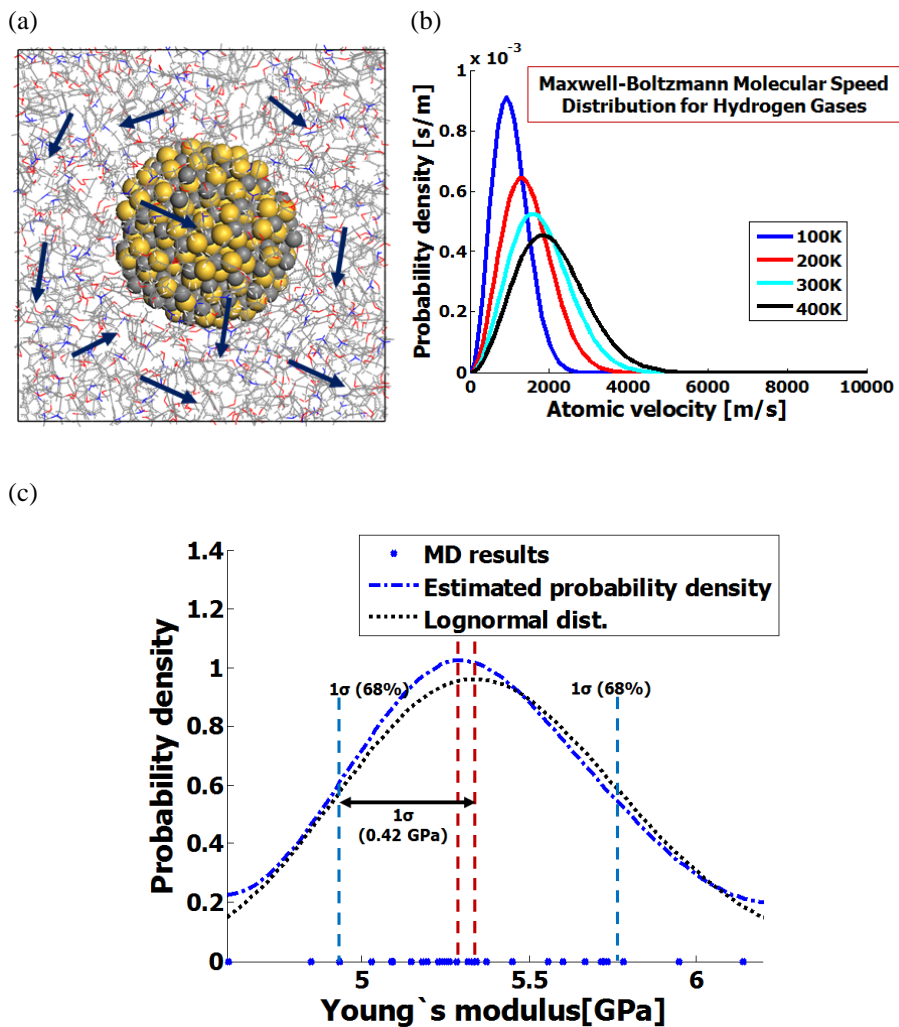


Fig. A.2. Major model uncertainties: (a) uncertainties that stem from chaotic flow of molecules during ensemble averages; (b) randomness of initial ensemble velocity distribution despite identical macroscopic temperature; and (c) lognormal distribution of the obtained elastic properties of polymer nanocomposites including single particles (radius = 5.18 Å).

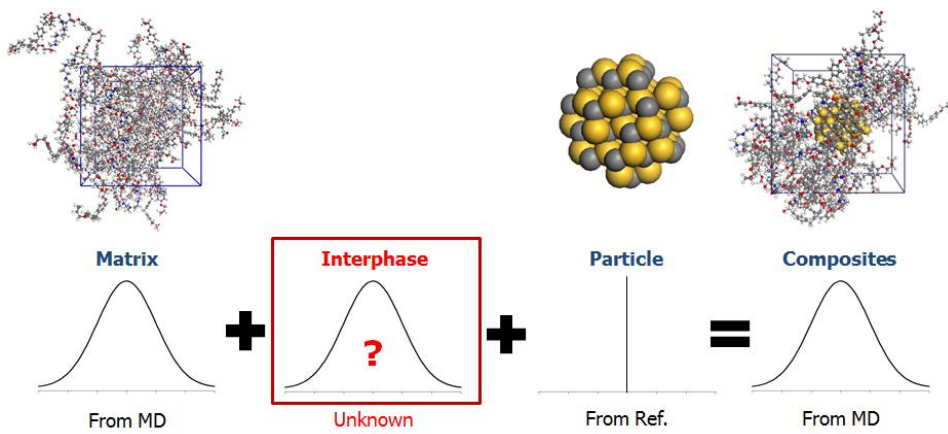


Fig. A.3. Statistical multiscale bridging method that reflects inherent uncertainty of MD model.

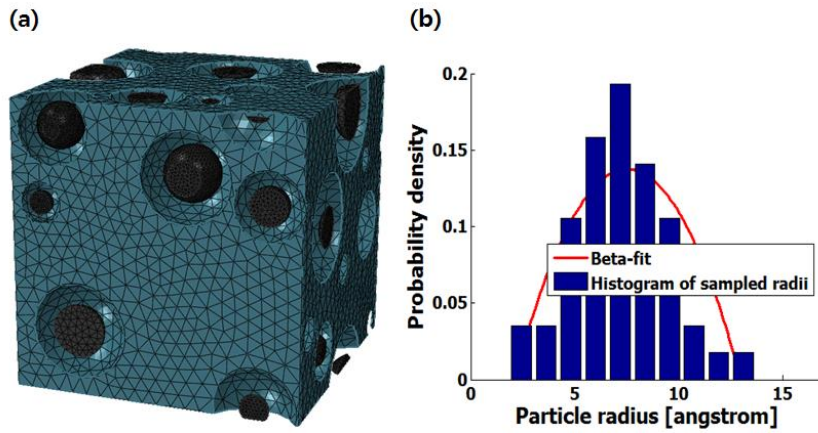


Fig. A.4. Representative volume element (RVE) with 30 nanoparticles and corresponding interphase inside the matrix phase. DIGIMAT[®] was used for modeling CAD geometry of randomly distributed nanoparticles and corresponding interphase. (a) Finite element model (Figure includes mesh configuration of matrix and particle only), and (b) probability density distribution of particle radii.

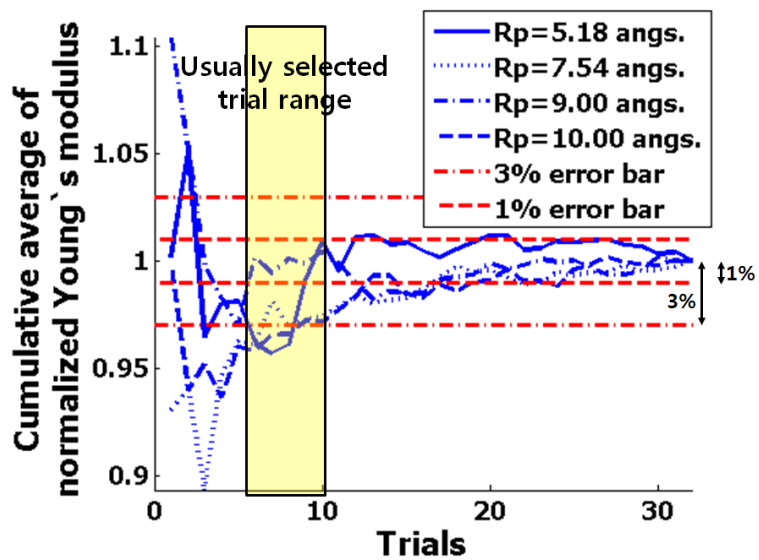


Fig. A.5. Cumulative average of normalized Young's moduli for polymer nanocomposites.

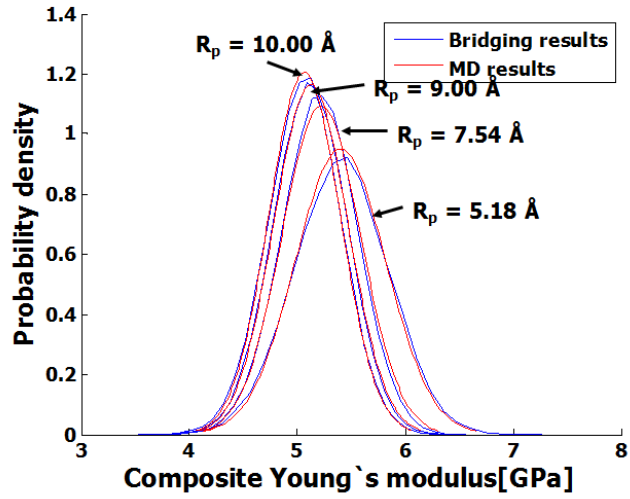


Fig. A.6. Comparison of nanocomposites elastic properties between statistical multiscale bridging method and molecular dynamics simulation to validate the proposed statistical multiscale bridging method.

Serial

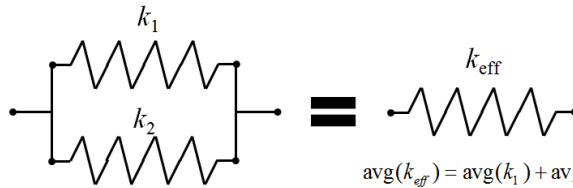
k_1 :log-normal distribution

k_2 :log-normal distribution



$$\text{avg}(k_{eff}) < \left(\frac{1}{\text{avg}(k_1)} + \frac{1}{\text{avg}(k_2)} \right)^{-1}$$

Parallel



$$\text{avg}(k_{eff}) = \text{avg}(k_1) + \text{avg}(k_2)$$

Fig. A.7. Influence of uncertainty in the material properties of each spring on the mean material property of the effective spring element.

APPENDIX B. A MULTISCALE HOMOGENIZATION OF POLYMER NANOCOMPOSITES THAT INCLUDE AGGLOMERATED NANOPARTICLES

B.1. Introduction

In spite of the rapid development of fabrication techniques, the uniform dispersion of the reinforced nanoparticles is still a challenging issue. Non-uniformly distributed nanoparticles due to an increase of non-bond interactions (including van der Waals interactions and electrostatic forces) constituted the nanoparticulate cluster [115-119]. To assess the influence of the clustered particles, simple analytic micromechanical models of composites have been developed [120-122] by considering the cluster as a composite inclusion made up of neat matrix and particles, a concept known as super-inclusion. Simulation results showed that the presence of the clustered particles had a negligible effect on the stress-strain curves of the composites with the same volume fraction as that of the reinforced particles [120]. However, it is still questioned on whether the presence of the clustered nanoparticles has a negligible influence on the stress-strain curves for the nanocomposites, particularly when the interface effect is considered.

The agglomeration of filler particles interrupts the effective penetration and crystallization of the polymer segment in the unoccupied regions [116,123], as well as the consequent effect of confining the nanoparticles [124]. As insufficient penetration of polymer brushes in the interphase zone naturally results in the formation of a vacancy zone in the agglomeration, it is generally believed to

degrade the overall mechanical properties. Nonetheless, there have been very few judicious simulation studies on the molecular level to obtain more information on the agglomeration of nanoparticles and to reveal the associated degradation mechanism of nanocomposites.

To investigate the agglomeration phenomenon of nanoparticles, molecular dynamics (MD) simulation obviously replicates molecular motions and creates a virtual experimental environment with the highest resolution. Since the agglomeration of nanoparticles involves the merging of two neighboring interphase zones, however, a definition of the interphase zone surrounding the nanoparticles on the continuum level is required to determine the concentration and properties of the interphase. In the study reported in this letter, we used MD simulations to explore the mechanism through which the agglomeration of nanoparticles degrades the elastic property. To quantitatively evaluate the degradation of a nanocomposite in terms of the percolated interphase zone, the Young's modulus of the percolated interphase zone is defined as a function of the degree of agglomeration through multiscale modeling, which combines the MD simulation results with the equivalent three-phase finite-element (FE)-based homogenization method. In addition, we examined the contribution of the non-bond interaction energy between agglomerated particles to the total deformation energy of the nanocomposite.

The concept of the equivalent cluster is introduced to describe the clustered nanoparticles, which accounts for the influence of the percolated interphase zone as shown in Fig. B.1. The multiscale homogenization schematic is proposed for the inverse estimation of the homogenized elastic properties of the equivalent cluster. With the use of the proposed multiscale homogenization schematic, the

homogenized elastic properties of the equivalent cluster are determined, and fitted as a function of the radius of the cluster, at a fixed volume fraction and radii of nanoparticles, where the cluster of nanoparticles is simplified as the spherical inclusion with homogeneous and isotropic elastic properties. Finally, it is verified that the equivalent cluster model is applicable to the polymeric nanocomposites that include a number of clusters.

To the best of our knowledge, published multiscale models of polymeric nanocomposites that include clusters of nanoparticles have not accounted for the influence of the interphase percolation. Due to the difficulty in achieving the precise control, the experimental quantification of the influence of the clustered nanoparticles on the degradation of homogenized elastic properties is impossible. Therefore, the proposed multiscale modeling strategy of the polymeric nanocomposites that includes clusters of nanoparticles can act as the foundation of the multiscale modeling.

B.2. Characterization of the Percolated Interphase Zone near the Agglomerated Nanofillers in Polymer Nanocomposites

B.2.1. Molecular modeling and simulation results

To investigate the correlation between the interparticulate distance of two neighboring nanoparticles and the resulting elastic modulus of the nanocomposite, we set up 12 different nanocomposite unit cells with different interparticulate distances (d), as shown in Tables B.1 and B.2. The filler radius (r_p) and volume fraction (V_f) were fixed at 9 Å and 3%, respectively, for each system in Table B.1, while they were fixed at 5.18 Å and 3% for each system in Table B.2. The

nanocomposite molecular model consisted of two aligned spherical silicon carbide (SiC) nanoparticles and an isotactic polypropylene (PP) matrix composed of 50 repeating monomer units. A commercial MD simulation package, Materials Studio 5.5 (Accelrys[®] Inc., now BIOVIA, USA) was used to construct molecular unit cell models in this study [57]. Through the use of an amorphous cell construction module in the Materials Studio 5.5 package, 12 different nanocomposite unit cells were constructed as amorphous unit cells, as listed in Tables B.1 and B.2. In Table B.1, the entire system (approximately 20,000 atoms) was contained within an area of $46.6908 \times 46.6908 \text{ \AA}^2$ and length of 93.3817 \AA , as shown in Fig. B.2(a), while the entire system (approximately 4,000 atoms) in Table B.2 was contained within an area of $26.8732 \times 26.8732 \text{ \AA}^2$ and length of 53.7463 \AA . Periodic boundary conditions were used in all directions. Based on data reported in the literature, the target density of the employed systems was set to $0.8 \text{ g}\cdot\text{cm}^{-3}$ [126]. After the initial construction of the unit cell system, the conjugate gradient method with the energy deviation convergence cutoff of $0.1 \text{ kcal}\cdot\text{mol}^{-1}\cdot\text{\AA}^{-1}$ was used to minimize the potential energy. Upon completion of the construction of each nanocomposite system, relaxation procedures were applied. In order to relax the unit cells at the desired temperature and pressure, isothermal ensemble (*NVT*) simulations at 200 K and isothermal–isobaric ensemble (*NPT*) simulation at the same temperature and at 1 atm were implemented for 700 ps and 5 ns, respectively. Here, *N* is the number of atoms in the unit cell, and *V*, *T*, and *P* are the volume, temperature, and pressure of unit cell, respectively. During the relaxation procedure, Andersen thermostat (in *NVT*) and Berendsen barostat (in *NVT* and *NPT*) are employed. The polymer-consistent force field (PCFF) was employed [100,126] to describe all the inter- and

intra-atomic interactions. For efficient calculation of the non-bonded interaction energy (the sum of van der Waals and Coulombic interaction energies), an atom-based cut-off method with a cut-off distance of 9.5 Å was applied and the distance-dependent dielectric method was used for the Coulombic interactions.

In Table B.1 and B.2, HNR and LNR are abbreviation of “High Nanoparticulate Radius” and “Small Nanoparticulate Radius”, respectively. An equivalent FE discretized model of the nanocomposite consisting of nanoparticles (red), an interphase (green), and a matrix zone (light kaki) is shown in Fig. B.2(b). In Table B.1 and B.2, E_L^{comp} , E^{int} , V_f^{int} , δ_{overlap} , and t_{int} are the longitudinal elastic modulus of the nanocomposite, modulus of the interphase, volume fraction of the interphase, overlapping density, and interphase thickness, respectively. The overlapping density is defined as

$$\delta_{\text{overlap}} = \frac{V_{\text{overlap}}^{\text{int}}}{V_{\text{total}}^{\text{int}}} \leq 1 \quad (\text{B.1})$$

where $V_{\text{overlap}}^{\text{int}}$ is the overlapping volume of the interphase caused by nanoparticle agglomeration, and $V_{\text{total}}^{\text{int}}$ is the total volume of the interphase. To determine the overlapping thickness, the thickness of the interphase should first be determined.

The Parrinello–Rahman strain fluctuation method [99] was chosen to calculate the elastic moduli of the employed systems, through the use of a commercial MD simulation package, Materials Studio 5.5 (Accelrys® Inc., now BIOVIA, USA). More procedures that are detailed are introduced in Chapter 2. To avoid statistical noise of inherent uncertainties in the MD model, the average longitudinal elastic modulus E_L^{comp} was obtained from six measurements of the same molecular structure with different initial velocity distributions of atoms [16,102,111].

The values of the longitudinal elastic modulus along the aligned direction of SiC nanoparticles are shown in Tables B.1 and B.2. For high particulate radius systems (Table B.1), when the interparticulate gap between fillers (d) is larger than 10.7 \AA , the modulus does not show a considerable dependence on the gap; however, a drop of nearly 20% in the modulus is observed when the gap is smaller than the critical threshold, below 10 \AA . Meanwhile, the elastic modulus shows less dependence on the gap for low particulate radius systems (Table B.2); a drop of nearly 12–15% in the modulus is observed when the gap decreases. Despite different particulate radii, the dependency of the elastic modulus on the gap is clearly observed. However, the degree of dropdown of elastic properties is dependent on the reinforced particulate radii because the formation of an interphase zone is critically dependent on the particulate curvature and non-bond interaction between polymer chain and fillers [16,48,111,127]. As the filler radius increases, the intercalation of the polymer chain becomes more difficult at a fixed interparticulate gap between neighboring nanoparticles. This difficulty in the intercalation of the polymer appears to be the main reason there is a direct dependency on the filler size. Such degradation is mainly attributed to insufficient penetration of the polymer brush in the interparticulate domain and the reduced volume fraction of the interphase zone surrounding the nanoparticles. Therefore, characterization of the degradation of nanocomposites by the agglomeration in terms of the interphase zone requires an equivalent continuum model that incorporates a three-phase microstructure consisting of the nanoparticles, interphase, and matrix, as shown in Fig. B.2(b). Microstructural modeling including an interphase layer has been widely developed to take into consideration the significant interfacial nature of the mechanical and

conductive behaviors [13,78,127-130]. Since insufficient intercalation of matrix molecules leaves a region of vacancies inside the interphase zone, it is assumed that the agglomeration of nanoparticles involves a decrease in not only the volume concentration but also the elastic modulus of the interphase zone.

B.2.2. Multiscale homogenization modeling and verification

Assuming that the thickness of the interphase zone is not affected by the agglomeration, the decrease in interphase volume fraction by the agglomeration is naturally accounted for by forming a continuum volume element, as shown in Fig. B.2(b). In order to quantify the degradation of the interphase elastic property, we adopted the inverse algorithm to obtain both the elastic modulus and thickness of the interphase zone using a two-scale homogenization method and the MD results [88,109,110]. More details on the two-scale homogenization are introduced in Appendix A. In this study, 2nd order tetra (tetra10) elements are employed to conduct FE analysis (about the 100,000 number of elements for each FE model), and software MSC Nastran[®] is employed to construct mesh configuration [131]. Computational homogenization analysis is performed based on our in-house FE code. Details of the mathematical formula and finite-element discretization are found in Ref. 88. Since the elastic properties of nanocomposites are determined by MD simulation, the unknown property of the interphase can be numerically obtained. We adopted the most up-to-date second-moment interphase strain-energy-based algorithm proposed by Choi et al.[48] to simultaneously estimate the thickness and moduli of the interphase. The key idea of this method is to determine the optimum interphase properties that satisfy the following convergence criteria

when a small longitudinal strain of 0.3% is applied to both the MD simulation cell and the FE model:

$$f_1(E_{\text{int}}, G_{\text{int}}, t_{\text{int}}) < 10^{-10}, f_2(E_{\text{int}}, G_{\text{int}}, t_{\text{int}}) < 10^{-4} \quad (\text{B.2a})$$

$$f_1 = \sqrt{\left(\frac{E_{\text{comp}}^{\text{MD}} - E_{\text{comp}}^{\text{FE}}}{E_{\text{comp}}^{\text{MD}}}\right)^2 + \left(\frac{G_{\text{comp}}^{\text{MD}} - G_{\text{comp}}^{\text{FE}}}{G_{\text{comp}}^{\text{MD}}}\right)^2} \quad (\text{B.2b})$$

$$f_2 = \left| \frac{U_{\text{int}}^{\text{MD}} - U_{\text{int}}^{\text{FE}}}{U_{\text{int}}^{\text{MD}}} \right| \quad (\text{B.2c})$$

where U_{int} is the deformation energy of the interphase zone and the subscripted identifier of U (e.g., “int”) indicates the model from which the deformation energy is calculated.

The elastic properties of the interphase and the corresponding thickness obtained from Eq. (B.2a–c) are shown in Table B.1 and B.2. Reflecting the drop in the elastic modulus of the nanocomposite with decreasing interparticulate gap, the elastic properties of the interphase zone show a prominent fall as the of interparticulate distance decreases. The main reason for the degradation of the interphase elastic properties is the presence of the vacancy zone, which serves as a defect of the interphase. To verify the hypothesis of insufficient permeation of PP molecules into the gallery zone between two nanoparticles, we compared the density profiles of slab A across the overlapping region B in Fig. B.3(a) of the system HNR. II before and after the application of longitudinal tension. As shown in Fig. B.3(b), the transverse coordinate of 20 Å corresponds to the gallery between the two nanoparticles denoted as C. The density near the gallery zone before tensile loading was less than 0.2 g·cm⁻³, which is only 25% of the value for pure neat PP, owing to the nanoscale confinement of molecules in the gallery zone between

neighboring nanoparticles. Polymer chains are unable to permeate the nanometer-sized vacancy zone between nanoparticles because the potential barrier, which originates from high repulsive forces below the equilibrium distance, is too high. After applying tensile loading, which increased the interparticulate distance, the density of PP in region C slightly increased while that in region B (right in the vicinity of region C) decreased. This change indicates that the molecules at B, which had not initially permeated the vacancy zone, moved to the region C after the tensile deformation was applied. Therefore, it can be concluded that the insufficient permeation of matrix molecules into the agglomeration of nanoparticles acts as a vacancy defect inside the interphase zone.

In order to construct a percolated interphase model that describes the degradation of the nanocomposite, the elastic modulus of the interphase zone must be expressed in terms of the degree of agglomeration. Since the agglomeration of nanoparticles involves an increase in the overlapping density defined in Eq. (B.3) as well as a decrease in the interphase properties, the percolated interphase model is defined through exponentially decayed fitting of interphase Young's modulus data listed in Table B.1, as described by the following equation:

$$E_{\text{int}} = \alpha e^{\beta(\delta_{\text{overlap}} - \gamma)} + E_{\text{mat}} \quad (\text{B.3})$$

where $\alpha = 2.7208$ GPa, $\beta = -0.0393$, and $\gamma = 2.1140$. For smaller nanoparticulate radius systems (Table B.2), $\alpha = 1.8795$ GPa, $\beta = -0.0331$, and $\gamma = 5.4817$. At $\delta_{\text{overlap}}=0\%$, this model agrees with the well-dispersed state data ($E_{\text{int}} = 5.1$ GPa) listed in Table B.1. The $E_{\text{int}}/E_{\text{mat}}$ ratios are 3.04 ($r_p = 9.00 \text{ \AA}$), and 2.38 ($r_p = 5.18 \text{ \AA}$) which are similar to the values reported in the literature (1.44–4.62) for thermoplastic polymer nanocomposites with sub-nanometer-sized particles ($r_p = 5\text{--}$

10 Å) [16]. Using the percolated interphase model defined in Eq. (B.3), the Young's modulus of the nanocomposite was obtained from the FE-based homogenization method for different values of interparticulate distance. Note that the exponentially decayed fitting of the interphase Young's modulus as a function of the overlapping density is appropriate for predicting the elastic properties of the nanocomposite, as shown in Fig. B.4(c) and (d). In other words, the global response of the nanocomposite can be accurately obtained through the proposed interphase percolation model.

The proposed percolated interphase model is also applicable to the multiparticulate system (Fig. B.5). In this study, the multiparticulate nanocomposite systems that include four agglomerated nanoparticles were considered. The coordinates of the four SiC nanoparticles are listed in Table B.3. In Table B.3, MP is the abbreviation for "multiparticulate." In the MP I system, each particulate radius is fixed at 9.00 Å, and the unit cell volume is 48^3 Å^3 ($V_f = 11\%$). The occupied interphase volume and overlapping interphase volume of the employed system are $69,187 \text{ Å}^3$ and $43,093 \text{ Å}^3$ ($\delta_{\text{overlap}} = 62\%$), respectively. Using Eq. (B.3), the corresponding interphase elastic property E^{int} of this overlapping density is 1.95 GPa. Specifically, it is implemented in the C matrix of the interphase when the homogenized elastic stiffness matrix is computed. To obtain the homogenized elastic properties of the multiparticulate system, a periodic boundary condition is applied. The MP II system is composed of four nanoparticles ($r_p = 5.18 \text{ Å}$), and the unit cell volume is 31.90^3 Å^3 ($V_f = 7.17\%$). The occupied interphase volume and overlapping interphase volume of the employed system are $18,394 \text{ Å}^3$ and $11,500 \text{ Å}^3$ ($\delta_{\text{overlap}} = 63\%$), respectively. Using Eq. (B.3), the

corresponding interphase elastic property E^{int} of this overlapping density is 1.97 GPa. In order to compare the isotropic elastic properties, Hill's model for polycrystalline structures [132] was applied to the homogenized elastic modulus of the nanocomposite base cell.

As shown in Table B.4, the multiscale homogenization method using the proposed interphase percolation model (present model) provided accurate elastic moduli close to the MD simulation results. Additionally, we repeated the calculations using a multiparticulate model without taking into consideration the interfacial property degradation ($E^{\text{int}} = 5.1$ GPa about MP I system, and $E^{\text{int}} = 4.0$ GPa about MP II system). When degradation of the interphase by the agglomeration is not considered in the same multiparticulate system, however, the results are about two times higher than the MD simulation results, which is not an acceptable prediction. Therefore, the proposed interphase percolation model is required to analyze the multiparticulate system.

Finally, the local field fluctuation caused by the two approaching nanoparticles was analyzed for HNR. I that is the system that has the smallest interparticulate distance. Contrary to belief, the decrease in interparticulate distance that accompanies the agglomeration involves local field perturbations. For organic nanoparticles composed of partially charged atoms embedded in typical engineering polymers, the direct non-bond interactions, namely the van der Waals and Coulombic forces between the aggregating particles, grow more significant with agglomeration. Therefore, the local stress field of the agglomeration becomes remarkably increased because according to the classical virial theorem, the non-bond interactions between neighboring nanoparticles can act as stiff springs

[133,134]. The interparticulate energy consists of the van der Waals and Coulombic interaction, as described by $U_{A-B} = \sum_{I \in A} \sum_{J \in B} U_{\text{vdW}}^{IJ} + U_{\text{elec}}^{IJ}$, where A and B represent the two nanoparticles, and I and J correspond to two interacting atoms in each nanoparticle. In the elastic deformation condition of the nanocomposite, the interparticulate interaction energy directly contributes to the overall strain energy, which is proportional to the elastic modulus of the nanocomposite, $U_{\text{composite}} = E_L \varepsilon_L^2 V / 2$. Therefore, we defined the relative contribution of the interparticulate energy to the total deformation energy of mechanically loaded nanocomposites as $U_{A-B} / U_{\text{composite}}$. At a strain of 3%, the contribution of interparticulate interaction to the total strain energy of HNR. I is 0.328% ($= 2.73 \times 10^{-21} \text{J} / 8.32 \times 10^{-19} \text{J}$), showing that interparticular interaction of closely interacting SiC nanoparticles is not a dominant factor in determining the elastic modulus of a polymer nanocomposite consisting of agglomerates. Therefore, additional consideration of the filler–filler interaction by incorporating a fictitious strain field or elasticity is not required in equivalent continuum modeling of agglomerated nanocomposite particles.

B.3. Homogenization Analysis of Polymeric Nanocomposites Containing Nanoparticulate Clusters

B.3.1. Models and methods

B.3.1.1. Preparation of finite element unit cells

To assess the existence of a possible influence of the clustered nanoparticles on the degradation of homogenized elastic properties, the clustered nanoparticles were placed at the center of the unit cell, and were close-packed as shown in Fig. B.6.

We set up four different nanocomposite unit cells containing different numbers of clustered nanoparticles (4, 10, 18, and 30). The filler radius (r_p), and volume fraction (V_f) were fixed at 9Å, and 3%, respectively. We conducted CAD modeling using the DIGIMAT[®] software [107], which is a package used for multiscale modeling and simulation (Fig. B.6). For the finite element modeling, ABAQUS[®] was employed to construct the mesh configuration (using approximately the 40,000-100,000 elements for each finite element models) with 2nd order tetrahedral (tetra10) elements [135]. For the preprocessing of the CAD modeling in DIGIMAT[®], the coordinates of the clustered nanoparticles were determined using our in-house code.

A newly developed multiscale schematic is proposed to determine the coordinates of the clustered nanoparticles as shown in Fig. B.7. For the given r_p and n_p of nanoparticles, the coordinates of the clustered nanoparticles can be determined using the proposed schematic. When the nanoparticles are agglomerated and clustered, there exists an unavoidable gap between them due to the high repulsive forces developed when the inter-distance falls below the critical minimum distance, denoted as $(d_{\min})_{\text{criteria}}$. The minimum distance between nanoparticles is determined to be approximately 2Å using molecular dynamics simulations as shown in Fig. B.8. For the molecular modeling and molecular dynamics simulations, we employed Materials Studio 5.5 (Accelrys[®] Inc., now BIOVIA, USA) [57], and the polymer-consistent force field (PCFF) was employed to describe all the inter- and intra-atomic interactions [100,126]. Initially, a radius of cluster was assumed to be equal to:

$$(r_c)_{\text{guess}} = r_p \left(n_p \cdot 3\sqrt{2} \cdot \pi^{-1} \right)^{1/3} \quad (\text{B.4})$$

where the total volume of nanoparticles was assumed to be the same to that of the effective cluster. At each trial, the coordinates of the nanoparticles were generated, and the minimum distance criteria were checked. Due to the existence of the non-particulate cluster domain, (e.g., percolated interphase zone, gallery zone, and neat matrix), the actual radius of the effective cluster is larger than the initially determined value. If the assumed radius of the effective cluster is regarded as infeasible, in spite of the hundreds of trials, the radius of the effective cluster updated with an increasing increment of 1%. If the feasible radius of the effective cluster was attained, the coordinates of the clustered nanoparticles were stored, and were subsequently employed for the CAD modeling using DIGIMAT[®]. During the finite element modeling of the polymeric nanocomposites including the clustered nanoparticles, the percolated interphase zone was considered.

B.3.1.2. Multiscale modeling of equivalent cluster

For the purpose of an efficient description of the clustered nanoparticles, we proposed equivalent cluster-based homogenization approach, as shown in Fig. B.9. In this approach, the representation of the clustered nanoparticles was simplified in the form of an equivalent cluster, that is, the minimum spherical domain to include the clustered nanoparticles. The radius of the equivalent cluster is determined as indicated by the proposed schematics (Fig. B.7). For the 9\AA of the nanoparticulate radius, the radius of the equivalent cluster can be determined as a function of the number of clustered nanoparticles as shown in Fig. B.10. It is shown that the coefficient of variations (CoVs) of the radius of the equivalent cluster are less than 2%, which indicates that the radius of the equivalent cluster can be determined with

negligible fluctuation.

Software MSC Nastran[®] was employed to construct the mesh configuration (approximately 10,000 elements for equivalent cluster-based models). Computational homogenization analysis was performed using our FE code. The unknown elastic properties of the equivalent cluster can be numerically obtained, in such a way that, the unit cell shows the same homogenized elastic behavior as the cell that included all the nanoparticles (i.e., “direct computation”). In other words, the following convergence criteria were solved in order to determine the elastic properties of the equivalent cluster (E_{cluster} and G_{cluster}):

$$f_{\text{cluster}}(E_{\text{cluster}}, G_{\text{cluster}}) = \left\| (f_E, f_G) \right\| < 10^{-10} \quad (\text{B.5})$$

$$f_E = \frac{E_{\text{equi}}^H(E_{\text{cluster}}, G_{\text{cluster}}) - E_{\text{direct}}^H}{E_{\text{direct}}^H}, f_G = \frac{G_{\text{equi}}^H(E_{\text{cluster}}, G_{\text{cluster}}) - G_{\text{direct}}^H}{G_{\text{direct}}^H} \quad (\text{B.6})$$

where E_{equi}^H , and G_{equi}^H are the respective Young’s and shear moduli obtained from the equivalent cluster-based homogenization approach, and E_{direct}^H , and G_{direct}^H , are the equivalent moduli obtained from the direct computation with the total number of nanoparticles.

B.3.2. Homogenization results of polymeric nanocomposites unit cells including single clusters of nanoparticles

The homogenized Young’s moduli decrease remarkably as the number of clustered nanoparticles increases as shown in Table B.5. Intuitively, the homogenized Young’s moduli of polymeric nanocomposites are clearly related to the volume fraction and elastic properties of the interphase zone. As shown in Fig.

B.11 (a), the overall interphase volume fraction clearly decreases as the number of clustered nanoparticles increases. The decrease of the overall interphase volume fraction causes the increase of the overlapping density, which then causes a remarkable decrease of the elastic properties of the interphase zone as shown in Fig. B.11 (b). Therefore, the formation of the clustered nanoparticles causes decreases in the elastic properties of the interphase zone as well as decreases in volume fraction of the interphase.

Fig. B.12 shows that the decrease of the elastic property values of the interphase zone is more critical than that of the decreasing volume fraction. As shown in Fig. B.13, we compare the influence of the interphase percolation model by considering three different types of elastic models where the “w/o degradation” model has constant elastic properties at the interphase regardless of the overlapping densities. As shown in Fig. B.12, the homogenized Young’s moduli range between 2.19-2.27GPa (which correspond to a degradation of 7-11% from unit cells that contained regularly arrayed nanoparticles) when we neglect the effect of degradation of the elastic properties of the interphase zone. However, the degradation of the elastic properties of the interphase zone caused a degradation in the range of 22-26% (1.81-1.90GPa) for unit cells with regularly arrayed nanoparticles. Therefore, the influence of the degradation of the elastic properties of the percolated interphase zone is critical.

Additionally, we investigated the influence of the “linear degradation” model that can be constructed based on the degradation of the homogenized elastic properties. The homogenized Young’s moduli were in the range of 2.09-2.22GPa (exhibiting a 9-15% degradation in the case of unit cells with regularly arrayed

nanoparticles). Due to the slow degradation of the elastic properties at the interphase within the range of an overlapping density below 50%, this “linear degradation” model is not applicable to the description of the homogenized elastic properties of the small-sized cluster of nanoparticles. It is expected that the degradation of the resulting elastic properties obtained from the “linear degradation” model is similar to that of the “Proposed” model for the unit cell with sufficiently high numbers of clustered nanoparticles.

B.3.3. Homogenized elastic model of equivalent cluster and verification

Using the proposed multiscale strategy (Fig. B.9), the effective Young’s moduli of the equivalent cluster (E_{cluster}) are obtained for different numbers of clustered nanoparticles (4, 10, 18, and 30). As shown in Table B.6, the Young’s moduli of the equivalent cluster (E_{cluster}) decrease as its radius (r_{cluster}) increases. The fitting equation takes the following form:

$$E_{\text{cluster}} = \beta_0 e^{-\beta_1 (r_{\text{cluster}}/r_{\text{par}})} + \beta_2 \quad (\text{B.7})$$

where β_0 , β_1 , and β_2 are 86.17GPa, 0.5166, and 2.5688GPa, respectively. An accurate quantification of the limit value could not be attained. However, for a radius less than 50Å, the elastic properties of the equivalent cluster can be determined using the fitted curve, without the need of an additional inverse estimation procedure (Section B.3.1.2).

In order to verify the equivalent cluster approach, we prepared polymeric nanocomposites unit cells that included multi-clusters and free nanoparticles. The homogenized elastic properties are compared in the cases of the direct computation and the equivalent cluster-based homogenization approach, as shown in Fig. B.14.

The obtained homogenized elastic properties are listed in Table B.7. The differences of the homogenization results between the direct computation and the equivalent cluster-based homogenization approach are approximately 1% for the three different types of models. For these employed finite element models, the equivalent cluster-based homogenization approach reduced computational time up to ten times. Therefore, the equivalent cluster-based homogenization approach can replace the direct computational approach. In fact, the direct models involve the complexity of geometry, which causes the failure of mesh generation and needs a large number of elements. To overcome this limitation, the proposed equivalent cluster-based homogenization approach is necessary without loss of computational accuracy.

B.4. Summary of Appendix B

To summarize, we firstly evaluated the longitudinal elastic properties of a nanocomposite with two reinforcements and various interparticulate gaps through MD simulation. The longitudinal elastic properties of the nanocomposite are declined by up to 20% when the reinforced fillers are agglomerated. Insufficient development of the interphase zone near the agglomerated nanoparticles was the main degradation mechanism. To describe the degradation of the modulus by the agglomeration, an interphase percolation model was proposed as a function of the nanoparticles' overlapping density, which was verified through MD simulation. Since locally concentrated agglomeration of nanoparticles is still the most challenging task, the proposed percolation interphase model can be effectively applied to evaluate the performance of a nanocomposite.

Using this interfacial nature near the agglomerated nanofillers, we conducted a multiscale homogenization analysis to predict the elastic properties of polymeric nanocomposites that included agglomerated nanoparticles. We expect that this study can act as the foundation of the multiscale modeling of the polymeric nanocomposites that includes clusters of nanoparticles. The two major aspects of the study are summarized as follows:

- We examined the influence of the clustered nanoparticles on the degradation of the homogenized elastic properties of the polymeric nanocomposite unit cell. Small size of cluster including four nanoparticles causes remarkable decrease of the homogenization elastic properties up to approximately 22%. As a size of cluster increases, the monotonically decreasing tendency of the homogenized elastic property values is clearly investigated above 25%.
- For an efficient description of the polymeric nanocomposite unit cell that includes the clustered nanoparticles, the representation of the clustered nanoparticles was simplified as an equivalent spherical inclusion. The equivalent cluster-based homogenization approach can provide high computational efficiency without loss in computational accuracy.

Table B.1. Longitudinal elastic properties of molecular system and corresponding interphase characteristics for various interparticulate distances ($r_p = 9.00 \text{ \AA}$)

Model	$d \text{ (\AA)}$	E_L^{comp} (GPa)	E^{int} (GPa)	V_f^{int} (%)	δ_{overlap} (%)	t_{int} (\AA)
HNR. I	2.7	2.27	3.6	43.01	17.31	
HNR. II	4.7	2.15	2.9	44.51	13.35	
HNR. III	10.7	2.50	4.3	48.12	4.84	
HNR. IV	16.7	2.55	4.6	50.14	0.62	10.0
HNR. V	22.7	2.52	4.6	50.45	0	
HNR. VI (Well-dispersed)	28.7	2.61	5.1	50.45	0	
Polypropylene [126]	-	1.68	-	-	-	-
Silicon carbide [48]	-	451.6	-	-	-	-

Table B.2. Longitudinal elastic properties of the molecular system and the corresponding interphase characteristics for various interparticulate distances ($r_p = 5.18 \text{ \AA}$)

Model	d (\AA)	E_L^{comp} (GPa)	E^{int} (GPa)	V_f^{int} (%)	δ_{overlap} (%)	t_{int} (\AA)
LNR. I	2.51	2.38	3.3	61.94	61.94	
LNR. II	3.51	2.31	3.0	63.36	63.36	
LNR. III	6.51	2.41	3.1	67.00	67.00	
LNR. IV	10.51	2.80	4.2	70.82	70.82	7.0
LNR. V	12.51	2.67	3.7	71.69	71.69	
LNR. VI (Well-dispersed)	16.51	2.75	4.0	72.00	72.00	

Table B.3. Centroids of each particle in the multiparticulate nanocomposite system.

Par. id	MP I			MP II		
	x (Å)	y (Å)	z (Å)	x (Å)	y (Å)	z (Å)
1	15.44	30.49	10.29	15.44	30.49	10.29
2	21.58	3.99	8.34	21.58	3.99	8.34
3	32.22	21.19	9.36	32.22	21.19	9.36
4	20.02	15.56	24.55	20.02	15.56	24.55

Table B.4. Elastic moduli of the multiparticulate nanocomposite obtained using various approaches.

Model	MPI		MP II	
	<i>E</i> (GPa)	<i>G</i> (GPa)	<i>E</i> (GPa)	<i>G</i> (GPa)
MD	2.55 ± 0.19	0.98 ± 0.09	2.36 ± 0.26	0.84 ± 0.09
Present work	2.83	1.07	2.56	0.95
Model w/o interphase property degradation	4.88	1.84	3.80	1.40

Table B.5. Homogenization results of polymeric nanocomposites unit cell including single cluster of nanoparticles

# of clustered nanoparticles	E_{comp} (GPa)	E_{int} (GPa)	V_f^{int} (%)
1 (regular array)	2.448	6.56	17.54
4	1.897	2.23	14.04
10	1.831	1.92	13.34
18	1.822	1.81	12.78
30	1.815	1.74	11.95

Table B.6. Geometry and elastic properties of equivalent clusters

# of clustered nanoparticles	Cell size (Å)	Geometry of cluster		Young's modulus of cluster [GPa]
		Radius (Å)	Volume fraction (%)	
4	74.12	23.29	13.00	3.79
10	100.59	32.11	13.62	2.83
18	122.36	39.78	14.39	2.66
30	145.08	47.29	14.51	2.58

Table B.7. Verification of the equivalent cluster approach

Model id	Direct computation [GPa]	Equivalent cluster approach [GPa]	Deviation (%)
1	1.883	1.904	1.07
2	1.888	1.907	0.97
3	1.886	1.908	1.19

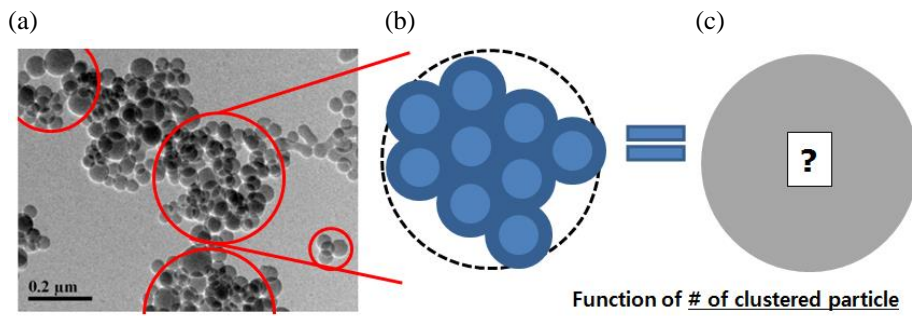


Fig. B.1. Multiscale homogenization strategy of polymeric nanocomposites containing the clustered nanoparticles: (a) TEM image of silica nanocomposites [125], (b) direct modeling, and (c) equivalent cluster modeling

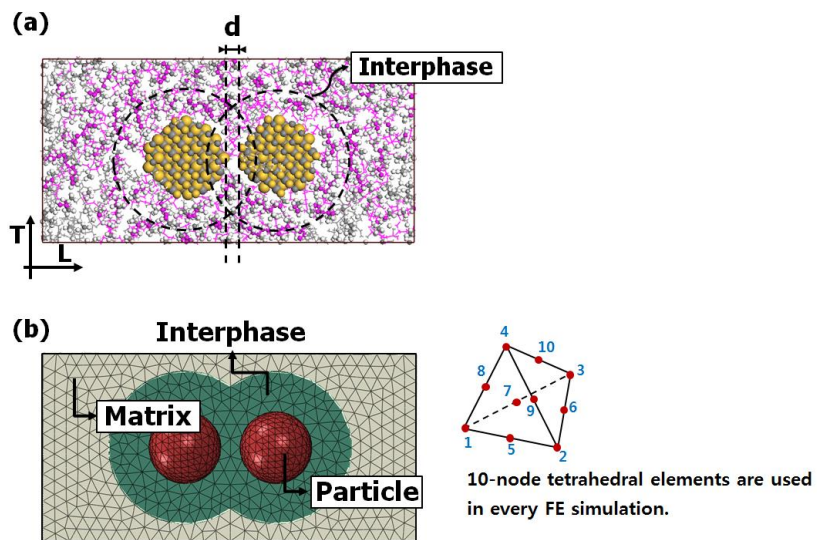


Fig. B.2. Cross section of nanocomposite molecular model and equivalent finite element model (HNR. II): (a) MD model, and (b) Finite element model.

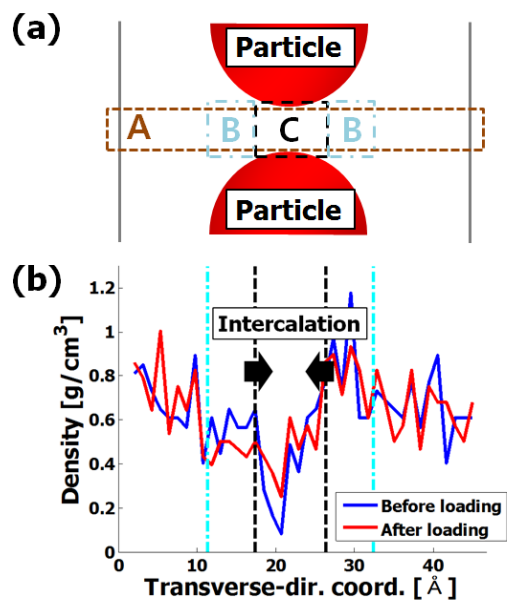


Fig. B.3. (a) Definition of interparticle region for the structural analysis B: overlap region, C: gallery region. (b) Density profile of PP molecules of slab A (HNR. II, $d = 4.7\text{\AA}$).

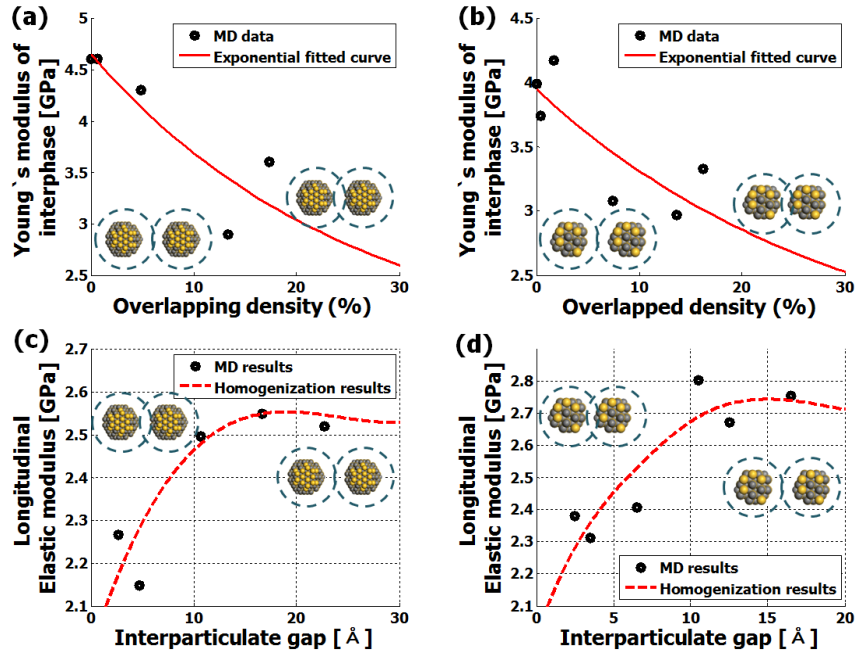


Fig. B.4. The proposed percolation interphase model: interphase Young's modulus when the nanoparticle radius is (a) $r_p=9.00\text{\AA}$, and (b) $r_p=5.18\text{\AA}$, and corresponding longitudinal elastic modulus of nanocomposites predicted from the two-scale homogenization method using the interphase percolation model: (c) $r_p=9.00\text{\AA}$, and (d) $r_p=5.18\text{\AA}$.

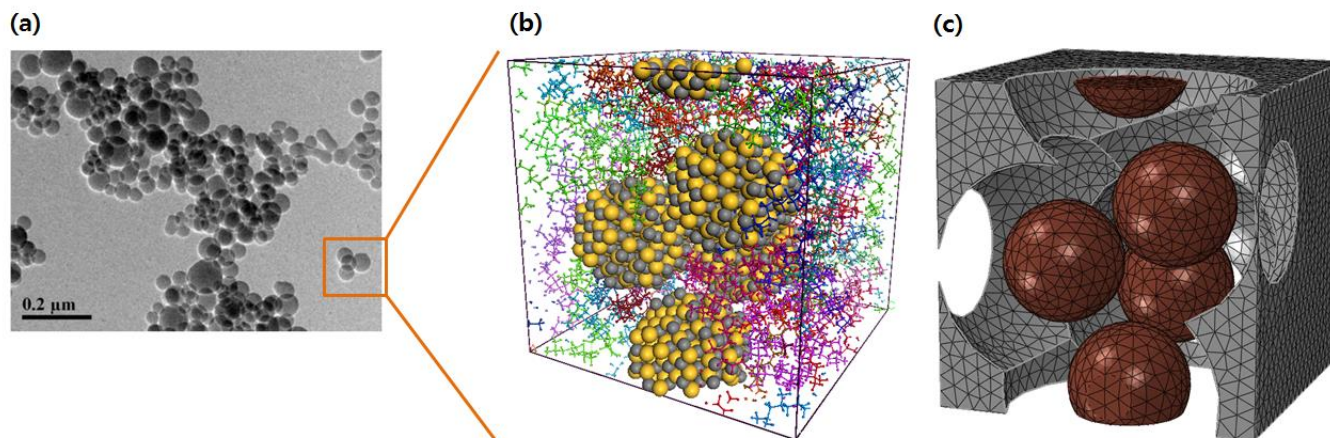


Fig. B.5. A multiparticulate nanocomposite systems that includes four agglomerated nanoparticles: (a) TEM image of silica nanocomposites [125], (b) MD model, and (c) equivalent finite element model (Figure includes mesh configuration of matrix and particle only).

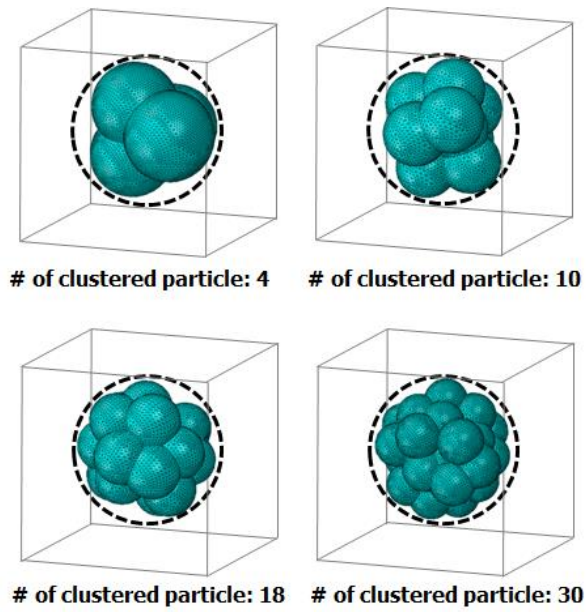


Fig. B.6. Finite element models of a single cluster of nanoparticles for different numbers of nanoparticles (4, 10, 18, and 30) at a fixed volume fraction (3%) and radii (9\AA) of nanoparticles (the schematics include a mesh configuration of the interphase only).

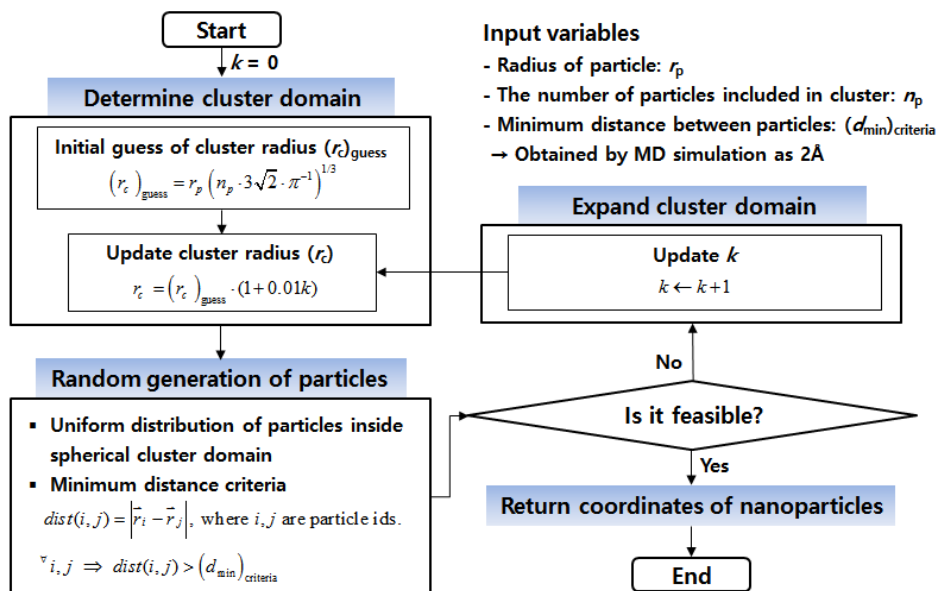


Fig. B.7. Schematics representation of the flow diagram of the processing steps used to determine the coordinates of the clustered nanoparticles

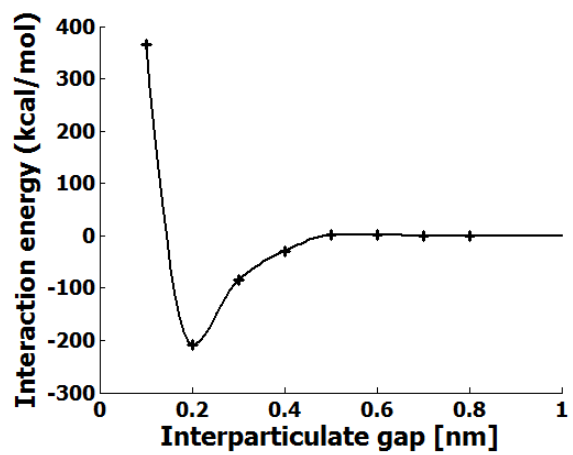


Fig. B.8. Interaction energy between interparticles

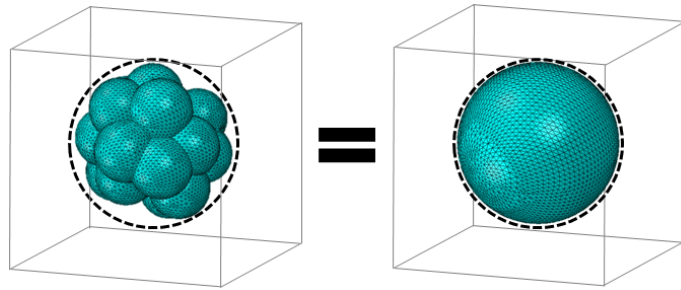


Fig. B.9. The schematics of the equivalent cluster-based homogenization approach

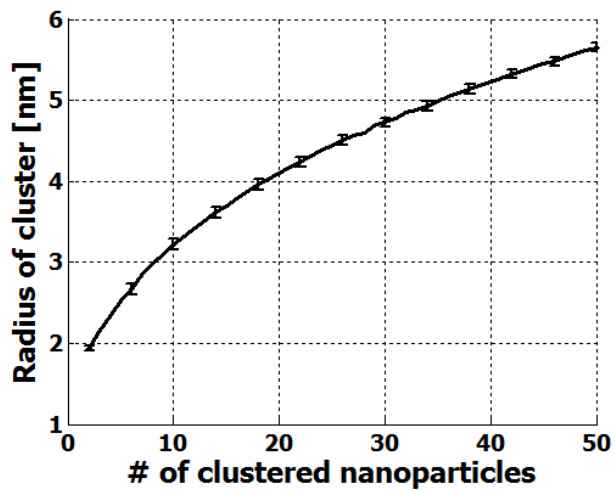


Fig. B.10. Variation of the radius of the cluster with respect to the number of clustered nanoparticles at a nanoparticle radius of 9\AA when nanoparticles are closely-packed

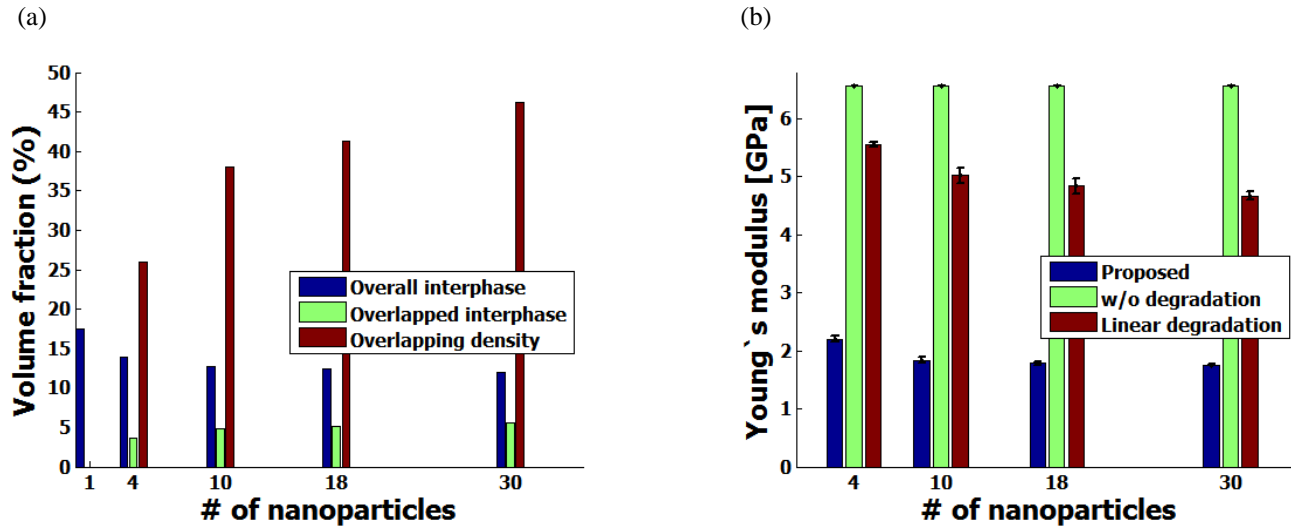
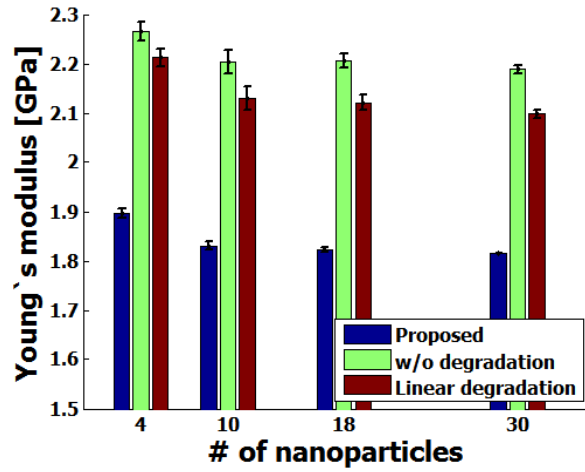


Fig. B.11. Characteristics of percolated interphase zone: (a) volume fraction of interphase and overlapping density, and (b) Young's moduli of percolated interphase zone.

(a)



(b)

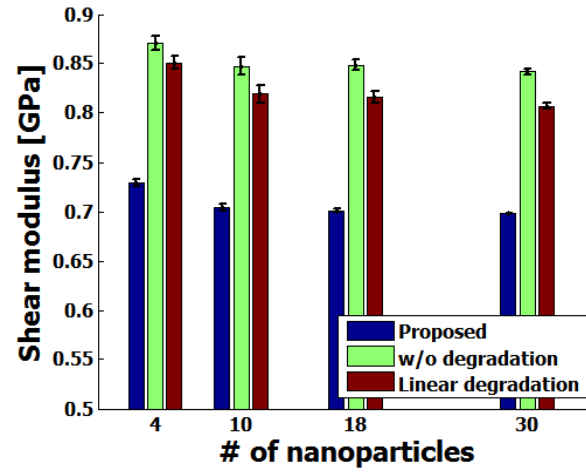


Fig. B.12. Homogenization results of polymeric nanocomposites unit cell including single cluster of nanoparticles: (a) Young's modulus, and (b) shear modulus

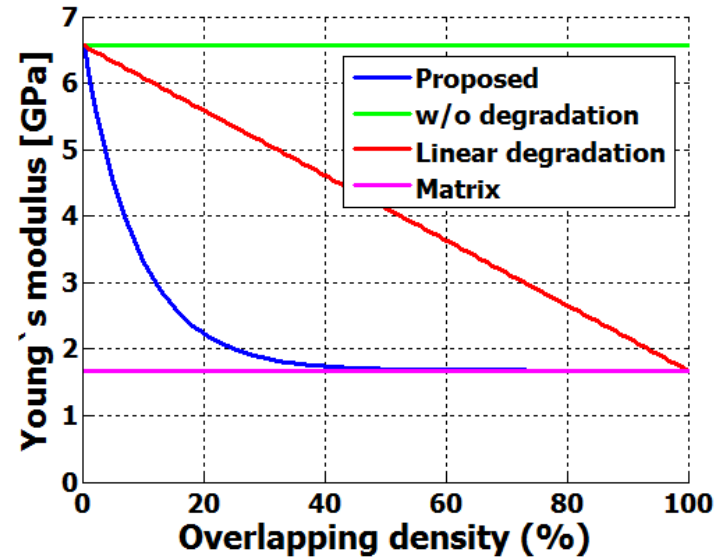


Fig. B.13. Various types of elastic model of overlapped interphase zone

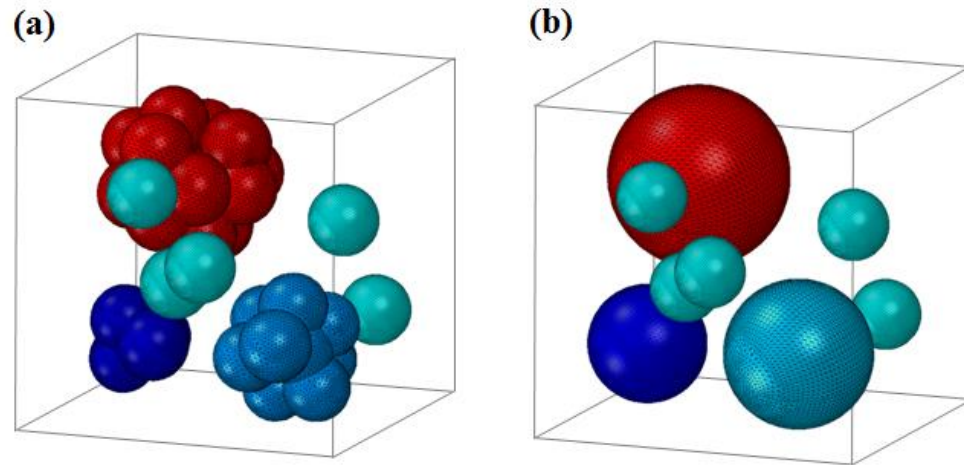


Fig. B.14. Finite element models of polymeric nanocomposites including the clustered nanoparticles: (a) direct computation, and (b) equivalent cluster-based approach (figures include only the mesh configuration of the interphase).

REFERENCES

- [1] RP Wool, KM O'Conner. A theory crack healing in polymers. *J. Appl. Phys.* **1981**, 52, 5953.
- [2] YH Kim, RP Wool. A theory of healing at a polymer-polymer interface. *Macromolecules* **1983**, 16, 1115-1120.
- [3] K Jud, HH Kausch, JG Williams. Fracture mechanics studies of crack healing and welding of polymers. *J. Mater. Sci.* **1981**, 16, 204-210.
- [4] SR White, NR Sottos, PH Geubelle, JS Moore, MR Kessler, SR Sriram, EN Brown, S Viswanathan. Autonomic healing of polymer composites. *Nature* **2001**, 409, 794-797.
- [5] CE Diesendruck, NR Sottos, JS Moore, SR White. Biomimetic Self-Healing. *Angew. Chem. Int. Ed. Engl.* **2015**, 54, 10428-10447.
- [6] BJ Blaiszik, SLB Kramer, SC Olugebefola, JS Moore, NR Sottos, SR White. Self-Healing Polymers and Composites. *Annu. Rev. Mater. Res.* **2010**, 40, 179-211.
- [7] DY Zhu, MZ Rong, MQ Zhang. Self-healing polymeric materials based on microencapsulated healing agents: From design to preparation. *Prog. Polym. Sci.* **2015**, 49-50, 175-220.
- [8] MG Ahangari, A Fereidoon. Micromechanical properties and morphologies of self-healing epoxy nanocomposites with microencapsulated healing agent. *Mater. Chem. Phys.* **2015**, 151, 112-118.
- [9] BRK Blackman, AJ Kinloch, JS Lee, AC Taylor, R Agarwal, G Schueneman, S Sprenger. The fracture and fatigue behaviour of nano-modified epoxy polymers.

- J. Mater. Sci.* **2007**, 42, 7049-7051.
- [10] H-Y Liu, G Wang, Y-W Mai. Cyclic fatigue crack propagation of nanoparticle modified epoxy. *Compos. Sci. Technol.* **2012**, 72, 1530-1538.
- [11] MH Kothmann, R Zeiler, A Rios de Anda, A Brückner, V Altstädt. Fatigue crack propagation behaviour of epoxy resins modified with silica-nanoparticles. *Polymer* **2015**, 60, 157-163.
- [12] J-S Jang, B Bouveret, J Suhr, RF Gibson. Combined numerical/experimental investigation of particle diameter and interphase effects on coefficient of thermal expansion and Young's modulus of SiO₂/Epoxy nanocomposites. *Polym. Compos.* **2012**, 33, 1415-1423.
- [13] S Yu, S Yang, M Cho. Multi-scale modeling of cross-linked epoxy nanocomposites. *Polymer* **2009**, 50, 945-952.
- [14] J Choi, S Yu, S Yang, M Cho. The glass transition and thermoelastic behavior of epoxy based nanocomposites: a molecular dynamics study. *Polymer* **2011**, 52, 5197-5203.
- [15] J-L Tsai, S-H Tzeng. Characterizing mechanical properties of particulate nanocomposites using micromechanical approach. *J. Compos. Mater.* **2008**, 42, 2345-2361.
- [16] S Yang, M Cho. Scale bridging method to characterize mechanical properties of nanoparticle/polymer nanocomposites. *Appl. Phys. Lett.* **2008**, 93, 043111.
- [17] H Liu, LC Brinson. Reinforcing efficiency of nanoparticles: a simple comparison for polymer nanocomposites. *Compos. Sci. Technol.* **2008**, 68, 1502-1512.
- [18] BJ Yang, YY Hwang, HK Lee. Elastoplastic modeling of polymeric

- composites containing randomly located nanoparticles with an interface effect. *Compos. Struct.* **2013**, 99, 123-130.
- [19] M Ganß, BK Satapathy, M Thunga, WR Weidisch, P Pötschke, D Jehnichen. Structural interpretations of deformation and fracture behavior of polypropylene/multi-walled carbon nanotube composites. *Acta. Mater.* **2008**, 56, 2247-2261.
- [20] SP Bao, SC Tjong. Mechanical behaviors of polypropylene/carbon nanotube nanocomposites: the effects of loading rate and temperature. *Mater. Sci. Eng. A* **2008**, 485, 508-516.
- [21] P Barai, GJ Weng. A theory of plasticity for carbon nanotube reinforced composites. *Int. J. Plasticity* **2011**, 27, 539–559.
- [22] J Williams. Particle toughening of polymers by plastic void growth. *Compos. Sci. Technol.* **2010**, 70, 885-891.
- [23] J Williams, B Blackman, H Steininger, K Zuo. Toughening by plastic cavitation around cylindrical particles and fibres. *Compos. Sci. Technol.* **2014**, 103 119-126.
- [24] TH Hsieh, AJ Kinloch, K Masania, AC Taylor, S Sprenger. The mechanisms and mechanics of the toughening of epoxy polymers modified with silica nanoparticles. *Polymer* **2010**, 51, 6284-6294.
- [25] TH Hsieh, AJ Kinloch, K Masania, JS Lee, AC Taylor, S Sprenger. The toughness of epoxy polymers and fibre composites modified with rubber microparticles and silica nanoparticles. *J. Mater. Sci.* **2010**, 45, 1193-1210.
- [26] M Zappalorto, M Salviato, M Quaresimin. A multiscale model to describe nanocomposite fracture toughness enhancement by the plastic yielding of

- nanovoids. *Compos. Sci. Technol.* **2012**, 72, 1683-1691.
- [27] M Salviato, M Zappalorto, M Quaresimin. Plastic shear bands and fracture toughness improvements of nanoparticle filled polymers: a multiscale analytical model. *Compos. Part A Appl. Sci. Manuf.* **2013**, 48, 144-152.
- [28] M Quaresimin, M Salviato, M Zappalorto. A multi-scale and multi-mechanism approach for the fracture toughness assessment of polymer nanocomposites. *Compos. Sci. Technol.* **2014**, 91, 16-21.
- [29] AG Evans, S Williams, PWR Beaumont. On the toughness of particulate filled polymers. *J. Mater. Sci.* **1985**, 20, 3668-3674.
- [30] KM Hamdia, X Zhuang, P He, T Rabczuk. Fracture toughness of polymeric particle nanocomposites: Evaluation of models performance using Bayesian method. *Compos. Sci. Technol.* **2016**, 126, 122-129.
- [31] JK Shang, RO Ritchie. On the particle-size dependence of fatigue-crack propagation thresholds in SiC-particulate-reinforced aluminum-alloy composites: role of crack closure and crack trapping. *Acta. Metall.* **1989**, 37, 2267-2278.
- [32] JR Jones, CA Watkins, SR White, NR Sottos. Self-healing thermoplastic-toughened epoxy. *Polymer* **2015**, 74, 254-261.
- [33] J-P Pascault, RJJ Williams. *Epoxy Polymers*. Weinheim: Wiley-VCH, 2010.
- [34] X Wang, J Jin, M Song. An investigation of the mechanism of graphene toughening epoxy. *Carbon* **2013**, 65, 324-333.
- [35] R Bagheri, BT, Marouf, RA Pearson. Rubber-toughened epoxies: a critical review. *J. Macromol. Sci. Pol. R.* **2009**, 49, 201-225.
- [36] Y Huang, AJ Kinloch. Modelling of the toughening mechanisms in rubber-

- modified epoxy polymers. *J. Mater. Sci.* **1992**, 27, 2763-2769.
- [37] SK Douglass, PWR Beaumont, MF Ashby. A model for the toughness of epoxy-rubber particulate composites. *J. Mater. Sci.* **1980**, 15, 1109-1123.
- [38] BB Johnsen, AJ Kinloch, AC Taylor. Toughness of syndiotactic polystyrene/epoxy polymer blends: microstructure and toughening mechanisms. *Polymer* **2005**, 46, 7352-7369.
- [39] JA Cecere, JE McGrath. Morphology and properties of amine-terminated poly(aryl ether ketone) and poly(aryl ether sulphone) modified epoxy resin systems. *Polym. Chem. Polym. Prepr.* **1986**, 27, 299-301.
- [40] RA Pearson, AF Yee. Toughening mechanisms in thermoplastic-modified epoxies: 1. Modification using poly(phenylene oxide). *Polymer* **1993**, 34, 3658-3670.
- [41] AJ Kinloch, ML Yuen, SD Jenkins. Thermoplastic-toughened epoxy polymers. *J. Mater. Sci.* **1994**, 29, 3781-3790.
- [42] S-E Lee, E Jeong, MY Lee, M-K Lee, Y-S Lee. Improvement of the mechanical and thermal properties of polyethersulfone-modified epoxy composites. *J. Ind. Eng. Chem.* **2016**, 33, 73-79.
- [43] S Zhao, LS Schadler, R Duncan, H Hillbrog, T Auletta. Mechanisms leading to improved mechanical performance in nanoscale alumina filled epoxy. *Compos. Sci. Technol.* **2008**, 68, 2965-2975.
- [44] B Lauke. On the effect of particle size on fracture toughness of polymer composites. *Compos. Sci. Technol.* **2008**, 68, 3365-3372.
- [45] LS Sigl, PA Mataga, BJ Dalgleish, RM Mcmeeking, AG Evans. On the toughness of brittle materials reinforced with a ductile phase. *Acta. Metall.* **1988**,

- 36, 945-953.
- [46] BJ Cardwell, AF Yee. Toughening of epoxies through thermoplastic crack bridging. *J. Mater. Sci.* **1998**, 33, 5473-5484.
- [47] RM Elder, JW Andzelm, TW Sirk. A molecular simulation study of the glass transition of cross-linked poly(dicyclopentadiene) networks. *Chem. Phys. Lett.* **2015**, 637, 103-109.
- [48] J Choi, H Shin, S Yang, M Cho. The Influence of Nanoparticle Size on the Mechanical Properties of Polymer Nanocomposites and the Associated Interphase Region: A Multiscale Approach. *Compos. Struct.* **2015**, 119, 365-376.
- [49] B Kim, J Choi, S Yang, S Yu, M Cho. Influence of crosslink density on the interfacial characteristics of epoxy nanocomposites. *Polymer* **2015**, 60, 186-197.
- [50] H Shin, S Yang, S Chang, S Yu, M Cho. Multiscale Homogenization Modeling for Thermal Transport Properties of Polymer Nanocomposites with Kapitza Thermal Resistance. *Polymer* **2013**, 54, 1543-1554.
- [51] V Varshney, SS Patnaik, AK Roy, BL Farmer. A Molecular Dynamics Study of Epoxy-Based Networks: Cross-Linking Procedure and Prediction of Molecular and Material Properties. *Macromolecules* **2008**, 41, 6837-6842.
- [52] H Sun. Force field for computation of conformational energies, structures, and vibrational frequencies of aromatic polyesters. *J. Comput. Chem.* **1994**, 15, 754-779.
- [53] TVM Nodoro, E Voyiatzis, A Ghanbari, DN Theodorou, MC Böhm, PF Müller. Interface of grafted and ungrafted silica nanoparticles with a polystyrene matrix: atomistic molecular dynamics simulations. *Macromolecules* **2011**, 44, 2316-2327.

- [54] TVM Nodoro, MC Böhm, PF Müller. Interface and interphase dynamics of polystyrene chains near grafted and ungrafted silica nanoparticles. *Macromolecules* **2012**, 45, 171-179.
- [55] MR Kessler, SR White. Cure Kinetics of the Ring-Opening Metathesis Polymerization of Dicyclopentadiene. *J. Polym. Sci., Part A* **2002**, 40, 2373-2383.
- [56] M Parrinello, A Rahman. Crystal Structure and Pair Potentials: A Molecular-Dynamics Study. *Phys. Rev. Lett.* **1980**, 45, 1196.
- [57] Accelrys Inc., San Diego, <http://www.accelrys.com/>
- [58] S Plimpton. Fast parallel algorithms for short-range molecular dynamics. *J. Comput. Phys.* **1995**, 117, 1-19.
- [59] M Hori, NS Nemat. Double-inclusion model and overall moduli of multi-phase composites. *Mech. Mater.* **1993**, 14, 189.
- [60] EN Brown, SR White, NR Sottos. Microcapsule induced toughening in a self-healing polymer composite. *J. Mater. Sci.* **2004**, 39, 1703-1710.
- [61] H Jin, GM Miller, SJ Pety, AS Griffin, DS Stradley, D Roach, NR Sottos, SR White. Fracture behavior of a self-healing, toughened epoxy adhesive. *Int. J. Adhes. Adhes.* **2013**, 44, 157-165.
- [62] J-K Chen, Z-P Huang, J Zhu. Size effect of particles on the damage dissipation in nanocomposites. *Compos. Sci. Technol.* **2007**, 67, 2990-2996.
- [63] J Qu, M Cherkaoui. Fundamentals of micromechanics of solid. Hoboken, New Jersey: John Wiley & Sons, Inc. **2006**.
- [64] KK Shi, LX Cai, S Qi, C Bao. A prediction model for fatigue crack growth using effective cyclic plastic zone and low cycle fatigue properties. *Eng. Fract.*

- Mech.* **2016**, 158, 209-219.
- [65] H Shin, S Yang, J Choi, S Chang, M Cho. Effect of interphase percolation on mechanical behavior of nanoparticle-reinforced polymer nanocomposite with filler agglomeration: A multiscale approach. *Chem. Phys. Lett.* **2015**, 635, 80-85.
- [66] RO Ritchie. Mechanisms of fatigue crack propagation in metals, ceramics and composites: Role of crack tip shielding. *Mat. Sci. Eng. A* **1988**, 103, 15-28.
- [67] S Maiti, PH Geubelle. Cohesive modeling of fatigue crack retardation in polymers: Crack closure effect. *Eng. Fract. Mech.* **2006**, 73, 22-41.
- [68] EN Brown, SR White, NR Sottos. Retardation and repair of fatigue cracks in a microcapsule toughened epoxy composite—Part II: In situ self-healing. *Compos. Sci. Technol.* **2015**, 65, 2474-2480.
- [69] RO Ritchie. Mechanisms of fatigue-crack propagation in ductile and brittle solids. *Int. J. Fracture* **1999**, 100, 55-83.
- [70] W Elber. Fatigue crack closure under cyclic tension. *Eng. Fract. Mech.* **1970**, 2, 37-45.
- [71] MN James, CJ Christopher, Y Lu, EA Patterson. Local crack plasticity and its influences on the global elastic stress field. *Int. J. Fatigue* **2013**, 46, 4-15.
- [72] FV Antunes, AG Chegini, R Branco, D Camas. A numerical study of plasticity induced crack closure under plane strain conditions. *Int. J. Fatigue* **2015**, 71, 75-86.
- [73] Y Shao, H-P Zhao, X-Q Feng, H Gao. Discontinuous crack-bridging model for fracture toughness analysis of nacre. *J. Mech. Phys. Solids* **2012**, 60, 1400-1419.
- [74] SE Naleway, MM Porter, J McKittrick, MA Meyers. Structural Design Elements in Biological Materials: Application to Bioinspiration. *Adv. Mater.*

2015, 27, 5455-5476.

- [75] T Mori, K Tanaka. Average stress in matrix and average elastic energy of materials with misfitting inclusions. *Acta. Metall.* **1973**, 21, 571-574.
- [76] J Chakrabarty. Theory of plasticity. 3rd ed. Oxford, UK: Butterworth-Heinemann Publication, **2006**.
- [77] P Lazzarin, M Zappalorto. Plastic notch stress intensity factors for pointed V-notches under antiplane shear loading. *Int. J. Fract.* **2008**, 152, 1-25.
- [78] M Zappalorto, M Salviato, M Quaresimin. Influence of the interphase zone on the nanoparticle debonding stress. *Compos. Sci. Technol.* **2011**, 72, 49-55.
- [79] Dielectric corporation.
www.dielectriccorp.com/downloads/thermoplastics/pes.pdf
- [80] H Sun, SJ Mumby, JR Maple, AT Hagler. An ab initio CFF93 all-atom force field for polycarbonates. *J. Am. Chem. Soc.* **1994**, 116, 2978-2987.
- [81] A Gómez, B Ramón, A Torregaray, JR Sarasua. Mechanical behavior of thermoplastic (PES, PBT) carbon nanofiber composites. ICCM 17, **2009**.
- [82] AA Gusev, MM Zehnder, UW Suter. Fluctuation formula for elastic constants. *Phys. Rev. B* **1996**, 54, 1-4.
- [83] C Li, E Jaramillo, A Strachan. Molecular dynamics simulations on cyclic deformation of an epoxy thermoset. *Polymer* **2013**, 54, 881-890.
- [84] F-L Jin, S-J Park. Improvement in fracture behaviors of epoxy resins toughened with sulfonated poly(ether sulfone). *Polym. Degrad. Stab.* **2007**, 92, 509-514.
- [85] S Horiuchi, AC Street, T Ougizawa, T Kitano. Fracture toughness and morphology study of ternary blends of epoxy, poly(ether sulfone) and

- acrylonitrile-butadiene rubber. *Polymer* **1994**, 35, 5283-5292.
- [86] ET Thostenson, C Li, TW Chou. Nanocomposites in context. *Compos. Sci. Technol.* **2005**, 65, 491-516.
- [87] QH Zeng, AB Yu, GQ Lu. Multiscale modeling and simulation of polymer nanocomposites. *Prog. Polym. Sci.* **2008**, 33, 191-269.
- [88] M Cho, S Yang, S Chang, S Yu. A study on the prediction of the mechanical properties of nanoparticulate composites using the homogenization method with the effective interface concept. *Int. J. Numer. Meth. Eng.* **2011**, 85, 1564-1583.
- [89] P Valsesia, M Beretta, S Bracco, A Comotti, P Sozzani. Polymer/silica nanocomposite micro-objects as a key point for silica-to-polymer shape replication. *J. Mater. Chem.* **2008**, 18, 5511-5517.
- [90] N Vu-Bac, T Lahmer, Y Zhang, X Zhuang, T Rabczuk. Stochastic predictions of interfacial characteristic of polymeric nanocomposites (PNCs). *Composites Part B* **2014**, 59, 80.
- [91] N Vu-Bac, R Rafiee, X Zhuang, T Lahmer, T Rabczuk. Uncertainty quantification for multiscale modeling of polymer nanocomposites with correlated parameters. *Composites Part B* **2015**, 68, 446.
- [92] S Yang, J Choi, M Cho. Elastic stiffness and filler size effect of covalently grafted nanosilica polyimide composites: molecular dynamics study. *ACS Appl. Mater. Inter.* **2012**, 4, 4792-4799.
- [93] PK Valavala, GM Odegard. Modeling techniques for determination of mechanical properties of polymer nanocomposites. *Rev. Adv. Mater. Sci.* **2005**, 9, 34-44.
- [94] J Choi, S Yang, S Yu, H Shin, M Cho. Method of scale bridging for

- thermoelasticity of cross-linked epoxy/SiC nanocomposites at a wide range of temperature. *Polymer* **2012**, 53, 5178-5189.
- [95] S Yang, S Yu, W Kyoung, D-S Han, M Cho. Multiscale modeling of size-dependent elastic properties of carbon nanotube/polymer nanocomposites with interfacial imperfections. *Polymer* **2012**, 53, 623-633.
- [96] R Rahman, A Haque. Molecular modeling of crosslinked graphene-epoxy nanocomposites for characterization of elastic constants and interfacial properties. *Composites Part B* **2013**, 54, 353.
- [97] S Yu, S Yang, M Cho. Analysis of thermal conductivity of polymeric nanocomposites under mechanical loading. *J. Appl. Phys.* **2013**, 114, 213503.
- [98] D Frenkel, B Smit. Understanding Molecular Simulation, 2nd Edition: From Algorithms to Applications (Computational Science). Academic Press, **2001**.
- [99] M Parrinello, A Rahman. Strain fluctuations and elastic constants. *J. Chem. Phys.* **1982**, 76, 2662-2666.
- [100] N Vu-Bac, T Lahmer, H Keitel, J Zhao, X Zhuang, T Rabczuk. Stochastic predictions of bulk properties of amorphous polyethylene based on molecular dynamics simulations. *Mech. Mater.* **2014**, 68, 70-84.
- [101] C Redenbach, I Vecchio. Statistical analysis and stochastic modelling of fibre composites. *Compos. Sci. Technol.* **2011**, 71, 107-112.
- [102] GM Odegard, BD Jensen, S Gowtham, J Wu, J He, Z Zhang. Predicting mechanical response of crosslinked epoxy using ReaxFF. *Chem. Phys. Lett.* **2014**, 591, 175-178.
- [103] C Wei, D Srivastava, K Cho. Thermal Expansion and Diffusion Coefficients of Carbon Nanotube-Polymer Composites. *Nano Lett.* **2002**, 2, 647-650.

- [104] HB Fan, MMF Yuen. The experimental data can be found from HEXION TM technical data sheet, 'Diglycidyl Ether of Bisphenol F (DGEFB) – Performance Properties'. *Polymer* **2007**, 48, 2174-2178.
- [105] R Hill. The elastic behavior of a crystalline aggregates. *Proc. Phys. Soc. London, Sect. A* **1952**, 65, 349-354.
- [106] DW Scott. Average shifted histograms: effective non-parametric density estimators in several dimensions. *Ann. Stat.* **1985**, 13, 1024-1040.
- [107] DIGIMAT. Software Platform for Nonlinear Multi-scale Modeling of Composite Materials and Structures. e-Xstream Engineering, Belgium and Luxembourg. Available from: www.e-Xstream.com, **2009**.
- [108] Y Yu, B Zhang, Z Tang, G Qi. Stress transfer analysis of unidirectional composites with randomly distributed fibers using finite element method. *Composites Part B* **2015**, 69, 278.
- [109] MP Bendsøe, N Kikuchi. Generating optimal topologies in structural design using a homogenization method. *Comput. Methods. Appl. Mech. Eng.* **1988**, 71, 197-224.
- [110] JM Guedes, N Kikuchi. Preprocessing and postprocessing for materials based on the homogenization method with adaptive finite element methods. *Comput. Methods. Appl. Mech. Eng.* **1990**, 83, 143-198.
- [111] S Yang, M Cho. A scale-bridging method for nanoparticulate polymer nanocomposites and their nondilute concentration effect. *Appl. Phys. Lett.* **2009**, 94, 223104.
- [112] BD Wood, F Cherblanc, M Quintard, S Whitaker. Volume averaging for determining the effective dispersion tensor: Closure using periodic unit cells and

- comparison with ensemble average. *Water Resour. Res.* **2003**, 39, 1210.
- [113] G Matheron. The theory of regionalized variables and its applications. *Tech. Rep., Paris School of Mines Publications* 1971.
- [114] C-S Man, M Huang. A Simple Explicit Formula for the Voigt-Reuss-Hill Average of Elastic Polycrystals with Arbitrary Crystal and Texture Symmetries. *J. Elasticity.* **2011**, 105, 29.
- [115] L Vaisman, HD Wagner. The role of surfactants in dispersion of carbon nanotubes. *Adv. Colloid Interface Sci.* **2006**, 128, 37.
- [116] J Liu, Y Gao, D Cao, L Zhang, Z Guo. Nanoparticle dispersion and aggregation in polymer nanocomposites: insights from molecular dynamics simulation. *Langmuir* **2011**, 27, 7926-7933.
- [117] LM Hamming, R Qiao, PB Messersmith, LC Brinson. Effects of dispersion and interfacial modification on the macroscale properties of TiO₂ polymer-matrix nanocomposites. *Compos. Sci. Technol.* **2009**, 69, 1880-1886.
- [118] D Weidt, L Figiel. Effect of CNT waviness and Van der Waals interaction on the nonlinear compressive behavior of epoxy/CNT nanocomposites. *Compos. Sci. Technol.* **2015**, 115, 52-59.
- [119] S-G Prolongo, M Buron, M-R Gude, R-C Moran, M Campo, A Urena. Effects of dispersion techniques of carbon nanofibers on the thermo-physical properties of epoxy nanocomposites. *Compos. Sci. Technol.* **2008**, 68, 2722-2730.
- [120] GK Hu, G Guo, D Baptiste. A micromechanical model of influence of particle fracture and particle cluster on mechanical properties of metal matrix composites. *Comp. Mater. Sci.* **1998**, 9, 420-430.

- [121] QS Yang, XQ He, X Liu, F-F Leng, Y-W Mai. The effective properties and local aggregation effect of CNT/SMP composites. *Composites Part B* **2012**, 43, 33-38.
- [122] J Cho, J-J Luo, I-M Daniel. Mechanical characterization of graphite/epoxy nanocomposites by multi-scale analysis. *Compos. Sci. Technol.* **2007**, 67, 2399-2407.
- [123] LM Hall, A Jayaraman, KS Schweizer. Molecular theories of polymer nanocomposites. *Curr. Opin. Solid State Mater. Sci.* **2010**, 14, 38.
- [124] A Pontefisso, M Zappalorto, M Quaresimin. An efficient RVE formulation for the analysis of the elastic properties of spherical nanoparticle reinforced polymers. *Comp. Mater. Sci.* **2015**, 96, 319-326.
- [125] H Gu, Y Guo, SY Wong, C He, X Li, VPW Shim. Effect of interphase and strain-rate on the tensile properties of polyamide 6 reinforced with functionalized silica nanoparticles. *Compos. Sci. Technol.* **2013**, 75, 62-69.
- [126] S Yang, S Yu, J Ryu, J-M Cho, W Kyoung, D-S Han, M Cho. Nonlinear multiscale modeling approach to characterize elastoplastic behavior of CNT/polymer nanocomposites considering the interphase and interfacial imperfection. *Int. J. Plasticity* **2013**, 41, 124.
- [127] GM Odegard, TC Clancy, TS Gates. Modeling of the mechanical properties of nanoparticle/polymer composites. *Polymer* **2005**, 46, 553.
- [128] I Sevostianov, M Kachanov. Effect of interphase layers on the overall elastic and conductive properties of matrix composites. Applications to nanosize inclusion. *Int. J. Solids. Struct.* **2007**, 44, 1304.
- [129] RK Patel, B Bhattacharya, S Basu. Effect of interphase properties on the

- damping response of polymer nano-composites. *Mech. Res. Commun.* **2008**, 35, 115-125.
- [130] HW Wang, HW Zhou, RD Peng, JL Mishnaevsky. Nanoreinforced polymer composites: 3D FEM modeling with effective interface concept. *Compos. Sci. Technol.* **2011**, 71, 980.
- [131] MSC Software Inc., California (www.mscsoftware.com).
- [132] H Hill. The elastic behavior of a crystalline aggregates. *Proc. Phys. Soc. Sect. A* **1952**, 65, 349-354.
- [133] R Toth, F Santese, SP Pereira, DR Nieto, S Pricl, M Fermeglia, P Posocco. Size and shape matter! A multiscale molecular simulation approach to polymer nanocomposites. *J. Mater. Chem.* **2012**, 22, 5398.
- [134] JS Smith, D Bedrov, GD Smith. A molecular dynamics simulation study of nanoparticle interactions in a model polymer-nanoparticle composite. *Compos. Sci. Technol.* **2003**, 63, 1599.
- [135] ABAQUS/CAE Version 6.12; **2012**.

국문요약

본 논문에서는 자가치료 고분자 복합재의 멀티스케일 기계적 해석을 수행하였다. 최근 혈액응고 과정을 모방한 자가치료 고분자 재료에 대한 연구가 활발히 이루어지고 있다. 70% 이상의 높은 치료 효율을 보이는 한편, 치료제를 포함하고 있는 구형 마이크로 캡슐의 함량이 증가함에 따라 점차 낮은 기계적 강도와 파괴 인성 특성을 보인다는 단점이 있다. 이러한 단점을 개선하기 위해, 캡슐 이외에 탄소나노튜브나 열소성 고분자 입자와 같은 충전제를 추가적으로 첨가한 “자가치료 고분자 복합재”의 개발이 이루어지고 있다. 많은 양의 설계 인자와 복잡한 역학 기작으로 인해, 실험 정보만으로 최적 설계를 수행하기에 어렵다는 문제가 있다. 이를 해결하기 위해서 본 연구에서는 설계에 명확한 방향을 제시할 수 있도록 이론에 기반한 해석 방법론을 제안하고, 이에 기반한 해석을 수행하였다.

자가치료 고분자 복합재료의 역학 문제는 균열 주변의 충전제로 인한 파괴 인성 향상 기작과 시편의 균열 치료 현상이 복합적으로 반영된 복잡한 문제이다. 본 논문의 연구 목표를 달성하기 위해 다음 두 가지 이론 기반 모델을 개발하였다. 우선, 마이크로 캡슐의 함량에 따른 자가치료 고분자 재료의 탄성 물성, 초기 파괴 인성, 치료 정도에 따른 파괴 인성을 예측할 수 있는 “자가치료 고분자 재료의 기계적 거동 예측 모델”을 개발하였다. 치료가 일어나는 동적 과정 하에 치료제와

기지재의 접촉 특성 및 계면의 기계적 거동 특성을 모사하기 위해 가교 동역학 모델과 분자동역학 전산모사를 접목한 방법론을 제안하였다. 그 다음, 충전제의 일종인 나노입자나 열소성 입자의 첨가로 인해 향상된 파괴 인성을 예측할 수 있는 “균열 주변의 멀티스케일 연속체 역학 모델”을 개발하였다. 파괴 인성은 소산된 에너지와 밀접한 관련이 있다. 향상된 파괴 인성의 예측을 위해 소산된 에너지를 연속체 역학을 토대로 정량화 하였다. 제안된 두 가지 모델은 모두 실험 결과와 비교하여 높은 정확도를 보인다는 것을 확인하였다. 자가치료 고분자 재료의 기계적 거동 예측 모델을 토대로 치료 정도에 따른 균열 주변의 응력 분포를 예측하고, 이를 기반으로 치료 정도에 따른 파괴 인성 향상 정도를 예측할 수 있다. 이러한 일련의 과정을 통해 자가치료 고분자 복합재료의 기계적 해석을 위한 이론 기반 틀을 구축하고, 기계적 해석을 수행하였다.

주요어: 자가치료 고분자, 고분자 나노복합재료, 멀티스케일 해석, 피로 및 파괴 해석, 유한요소 해석, 분자동역학 전산모사

학번: 2011-20720